

Sm/Nd garnet geochronology and pressure-temperature paths of eclogites from Syros, Greece: Implications for subduction zone processes and water loss from the subducting slab

Author: Jamie Kendall

Persistent link: <http://hdl.handle.net/2345/bc-ir:107239>

This work is posted on [eScholarship@BC](#),
Boston College University Libraries.

Boston College Electronic Thesis or Dissertation, 2016

Copyright is held by the author. This work is licensed under a Creative Commons Attribution-NonCommercial-NoDerivatives 4.0 International License (<http://creativecommons.org/licenses/by-nc-nd/4.0>).

Sm/Nd garnet geochronology and pressure-
temperature paths of eclogites from Syros,
Greece: Implications for subduction zone
processes and water loss from the
subducting slab

Jamie Kendall

A thesis

submitted to the Faculty of

the department of Earth and Environmental Sciences

in partial fulfillment

of the requirements for the degree of

Master of Science

Boston College
Morrissey College of Arts and Sciences
Graduate School

December 2016

Sm/Nd garnet geochronology and pressure-temperature paths of eclogites from Syros, Greece: Implications for subduction zone processes and water loss from the subducting slab

Jamie Kendall

Advisor: Ethan Baxter, PhD

Samarium/Neodymium (Sm-Nd) garnet geochronology of eclogites from Syros, Greece provides constraints on timing of peak metamorphism while thermodynamic modeling of the same samples allows a comparison of pressure-temperature (P-T) paths. Sm-Nd geochronology of four eclogite samples give ages of 48.8 ± 3.2 Ma (high $^{147}\text{Sm}/^{144}\text{Nd} = 0.49$, $n = 6$, MSWD = 0.67), 48.1 ± 2.3 Ma (high $^{147}\text{Sm}/^{144}\text{Nd} = 1.22$, $n = 4$, MSWD = 2.4), 44.7 ± 1.0 Ma (high $^{147}\text{Sm}/^{144}\text{Nd} = 3.9$, $n = 6$, MSWD = 1.4), and 43.6 ± 1.6 Ma (high $^{147}\text{Sm}/^{144}\text{Nd} = 1.39$, $n = 6$, MSWD = 2). These garnet growth ages span several million years and are younger than the only other published garnet eclogite ages from the island which use Lutetium/ Hafnium (Lu-Hf) garnet geochronology to place peak metamorphism at ~ 52 Ma (Lagos et al, 2007). Another eclogite sample dated less precisely yielded an age of 57.7 ± 6.3 Ma (high $^{147}\text{Sm}/^{144}\text{Nd} = 0.40$, $n = 10$, MSWD = 1.9), significantly older than the other garnets dated in this study. The garnet ages from eclogites presented here suggest that high pressure-low temperature metamorphism, and related garnet growth and dehydration, on Syros lasted ~ 9 myr, similar to what has been reported for nearby Sifnos Island (Dragovic et al., 2015). Thermodynamic modeling of three samples reveals similar prograde P-T paths despite differences in tectonic setting and chemistry between samples. Water loss from mineral breakdown during the span of subduction zone garnet growth varies between samples from 1.09 to 5.13 weight percent but is greatest for the most ultramafic sample due to chlorite stability permitting greater

capacity for water to be carried to depth. P-T paths reach greater maximum pressures (up to 2.42 GPa) than what is reported for Sifnos island (Dragovic et al., 2015) and greater than most previously published pressure estimates for Syros (ie. Okrusch and Bröcker, 1990; Putlitz et al., 2005).

TABLE OF CONTENTS

Table of Contents	iii
List of tables.....	v
List of figures.....	vi
List of abbreviations.....	viii
Acknowledgements.....	x
1.0 Introduction	1
2.0 Background.....	4
2.1 Geologic Setting.....	4
2.2 Previous work and outstanding questions.....	5
3.0 Methods.....	8
3.1 Garnet geochronology.....	8
3.1.1 Bulk garnet geochronology	8
3.1.2 Micro-sampled garnet geochronology.....	11
3.1.3 Laser ablation for trace element concentration	12
3.2 Thermodynamic modeling.....	13
3.2.1 Necessary data for Perple_X modeling	14
3.2.2 Modeling garnet growth and water loss.....	15
4.0 Sample Descriptions.....	21
5.0 Results	25
5.1 Geochronology.....	25
5.2 Trace element concentrations	27
5.3 Thermodynamic modeling.....	29
5.4 Thermodynamic modeling and water loss.....	33
6.0 Discussion	34
6.1 Challenges and successes with Sm/Nd garnet geochronology	34
6.2 Regional implications of garnet geochronology.....	40
6.3 Challenges and successes with thermodynamic modeling.....	45
6.4 Regional implications of thermodynamic modeling.....	52
7.0 Conclusions.....	58
8.0 Tables.....	60
9.0 Figures.....	69

10.0	Appendices.....	97
10.1	Appendix A: TIMS standards and blanks	98
10.2	Appendix B: Slices of rock sent for XRF	101
10.3	Appendix C: Parameters for Perple_X runs	102
10.4	Appendix E: Exploratory geochronology	106
10.5	Appendix D: Labeled pseudosections.....	110
10.6	Appendix F: Micro-sampling a single large garnet	119
11.0	References.....	129

LIST OF TABLES

Table 1 Oxide weight percent data for rocks.....	60
Table 2 Oxide weight percent data for minerals.....	61
Table 3 Isotope data from TIMS analysis.....	62
Table 4 Garnet ages.....	65
Table 5 Compositions used for thermodynamic modeling.....	66
Table 6 Water loss during garnet growth.....	67
Table 7 Comparison of modal mineralogy observed in samples to that predicted by modeling.....	68
Table A1 Samples used in exploratory geochronology.....	106
Table A2 Exploratory isotopic data.....	107
Table A3 Sample preparation for 14BSY-10A.....	123
Table A4 Isotope data for 14BSY-10A.....	124

LIST OF FIGURES

Figure 1 Simplified geologic map of Syros, Greece.....	70
Figure 2 Microdrilling 14BSY-35D.....	71
Figure 3 Major element garnet transect for sample 06MSY-6E.....	73
Figure 4 Major element garnet transect for sample 14RSY-8A.....	74
Figure 5 Major element garnet transect for sample 14BSY-35D	75
Figure 6 Major element garnet transect for sample 14BSY-37A.....	76
Figure 7 Major element garnet transect for sample 14BSY-38A.....	77
Figure 8 Ferric iron and carbonate in fluid: exploratory pseudosections.....	78
Figure 9 Field photographs, sample photographs, and modal mineralogy.....	80
Figure 10 Representative photomicrographs.....	81
Figure 11 Isochrons for bulk garnet ages.....	82
Figure 12 Isochrons for core and rim ages for sample 14BYS-35D.....	83
Figure 13 Photo micrographs and laser ablation trace element data.....	84
Figure 14 Sm, Nd, and Lu concentrations for sample 14BSY-38A.....	85
Figure 15 Pseudosections for sample 06MSY-6E.....	86
Figure 16 Pseudosections for sample 14BSY-35D.....	88
Figure 17 Pseudosections for sample 14BSY-37A.....	89
Figure 18 Pseudosections for sample 14BSY-38A and 14BSY-38B.....	90

Figure 19 Labeled isochron and age vs. $^{147}\text{Sm}/^{144}\text{Nd}$ for sample 14RSY-8A.....	91
Figure 20 Labeled isochron and age vs. $^{147}\text{Sm}/^{144}\text{Nd}$ for sample 06MSY-6E.....	92
Figure 21 Garnet ages from Sifnos and Syros islands.....	93
Figure 22 All geochronology on Syros	94
Figure 23 P-T paths for modeled samples and comparison to Sifnos.....	96
Figure A1 $^{143}\text{Nd}/^{144}\text{Nd}$ Ames standards through time.....	98
Figure A2 Picograms of Nd measured in blanks through time.....	100
Figure A3 Slices of rock sent for bulk sample XRF analysis.....	101
FigureA4 Isochrons from exploratory work.....	109
Figure A5 06MSY-6E WR pseudosection: fully labeled for reference.....	110
Figure A6 06MSY-6E matrix pseudosection: fully labeled for reference.....	111
Figure A7 06MSY-6E matrix2 pseudosection: fully labeled for reference.....	112
Figure A8 14BSY-37A WR pseudosection: fully labeled for reference.....	113
Figure A9 14BSY-37A matrix pseudosection: fully labeled for reference.....	114
Figure A10 14BSY-38A WR pseudosection: fully labeled for reference.....	115
Figure A11 14BSY-38A, 38B hybrid WR pseudosection.: fully labeled for reference.....	116
Figure A12 14BSY-38A, 38B hybrid matrix pseudosection: fully labeled for reference.....	117
Figure A13 14BSY-38B WR pseudosection: fully labeled for reference.....	118
Figure A14 Sample preparation for microdrilling sample 14BSY-10A.....	125
Figure A15 Drilling sample 14BSY-10A.....	126
Figure A16 Isochrons for sample 14BSY-10A bulk, core and rim.....	128

LIST OF ABBREVIATIONS

%	percent
Amph	amphibole
Al	aluminum
Al ₂ O ₃	aluminum oxide
Ar	argon
arag	aragonite
Bio	biotite
C	celcius
Ca	calcium
CaO	calcium oxide
CBU	Cycladic Blueschist Unit
Chl	chlorite
CO ₂	carbon dioxide
Cpx	clinopyroxene
Do	dolomite
Ep	epidote
Fe	iron
Fe ₂ O ₃	iron oxide or ferric iron
Fe ³⁺	ferric iron
FeO	iron oxide or ferrous iron
Fetot	total iron
Gt	garnet
GPa	gigapascal
H ₂ O	di-hydrogen oxide or water
H ₃ PO ₄	phosphoric acid
HF	hydrofluoric acid
Hf	hafnium
HP-LT	high-pressure low-temperature
Ilm	ilmenite
K	kelvin
K	potassium
K ₂ O	potassium oxide
kV	kilovolt
LA-ICPMS	laser ablation inductively coupled plasma mass spectrometer
law	lawsonite

Lu	lutetium
Ma	megaannum
Mag	magnesite
Mg	magnesium
MgO	magnesium oxide
Mica	white mica
mL	milliliters
MLA	Methyl Lactic Acid
mm	millimeters
Mn	manganese
MnO	manganese oxide
mol	mole
MPa	megapascal
MSWD	mean square weighted deviation
myr	million years
Na	sodium
Na ₂ O	sodium oxide
Nd	neodymium
Pb	lead
ppm	parts per million
P-T	pressure-temperature
q	quartz
Rb	rubidium
REE	rare earth element
RSD	relative standard deviation
ru	rutile
Si	silica
SiO ₂	silica dioxide
Sm	samarium
sph	sphene
Sr	strontium
stlp	stilpnomelene
Ta ₂ O ₅	tantalum oxide
Ti	titanium
TiO ₂	titanium oxide
TIMS	Thermal Ionization Mass Spectrometer
U	Uranium
vsv	vesuvianite
vol	volume
wt	weight
XRF	X-Ray Fluorescence
zo	zoisite

ACKNOWLEDGEMENTS

I would like to thank my fellow B.U. graduate students; Katie Manerio, Emily Stewart, Nora Sullivan, Jen Lamp, Rachel Scudder, Ann Dunlea, Sarabeth Buckley, Chloe Anderson, and Will Kearney. Their constant support and indomitable sense of humor made doing any of this possible. Shaina Cohen, Martha Parsons, and Will Montz were my first friends at B.C. and also some of the smartest, hardest-working people I have ever met. I owe a debt of gratitude to Besim Dragovic who, out of the goodness of his own heart helped me with lab work, excel files, and so much more. Thanks to the Smats fieldwork dream team: Jen Gorce, Hanna Brooks, and Evan “Boxman” Ramos. I can’t imagine Grizzas, or any of this, without you guys.

Thanks to my parents, who nurtured a scientific curiosity in their daughter and have supported me every step of the way. Thanks to my real sister, Ellie, and my honorary sister, Hannah for being sources of humor and inspiration throughout this process and for my whole life. And thanks to Rohan who put up with a lot while I finished this degree and never once stopped supporting me or making me laugh.

Thanks to Arlo Weil, whose introductory geology course started me off on this journey. Thanks are owed to Mike Tappa, Tom Ireland, and Denise Honn who answered my questions, cleaned up my mistakes, and were always willing to come listen to the weird sound the TIMS was making this time. I would like to thank Seth Kruckenberg, whose editing greatly improved this document. Thanks to Mark Caddick, whose incredible knowledge of geology and equally incredible dry sense of humor greatly shaped my graduate experience. Finally, thanks to my advisor, Ethan Baxter who taught me all there is to know about garnet geochronology and so much more.

For my late grandmother, Peggy, who was the only woman in her class when she got her M.S. in 1952. I walk in her footsteps.

1.0 INTRODUCTION

When oceanic crust plunges into the mantle at subduction zones, it undergoes a cascade of complex metamorphic devolatilization reactions which, though they occur at the scale of a crystal lattice, exert a huge influence on the planet. These metamorphic reactions are fundamental components of the global chemical cycling, including the water cycle and the carbon cycle, that makes the planet habitable (Hacker, 2008; Kelemen & Manning, 2015). Metamorphic devolatilization reactions have been hypothesized to create earthquakes (Hacker et al., 2003) and have been long understood to be the cause of the most explosive volcanic activity on the planet by inducing flux melting of the mantle (ex: Tatsumi, 1986). Subduction zone metamorphism, however, is particularly difficult to study. Subduction zones are dynamic, constantly evolving systems inaccessible to scientists working on the surface of the earth and their unique high-pressure low-temperature geotherm is not found in any other geologic environment.

Thermodynamic and experimental modeling of subduction zone metamorphism has provided geoscientists with a wealth of information (ex: Schmidt & Poli, 1998; van Keken et al., 2011) but accurate model parameters are difficult to determine.

Metamorphism at subduction zones is influenced by the local geothermal gradient, the composition of the incoming crust, slab dip, and subduction rate. Even when these can be approximated, the nature of modeling is to assume a closed chemical system and

thermodynamic equilibrium. Subduction zones, however, are sites of massive chemical and fluid exchange, and huge changes in temperature over short distances (ex: Abers et al., 2006). These factors make equilibrium a dubious assumption.

While most of the material sent into subduction zones continues on a one-way path into the mantle, occasionally some of this metamorphosed oceanic crust is exhumed and preserved at the surface of the earth. Studies of the blueschists, eclogites, serpentinites, and associated high-pressure low-temperature rocks that make up fossil subduction zone assemblages have revealed a wealth of information including the P-T and deformation history of the rocks (ex, Trotet et al., 2001a, b; Davis & Whitney, 2008), the composition of metamorphic associated fluid (ex, Früh-Green et al., 2004; Spandler & Hermann, 2006; Marschall et al., 2008), and the degree of fluid-rock interaction (ex, Bebout & Barton, 1989; Halama et al., 2011). While incredibly illuminating in their own right, such studies also serve as a way to ground-truth and guide thermodynamic models (ex, Davis & Whitney, 2006; Schumacher et al., 2008; Konrad-Schmolke et al, 2011). Yet, a temporal component is often missing from both modeling and field studies; while the P-T path a rock experienced can be modeled and inferred from petrography, the timing and duration of the metamorphic event (the P-T-t path) is usually overlooked or is based on assumptions. Geochronology of minerals from exhumed subduction-related rocks such as Ar-Ar in mica (Putliz et al., 2005), Rb-Sr in mica (Bröcker et al., 2013), U-Pb in zircon (Bröcker & Enders, 1999; Rubatto, 2002), and, in one instance, Lu-Hf in lawsonite (Mulcahy et al., 2014) can provide this missing time element. Garnet is a highly resistant prograde mineral found in many subduction zone rocks, which can preserve growth zoning and, critically, whose growth is associated with dehydration reactions (Baxter &

Caddick, 2013). Dating garnet with Sm-Nd or Lu-Hf, coupled with information about the distribution of these elements in garnet crystals can yield high-precision ages of subduction zone metamorphism. With thermodynamic modeling this growth can be tied to dehydration during subduction. Because garnet can preserve growth zoning, in some cases it is possible to micro-sample individual growth zones allowing for a highly nuanced and more complete picture of the metamorphic process (Pollington & Baxter, 2010; Dragovic et al., 2012).

2.0 BACKGROUND

2.1 GEOLOGIC SETTING

Syros, Greece is a small (80 km²) island in the Cyclades, an archipelago south of the Grecian mainland in the Mediterranean Sea. Several of these islands, including Syros, have excellent exposure of well-preserved high-pressure, low-temperature metamorphic rocks known as the Attic-Cycladic crystalline complex (Fig. 1). The Attic-Cycladic crystalline complex is composed of two tectonic units: the Cycladic Blueschist Unit (CBU) derived from former oceanic crust and sediment and the Vari Unit of crystalline basement (Keiter et al., 2011). The CBU records an initial eclogite to blueschist facies metamorphic event (acquired during subduction) and subsequent greenschist facies overprint (potentially acquired during exhumation) (Trotet et al., 2001a). The blueschist facies event is best preserved on the islands of Sifnos, Tinos, and Syros where alternating bands of marble and schist dominate the lithology. Intercalated with this sedimentary material is a metabasic tectonic *mélange* comprised of blueschist and eclogite facies metabasalts and metagabbros (Keiter et al., 2011). Often, the metabasic tectonic *mélange* is associated with a serpentine-talc-chlorite-tremolite schist. This serpentinite schist unit hosts the famous “knockers” of entrained pods made of eclogite, omphacite, glaucophanite, or metagabbro and rimmed with a reaction rind “blackwall” material of

tourmaline-actinolite-chlorite- rutile (Marschall et al., 2006; Keiter et al., 2011). An extensive geologic literature, including a recent and highly detailed map (Keiter et al., 2011), mean that much about the origin and degree of metamorphic overprint of the exhumed rocks is already established. This intellectual foundation makes Syros an ideal place to use garnet geochronology and thermodynamic modeling to refine our understanding of the nature of subduction zone processes and associated metamorphism. At the same time, questions specific to Syros still remain, such as the nature of an apparent HP-LT metamorphic event at ~80 Ma and the duration of the HP-LT event evident at ~50 Ma.

2.2 PREVIOUS WORK AND OUTSTANDING QUESTIONS

Extensive geochronology has been performed on the rocks of Syros, but most studies have dated zircon with U-Pb techniques (ex: Tomaschek et al., 2003) or mica with Ar-Ar (ex: Putlitz et al. 2005) or Rb-Sr (ex: Bröcker et al., 2013) isotopic methods. These studies have yielded protolith ages (Bröcker and Kiesling, 2006) or a wide range of ages from peak metamorphism (Maluski et al., 1987; Putlitz et al., 2005; Lister and Forster, 2016) through the greenschist facies overprint (Bröcker et al., 2013). Only one investigation has dated prograde metamorphic garnet. Lagos et al (2007) used Lu-Hf in garnet to date three eclogite facies samples, and concluded that prograde metamorphism preserved in the rocks on Syros took place over a short time interval between 52.2 ± 0.3 and 50 ± 2 Ma. A single zircon from a larger zircon study yielded ages almost directly in agreement with this tight time interval; Tomaschek et al. (2003) found a U-Pb zircon

age of 52.4 ± 0.8 Ma in a plagiogranite dike. Two other zircon studies have turned up interesting signs of an earlier HP-LT event at ~ 80 Ma (Bröcker and Enders, 2001; Bröcker and Keisling, 2006) but no additional support for this has been found. Garnet geochronology on nearby Sifnos island (Fig. 1) has revealed a different picture. There, prograde garnet growth ages span from 53.4 ± 2.6 (Dragovic et al., 2015) to 42.5 ± 3 (Dragovic, 2013), across a variety of lithologies (Fig. 2). Is there a difference in the timing of prograde metamorphism between the two islands? Is there any evidence in garnet for an earlier HP-LT event on Syros? This study uses $^{147}\text{Sm}/^{144}\text{Nd}$ garnet geochronology of five eclogite samples to resolve these outstanding questions.

Two recent studies combine zoned garnet geochronology and thermodynamic modeling on the island of Sifnos (Dragovic et al., 2012, 2015). The authors used identical methodology to tie garnet growth to H_2O loss from the subducting slab using `Perple_X` thermodynamic modeling (Connolly, 1990). Fluid loss is of particular interest in subduction zone rocks because metamorphic fluids in this setting are widely accepted to be the source of water for flux melting at volcanic arcs, the transport mechanism for many elements, and to be an important component of the global water cycle. Interestingly, the two studies found two different results. Dragovic et al. (2012) found that garnet growth in a mafic blueschist was sudden and occurred in one single pulse at $\sim 46.49 \pm 0.36$ Ma, involving up to 7×10^{-10} mol of fluid/ cm^3 of rock lost over only 1 million years. The rate of growth was rapid but the amount of fluid lost from the lithology was on the whole rather small, ~ 0.3 - 0.4 wt % lost over the period of garnet growth. Dragovic et al. (2015) found that garnet growth in a quartz mica schist was punctuated by pulses of rapid growth at 53.4 Ma, 47.2 Ma, and 44.96 ± 0.53 Ma in

between longer periods of very slow or no growth. This lithology also lost a very small amount of water from the bulk rock; it saw only 0.52 wt % water loss during garnet growth. By contrast, modeling of generalized MORB predicts it is possible to lose ~ 1 wt% water over a similar pressure temperature path during garnet growth (Baxter and Caddick, 2013). How does the bulk chemistry and P-T path of the rock affect the water lost during garnet growth? Is the water loss seen on Sifnos comparable to what occurred on Syros? This study uses thermodynamic modeling of four eclogite samples to try to address these questions.

3.0 METHODS

3.1 GARNET GEOCHRONOLOGY

3.1.1 Bulk garnet geochronology

Samarium (Sm) 147 decays to Neodymium (Nd) 143 by alpha decay with a half-life of 1.06×10^{11} years. The $^{147}\text{Sm} - ^{143}\text{Nd}$ decay system can be used to date co-genetic minerals or rocks that fractionate Sm from Nd during crystallization (Faure and Mensing, 2005). Garnet, though it possesses an overall low REE concentration, strongly fractionates Sm over Nd. While typical rocks and minerals will have a $^{147}\text{Sm}/^{144}\text{Nd}$ value of about 0.1 to 0.2, garnet can have a $^{147}\text{Sm}/^{144}\text{Nd}$ value up to 6 and more often in the range of 1 to 2 (Baxter & Scherer, 2013). Age calculation requires measurement of the parent isotope relative to a stable daughter ($^{147}\text{Sm}/^{144}\text{Nd}$) and the radiogenic daughter relative to the stable daughter ($^{143}\text{Nd}/^{144}\text{Nd}$) for at least two different co-genetic minerals or mineral assemblages. This information is plotted in $^{147}\text{Sm}/^{144}\text{Nd}$ vs $^{143}\text{Nd}/^{144}\text{Nd}$ space and the age is calculated by finding the slope of the line connecting the data points. Minerals and rocks which are co-genetic and have not been subjected to open system behavior will form a line in this space called the “isochron.” The statistical rigor of the isochron is evaluated by calculating the mean square weighted deviation (MSWD), a

quantification of the probability that the values on the isochron truly form a line (Wendt & Carl, 1991). For this research, isochrons are constructed using isotopic ratios from several chemically-cleansed garnet separates and a representative piece of the bulk rock. Ages are calculated using “Isoplot,” free software for use in Microsoft Excel from the University of California at Berkeley (Ludwig, 2008).

Metamorphic garnets often contain abundant inclusions which can make it impossible to physically separate pure garnet from micro-inclusions. As inclusions will nearly always have a greater Sm and Nd concentration than the garnet, small amount of micro-inclusions left in the garnet can dominate the measured Sm and Nd values and result in an apparently low $^{147}\text{Sm}/^{144}\text{Nd}$ ratio. This was recognized as a challenge in the very earliest garnet geochronology (van Breemen & Hawkesworth, 1980) and has since led to the misconception, still found in the community today, that Sm-Nd is an unreliable chronometer for metamorphic garnet growth. In fact, researchers have developed partial dissolution cleansing procedures to remove micro-inclusions from crushed garnet before the garnet is fully dissolved (Dewolf et al., 1996; Amato et al., 1999; Scherer et al., 2000; Baxter et al., 2002; Anczkiewicz & Thirwall., 2003; Pollington & Baxter, 2011). These partial dissolutions are usually modified for each sample to find the ideal method to remove inclusions but not dissolve too much pure garnet. A garnet is generally considered clean enough to avoid deleterious effects on age precision and accuracy when the partial dissolution yields a $^{147}\text{Sm}/^{144}\text{Nd} > 1$ and a Nd concentration < 0.5 ppm (see Baxter and Scherer, 2013).

The partial dissolution procedure used for bulk garnet geochronology in this research is based on that described in Baxter et al. (2002). Garnet is separated from the

rock by hand picking and magnetic separation and then crushed to between 149 and 63 microns in size. About 100 mg of this “garnet separate” is heated and sonicated in a closed beaker with 2 mL dilute hydrochloric acid and 1 mL concentrated hydrofluoric acid for 30 to 180 minutes to dissolve inclusions. In order to dissolve secondary fluorides, this acid mixture is then decanted and the sample is placed in 1 mL dilute hydrochloric acid and 2 mL concentrated perchloric acid, sonicated and heated for one hour and then dried in an elbow still overnight. The solid garnet is subsequently sonicated and heated for 180 minutes in 2 mL concentrated nitric acid to completely dissolve any secondary fluorides. The nitric acid is decanted and the solid garnet inspected for remaining visible inclusions and handpicked as necessary. The inclusion-cleansed garnet is subsequently fully dissolved using a sequential hydrofluoric acid, nitric acid, hydrochloric acid process.

After full dissolution, column chemistry in a clean lab is necessary to isolate the Sm and Nd for analysis. First, a cation exchange resin column is used to remove iron from the solution. Then, a Tru-spec column removes all elements except rare earth elements. Finally, a cation exchange column run with twice-distilled methyl lactic acid (MLA) isolates Sm and Nd. Samples are “spiked” with a “mixed spike” solution of known $^{147}\text{Sm}/^{144}\text{Nd}$ concentration after full dissolution and prior to column chemistry to allow the calculation of concentration from mass spectrometer data. Samarium and Nd are run separately on the Thermo-Finnegan TRITON Thermal Ionization Mass Spectrometer at Boston University. Neodymium is loaded onto single rhenium filaments with two μL combined H_3PO_4 and Ta_2O_5 slurry to facilitate ionization and measured as an oxide as in Harvey & Baxter (2009). Sm is loaded without this solution onto double

rhodium filaments and measured as a metal. For the duration of this study, in-house Nd standard solution (Ames metal) standards measured by the author give an average of $^{143}\text{Nd}/^{144}\text{Nd} = 0.5121190 \pm 0.0000081$ (15.7 ppm, 2RSD, $n = 26$) (see Appendix A). Long-term lab-wide reproducibility of $^{147}\text{Sm}/^{144}\text{Nd}$ is better than 0.1%. On average, blanks run through three columns or through dissolution and three columns were 10.4 picograms of Nd (see Appendix A).

3.1.2 Micro-sampled garnet geochronology

Zoned $^{147}\text{Sm}/^{144}\text{Nd}$ garnet geochronology has developed as a powerful tool to interrogate timescales of metamorphism. Researchers are able to place a duration on garnet growth by dating individual growth rings cut from a slice of a garnet, thereby supplying the critical time component often missing from discussions of metamorphism (Pollington & Baxter, 2010; Dragovic et al., 2012, 2015). Growth zones are segregated by micro-drilling with an automatic NewWave MicroMill drill. For this study, the eclogite samples of interest were too small for zoned sampling on a single garnet crystal. Instead, ~12 thin (0.5mm-0.8mm) slices were cut from sample 14BSY-35D, multiple porphyroblasts were drilled, and then their cores and rims were combined to create an adequate volume of core and rim material for geochronology (Fig. 2). Combining cores and rims from multiple crystals for dating requires that all garnets of a given size in the sample grew at the same time. Microprobe transects across multiple garnets along with qualitative element maps reveal that major element zonation is very similar for all crystals which is taken as evidence for contemporaneous growth- an important criteria if cores and rims from different crystals are to be combined (Fig. 2). Qualitative element

maps of garnets from this sample were made on the Tescan Vega 3 LMU variable-pressure scanning electron microscope with a LaB6 source at Boston College by M. Tappa. Garnet porphyroblasts larger than 5 mm in diameter in a given slice of rock were selected for drilling on the assumption that larger garnet cross sections represented a true cross section of garnet crystals. Each garnet was drilled to create a separate core and rim section. The drill trench was positioned on the crystal such that 75 % of the radius of the crystal was core and 25% was rim. The rim was drilled out from the matrix leaving a ~0.5 mm sliver of matrix around the perimeter of the rim to ensure that the very outermost rim was preserved. Approximately 30 crystals were drilled in this manner (Fig. 2). The sample is glued to a carbon block and drilled under water after (Pollington and Baxter, 2011). After drilling was completed for all crystals, the rims and cores from each garnet were combined and subsequently crushed and sieved to the standard grain size and then magnetically separated to remove matrix and inclusions. The two clean garnet separates were then subjected to the standard clean lab chemistry as bulk garnet separates. A “matrix” sample, that is, the garnet-absent bulk rock, was prepared by breaking off pieces of the drilled slices that had had garnets removed. The garnet-absent portions from several slices were collected, combined, and crushed and sieved to smaller than the 100 mesh. A garnet “powder” was prepared by crushing garnet to smaller than the 200 mesh.

3.1.3 Laser ablation for trace element concentration

Knowledge of the distribution of Sm and Nd in a garnet is important for the interpretation of Sm-Nd garnet ages. Laser ablation for trace element concentration was

performed on the Agilent 7500ce ICPMS coupled with a Geolas laser ablation system at Virginia Tech by J. Gorce. Samples were ablated with 193-nm ArF laser with a spot size that varied between samples from 60 to 90 microns. Analyses were standardized using an Fe(56) internal standard. Spot analyses contaminated by inclusions were removed. Because laser analysis did not provide spatial coordinates, images of laser pits with a scale bar were used to determine the location of measured points. The center of the garnet was chosen visually and laser pits were plotted as a distance from this center point. Concentrations of Sm and Nd were volumetrically averaged across each crystal using the spatial data obtained in this manner to determine a point of comparison for Sm and Nd concentrations measured with TIMS.

3.2 THERMODYNAMIC MODELING

The combination of minerals that is stable at a given pressure, temperature, and bulk composition can be calculated using thermodynamic principles. While this process has historically been quite laborious (e.g., Zen, 1966) computer programs have made the calculation of so-called pseudosections a powerful tool for even highly complex systems (ex: Connolly, 1990). The python-based program “Perple_X” was used to predict the pressure and temperature conditions of the initiation and cessation of garnet growth for four samples. Tracing a path between these two P-T conditions yields an approximate P-T path for the rock during peak metamorphism. The metamorphic evolution of the rock across this range allows calculation of water loss from the subducting lithology during

garnet growth. While equilibrium is never guaranteed for natural samples, eclogites from a mélangé present the dual problem of being relatively cold metamorphic rocks in a highly chemically heterogeneous setting. Nevertheless, there is a large literature using thermodynamic modeling to investigate such rocks (ie: Trotet et al., 2001b; Davis & Whitney, 2006; Cheng and Cao, 2015). This study attempts merely to add to the existing dialogue surrounding the metamorphic history of exhumed eclogites using the tools that are standard in the field.

3.2.1 Necessary data for Perple_X modeling

Bulk rock major element chemistry necessary for thermodynamic modeling is obtained from X-ray fluorescence (XRF) data (Table 1). A representative section of each rock was cut at Boston University and then crushed by the XRF lab. While none of the samples were strongly compositionally layered, care was taken to select a representative slice of rock by avoiding obviously late veins, removing weathered edges, and using a larger slice for coarser samples (see Appendix B for images of representative sections). X-ray Fluorescence data was gathered from two different institutions during the course of the study. Most analyses were carried out at Franklin and Marshall College on a Panalytical PW 2404 X-Ray Fluorescence Spectrometer by S. Mertzman. Two analyses were performed at the University of Massachusetts at Amherst on a Siemens MRS-400 multi-channel spectrometer by M. Vollinger.

Microprobe analyses for garnet transects and mineral compositions were obtained on the Cameca SX-50 Electron Microprobe at Virginia Tech by J. Gorce (Table 2). The

microprobe was run at a 20nA beam current with a 15 kV acceleration voltage. Major element mineral compositions for each sample were averaged from several probe points per mineral taken on different crystals in the thin section. Because garnet is strongly zoned, garnets composition was determined by volumetrically averaging the probe points along garnet transects. Garnet end members were calculated from oxide weight percent data normalized to 12 oxygen atoms. In calculating garnet's structural formula, ferric iron was determined to be insignificant in so four end-members - spessartine ($Mn_3Al_2Si_3O_{12}$), grossular ($Ca_3Al_2Si_3O_{12}$), almandine ($Fe_3Al_2Si_3O_{12}$), and pyrope ($Mg_3Al_2Si_3O_{12}$), were used (Figs 3, 4, 5, 6, and 7).

Mineral modes were determined by point-counts on thin sections but were adjusted slightly (within a few percent) if Mn in the bulk rock XRF was too low to account for garnet abundance. That is, if when the point-count garnet volume percent was subtracted from the bulk rock XRF, the Mn in the garnet absent composition was below 0, the garnet volume percent was adjusted very slightly until the Mn in the XRF remained positive. This approach is justified because the block of rock powdered for XRF and the billet cut for a thin section are, even if cut from adjacent parts of the rock, still separated by a few cm and can have slightly different amount of given minerals, especially large porphyroblasts.

3.2.2 Modeling garnet growth and water loss

The start of garnet growth is modeled by running *Perple_X* with the composition of the bulk rock as determined by XRF. Garnet core isopleths are plotted in P-T space for the modeled XRF composition. The point in P-T space where these four isopleths

intersect is the point where predicted garnet chemistry matches garnet chemistry measured with the microprobe and is thus the P-T conditions for the start of garnet growth. Predicted mineralogy at this P-T location is not expected to match what is seen in the rock today but can be useful to compare to inclusions in garnet.

When modeling the growth of a resistant porphyroblast such as garnet, researchers have determined it is important to adjust bulk rock chemistry as the phase grows and sequesters elements (ex: Marmo et al., 2002, Konrad-Schmolke et al., 2005). Accordingly, conditions of garnet rim growth are modeled by converting the total observed volume percent garnet to weight percent, subtracting this weight percent from the bulk rock and re-calculating the new garnet-absent oxide weight percent for each element. This garnet-absent composition is referred to as the “matrix.” This method assumes a garnet density of 4.05 g/cm^3 . Garnet rim isopleths are plotted in P-T space for the matrix composition and their intersection identifies the P-T location of the end of garnet growth. For two samples, garnet rim composition was either unable to be modeled or was not desirable for modeling (ie. was a resorption rim). In these cases, a point inside of the rim, towards the garnet interior, was chosen. The volumetric proportion of the garnet inside of this point was calculated and this volumetric amount was converted to a weight percent and subtracted from the whole rock. To avoid a resorption rim for sample 14BSY-35D, a point was chosen which was 144 microns from the physical rim and outside of 75% of the garnet volume (Fig. 5). For sample 14BSY-37A the true rim was unable to be modeled so a point 28 microns inside of the rim and outside of 90% of the garnet volume was chosen (Fig. 6).

Once a P-T path for garnet growth is established, water loss over this window can be calculated. This study uses the method reported in Dragovic et al., (2012) to account for both apparently overstepped garnet-in reactions (for garnet cores) and the decision to model a garnet-absent matrix (for garnet rims). The garnet-forming reaction can be considered to be overstepped when the measured garnet core chemistry is observed in models at a point in P-T space past the garnet-in line. If the weight percent water determined by Perple_X at this point in P-T space were to be used as the starting weight percent water for garnet growth, the predicted volume percent garnet would make the starting weight percent water in the rock appear lower than if there were truly no garnet in the rock. To account for this, we calculate rock weight percent water at the start of garnet growth by taking the mineralogy predicted by modeling at the garnet core P-T conditions, forcing garnet to a volume percent of 0, and then re-calculating weight percent water in the new garnet-free mineralogy. Similarly, the weight percent water in the rock at the conditions of garnet rim growth must also be adjusted. Because the rim is modeled using a bulk rock composition calculated by removing the volume percent garnet observed in hand sample from the whole rock XRF data, this removed garnet must be added back in to the predicted mineralogy at the rim P-T conditions before weight percent water is calculated. This is done in the same manner as the core garnet correction; the modal mineralogy predicted by modeling is obtained and the garnet abundance forced to the amount observed in hand sample or thin section. Weight percent water is re-calculated using this new increased-garnet modal mineralogy. If the sample was not able to be modeled to the completion of garnet growth, as was the case for 14BSY-35D and 14BSY-37A, the modal abundance of garnet was forced to the percentage of garnet that

was able to be modeled. For 14BSY-35D, because only 75 volume percent of the garnet was able to be modeled, the modal abundance of garnet was adjusted to be 75% of the amount observed in the sample. Similarly, for 14BSY-37A, the modal abundance of garnet was adjusted to be 90% of the amount observed in the sample.

The amount of water lost from core to rim of garnet growth can be expressed as moles of water per mole of garnet grown as in Dragovic et al. (2012). This is calculated by taking the predicted mineralogy and water content at conditions of core growth and comparing it to the *adjusted* predicted mineralogy and water content at the conditions of rim growth. The difference between the moles of each mineral at core and rim conditions is taken, including that for garnet and water. These numbers are then normalized to one mole of garnet, allowing a calculation of moles of water lost per mole of garnet grown.

In order to compare the predicted mineralogy at rim conditions to that observed in hand sample, the predicted mineralogy is adjusted differently than it is for the water loss calculation. For the mineral mode comparison, the garnet which was removed to create the matrix composition is added back in. This is different than forcing the garnet to be what is observed in the rock and allows an assessment of how well the program modeled the rock.

All samples were modeled using the same thermodynamic dataset and the same solution models. Perple_X version 6.6.8 (Connolly, 2009) was used with mineral end-member thermodynamic data from Holland and Powell (1998) and updated by the authors in 2004 (“HP04”). The solution models and details of run parameters are given in Appendix C. All models were run in fluid saturated conditions. This fluid was a binary H₂O-CO₂ solution. Carbon dioxide in the fluid was systematically varied from 0 to 0.05

mole % to 0.1 mole % for each sample to find the best parameters to create accurate garnet isopleth intersections modal mineralogy. In several instances, CO₂ in fluid had no effect on isopleth intersections and in these cases CO₂ was added only if the rock had optically visible carbonate mineralogy. In the absence of CO₂ in the fluid, the sample was run in a pure H₂O solution. Major element oxide weight percent from XRF data includes Fe₂O₃ weight percent determined by titration. This reported Fe₂O₃ is interpreted as the maximum ferric iron in the bulk rock because the titration process is slightly oxidizing. Ferric and ferrous iron ratios were varied from no ferric iron to, in some cases, the maximum ferric iron ratio reported by XRF analysis. The ferric iron to total iron ratio that yielded garnet isopleth intersections and modal mineralogy closest to those observed in the sample was chosen for each sample. Optimal Fe₂O₃/Fe_{tot} values ranged from 0.09 to 0.27. Samples 14BSY-38A and 14BSY-38B lack ferric iron titration data, and in these cases the general range of iron ratios in other samples was used as a guide.

The amount of carbonate in the fluid and the amount of ferric iron in the system have a large impact on the predicted mineralogy and can change the location of garnet isopleth intersections. These are also the least constrained parameters for our modeling process. To explore the sensitivity of the modeling results to changes in these two parameters, the whole-rock XRF composition for sample 14BSY-37A was run with Fe₂O₃/Fe_{tot} ratio of 0, 0.20, and 0.40 and a mole percent CO₂ in fluid of 0, 0.1, and 5 (Fig. 8). The high Fe₂O₃/Fe_{tot} ratio of 0.40 was chosen based on the higher end of the titrated values provided during XRF analysis. The high of 5 mole percent CO₂ in fluid was chosen to be slightly higher than the maximum value calculated by Schumacher et al. (2008) of 3 mole percent CO₂ in fluid. Two trends with implications for garnet isopleths

are immediately apparent in Figure 8. First, with increasing CO₂ in fluid, garnet stability is pushed to lower pressures and higher temperatures, as Mn-bearing carbonate is stable over a greater P-T range. The garnet-in reaction line can be seen to sweep to the right across the diagrams as CO₂ in fluid increases. Second, as the amount of ferric iron increases, the almandine isopleth moves to higher pressures. With these two parameters for which we have minimal real-world constraints, we are able to move the garnet stability in temperature space and garnet composition in pressure space. While this might be somewhat concerning, as seen in Figure 8, models did not yield good isopleth intersections in very many instances. The garnet isopleth intersections and modal mineralogy were used as the best way to constrain Fe₂O₃/Fe_{tot} ratio and mole percent CO₂ in fluid. Sample 14BSY-37A is the example shown in Figure 8; here the optimal values were determined to be Fe₂O₃/Fe_{tot} = 0.09 and CO₂ = 0 which is not shown in Figure 8 but is shown in Figure 17.

4.0 SAMPLE DESCRIPTIONS

The term “eclogite” here is taken to mean any rock with a primarily omphacite and garnet assemblage. Several of the samples studied include a substantial amount of white mica and several show evidence for rehydration in the form of large glaucophane crystals that overprint an earlier structural fabric. These eclogite samples are distinct from the other high pressure metamafic rocks on the island; omphacite-bearing but garnet-absent metagabbro and the glaucophane-dominated garnet-bearing blueschists. This study focuses exclusively on eclogitic rocks for three reasons. First, in exploratory work on samples collected from Syros, eclogites were the best candidates for $^{147}\text{Sm}/^{144}\text{Nd}$ garnet geochronology. Eclogitic samples were adequately cleansed of inclusions in the lab process while blueschist and mica-schist samples were not (see Appendix A). Second, as this study is concerned with water loss from the subducting slab and eclogites are the most dehydrated subduction zone rocks, studying eclogites allows us to potentially see the greatest water loss possible from rocks of a given composition. Finally, the only other garnet ages on Syros were performed on eclogitic rocks (Lagos et al., 2007) so focusing this study on eclogites will facilitate direct comparison with this previous study.

All samples with the exception of 06MSY-6E were taken from the Katergaki peninsula on the south of the island (Fig. 1). Sample 06MSY-6E was taken from the Kini peninsula on the west side of the island (Fig. 1). Both the area around Kini and the area

around Katergaki are mapped as metabasic rocks (Keiter et al., 2011). However, the Kini beach area also has outcrops of the serpentinite mélangé with “knockers” (Fig. 1). Sample 06MSY-6E, therefore, represents a fundamentally different setting than the four other samples. Importantly, the location near Kini is the same area where Lagos et al. (2007) collected one of three eclogitic samples for Lu-Hf garnet geochronology. 06MSY-6E is a coarse-grained eclogite-facies sample with the most ultramafic composition of any of the samples analyzed. It is dominantly composed of large ~0.5 cm garnet (40%), omphacite (29.3%) and glaucophane (17%) with minor amounts of rutile, chlorite, epidote, white mica, and carbonate (Fig. 9A). Two texturally distinct regions can be identified in the thin section. The first makes up about 80% of the thin section and contains intergrown omphacite and glaucophane with abundant garnet and large rutile grains (Fig. 10A). The rutile in this sample is particularly striking as it makes up about 6 vol% of the rock and occurs as large clots rather than distinct needles. This region is taken to be the most texturally representative region of the bulk rock and was consequently used for point counting to determine composition. A second region is characterized by euhedral, chemically zoned omphacite surrounded by interstitial glaucophane and a lack of both garnet and rutile. Omphacite in this region displays visually striking concentric zoning increase in the jadeitic component and a decrease in the augitic component from core to rim. The glaucophane is chemically identical to the glaucophane in the first region. The first region has a later assemblage found in the matrix and as veins in cracks in garnet composed of chlorite-mica-epidote. Garnet inclusions consist of epidote-iron-oxide-chlorite-zircon-albite. Albite inclusions display a symplectitic texture and are interpreted to result from breakdown of jadeite, indicating

that garnet grew while omphacite was stable. Chlorite inclusions are chemically distinct from later chlorite in the matrix, with inclusions having a higher iron component and matrix crystals having a higher magnesium component (Table 2).

14RSY-8A is a fine-grained mica-rich eclogite. The sample is composed mainly of omphacite (46%) and mica (36%) which together make-up a medium-grained matrix. Coarser grained calcite, Mn-Fe carbonate, garnet, blue amphibole needles, rutile, and sphene are present as porphyroblasts (Fig. 9B). Garnet inclusions consist of blue amphibole-apatite-rutile-Mn-Fe-carbonate. A later growth event is seen in a calcite vein with minor mica that cross-cuts garnet, amphibole needles, and the matrix. This sample is from the Katergaki peninsula area and in outcrop appeared as a fractured pod shot through with carbonate veins in a marble matrix.

14BSY-35D is a fine-grained eclogite. The matrix is dominantly omphacite (53%) and white mica (30%) with garnet porphyroblasts (10%) and minor glaucophane needles (1%) that form a lineation (Figs. 9C and 10B). Minor calcite was seen in the matrix. Garnet porphyroblasts vary from ~ 3mm to 5 mm in diameter. The sample was found in the field as float on the Katergaki peninsula.

14BSY-37A is a fine-grained eclogite with abundant small (0.5-2mm diameter) garnets. The sample is mostly omphacite (65%) and garnet (15%) with some epidote (7%) and large glaucophane needles (7%). Quartz and rutile are minor components (Fig. 9D). Garnet inclusions consist of large quartz-epidote-rutile- pyroxene (Fig. 10C). Calcite was seen as an inclusion in garnet but was not observed optically in the matrix, though in hand sample small later carbonate veins were visible. The omphacite, which makes up the majority of the sample, occurs as two optically and chemically distinct types. One has

a higher iron content, with more ferric iron. The other has a higher magnesium and aluminum content. Calcium and sodium differ very little between the two types and both are compositionally omphacite (Table 2). Only one pyroxene inclusion in garnet was analyzed and was found to be the more Mg-rich variety (Table 2). This sample was found as float on the Katergaki peninsula.

14BSY-38A has a fine-grained and homogenous matrix with a minor amount (3.9%) of small (~1 mm diameter) garnet porphyroblasts (Figs. 9E and 10D). The matrix is primarily composed of omphacite (73.6%) and mica (14.5%) with minor titanite-epidote-feldspar. Calcite in garnet and in mica-calcite veins makes up 6% of the sample. The sample was found as a small boudin in a quartz-mica-glaucophane schist on the Katergaki peninsula. The surrounding schist was collected as sample 14BSY-38B and was used as a point of comparison for 14BSY-38A but no garnet was dated from sample 14BSY-38B.

5.0 RESULTS

5.1 GEOCHRONOLOGY

Garnets were cleaned using the partial dissolution procedure describe above. An average of about 100 mg of crushed, picked and magnetically-separated garnet were put into partial dissolution. The smallest amount used was 29 mg while the largest was 150 mg. The average sample loss following the entire partial dissolution procedure was 75% of the starting sample weight. The lowest loss was 21% and the highest was 99.5%. Garnet samples were put in HF during partial dissolution for 15 to 180 minutes. Percent loss and time in HF necessary to yield an acceptable $^{147}\text{Sm}/^{144}\text{Nd}$ ratio for garnet geochronology varied between samples (Table 3). Isochrons for all samples were constructed with multiple garnet measurements of varying cleanliness and a single measurement of a representative piece of the whole rock (Fig. . Once sample, 14RSY-8A, includes two measurements of two different representative pieces of the whole rock. Sample 06MSY-6E includes a measurement of the leachate from the partial dissolution procedure. Garnet measurements were excluded from the isochron in the event of laboratory error resulting in an imprecise measurement (sample 14BSY-37A gts 5, 6; sample 14RSY-8A gts 5, 7) or inadequate cleaning resulting in a low $^{147}\text{Sm}/^{144}\text{Nd}$ value which falls off the isochron defined by higher $^{147}\text{Sm}/^{144}\text{Nd}$ measurements (14RSY-8A gts

1, 4; 14BSY-35D gt 3). All measurements, including measurements not included on isochrons, are reported in Table 3.

Samples 14BSY-35D, 14BSY-37A, and 14BSY-38A resulted in robust isochrons (maximum $^{147}\text{Sm}/^{144}\text{Nd}$ ratio, low MSWD) (Fig. 11, Table 4). Sample 14BSY-35D gives an age of 48.1 ± 2.3 Ma (maximum $^{147}\text{Sm}/^{144}\text{Nd} = 1.22$, $n = 4$, MSWD = 2.4). Sample 14BSY-37A gives an age of 43.6 ± 1.6 Ma (maximum $^{147}\text{Sm}/^{144}\text{Nd} = 1.39$, $n = 6$, MSWD = 2). Sample 14BSY-38A gives an age of 44.7 ± 1.0 Ma (maximum $^{147}\text{Sm}/^{144}\text{Nd} = 3.9$, $n = 6$, MSWD = 1.4). Samples 06MSY-6E and 14RSY-8A failed to yield high $^{147}\text{Sm}/^{144}\text{Nd}$ ratios above 1 (Fig. 11, Table 4). The reasons for this are addressed in the discussion. A low $^{147}\text{Sm}/^{144}\text{Nd}$ ratio results in the age reported from these samples having higher uncertainty. Sample 06MSY-6E gives an age of 57.7 ± 6.3 Ma (maximum $^{147}\text{Sm}/^{144}\text{Nd} = 0.4$, $n = 10$, MSWD = 1.9). Sample 14RSY-8A gives an age of 48.8 ± 3.2 Ma (maximum $^{147}\text{Sm}/^{144}\text{Nd} = 0.49$, $n = 6$, MSWD = 0.67). The average age for all samples studied is 48.5 Ma. The average age for the three successfully cleaned samples (with maximum $^{147}\text{Sm}/^{144}\text{Nd} > 1.0$) is 45.4 Ma.

Sample 14BSY-35D was microdrilled for geochronology to obtain a core and rim age to quantify the rate of garnet growth. Thirty-nine garnet crystals were microdrilled from 12 slices of the sample to generate 38 rims and 31 cores (not every garnet generated a core and a rim as sometimes material crumbled or was lost through human error) (Fig. 2). Raw core material initially totaled 181.4 mg. After crushing, sieving, and magnetic separation the 140-230 mesh fraction yielded 89.0 mg of garnet core (51% sample loss). Raw rim material initially totaled 847 mg. After crushing, sieving, and magnetic separation, the 140-230 mesh fraction weighed 203 mg (76% sample loss). Greater

sample loss during rim processing is due to matrix material included with rims during drilling being lost during magnetic separation. Material smaller than the 230 mesh size was set aside to be measured as the “powder” fraction. This material represents the equivalent of garnet with inclusions still present. Unfortunately, despite using the same partial dissolution cleansing procedures on these garnets as for all other samples, neither core nor rim yielded high $^{147}\text{Sm}/^{144}\text{Nd}$ above 1.0, resulting in less precise ages. A core isochron with the whole rock, core powder, and core garnet gives an age for core growth of 66 ± 15 Ma (maximum $^{147}\text{Sm}/^{144}\text{Nd} = 0.23$, $n = 3$, $\text{MSWD} = 0.76$) (Fig. 12, Table 4). The large amount of rim material allowed two partial dissolution attempts. An isochron with the matrix, rim powder, and two rim garnets gives an age for rim growth of 47.1 ± 3.0 Ma (maximum $^{147}\text{Sm}/^{144}\text{Nd} = 0.55$, $n = 4$, $\text{MSWD} = 1.4$) (Fig. 12, Table 4).

5.2 TRACE ELEMENT CONCENTRATIONS

Trace element concentrations were measured in situ on a laser ICP-MS. Garnet transects consist of around five to 10 laser points across a crystal (Fig. 13). Sample 14RSY-8A lacked spatial data so a volumetric average and assessment of any zonation was impossible for this sample. For 21 out of 61 analyses, Nd was below the detection limit. The small number of points per sample, the potential error inherent in determining spatial coordinates from an image after the fact of measurement, and the lack of a second garnet analysis for any sample make assessment of patterns across garnets difficult and decidedly suspect. However, it can be reasonably asserted that three of the four samples for which we have spatial data show some zonation in trace elements. Sample 06-MSY-

6E is un-zoned in Sm or Nd but shows a marked zonation in Lu from 27 ppm at the core to ~0.2 ppm at the rim (Fig. 13). 14BSY-35D is un-zoned in Nd but shows a slight decrease in Sm concentration towards the rim from 0.89 ppm to 0.62 ppm. The change is so slight, however, that the volumetric Sm average (0.69 ppm) is barely higher than the lowest measured concentration (0.62 ppm). Lu, however, changes from 5.2 ppm at the core to 0.8 ppm at the rim (Fig. 13). 14BSY-37A has increasing Sm, Nd, and Lu concentrations towards the rim, however, this pattern relies on Nd and Sm concentrations in the rim so high that they are greater than what was measured with TIMS, suggesting that these points might be compromised by inclusions. If this is the case, then this sample shows no evidence for trace element zonation but it also possesses only three inclusion-free points: too few to determine any pattern (Fig. 13). 14BSY-38A shows higher Sm concentrations (0.8 ppm) in the core of the garnet than the rim (0.04 ppm) while only two of the points analyzed were above detection limits for Nd. Lutetium concentration is lower at the rims and core and higher in the region between (Fig. 13). This is in contrast to every other sample analyzed in this study which show a Lu peak in the center of the garnet, but non-Rayleigh determined Lu zonation is not uncommon in the literature (cf. Moore et al., 2013; Jedlicka et al., 2015). This increase in Lu corresponds to the first increase in Mn from core to rim seen in the garnet (Fig. 14). Evidence for what may have caused this strange zonation is seen in Na/Ti and K/Ti concentrations (Fig. 14). These ratios show a marked increase from core to rim from 0.4 to 7,138 (Na/Ti) and 0.03 to 37 (K/Ti) but do not line up exactly with the Lu and Mn pulses. Because Ti is relatively immobile while Na and K are highly mobile, the increase in these ratios is evidence that the rock saw an open system as the garnet grew and mobile elements were added to the

system. Perhaps Lu concentrations in the infiltrating fluid changed during garnet growth creating elevated Lu between the core and rim (ie Moore et al. 2013).

5.3 THERMODYNAMIC MODELING

Garnet chemistry was determined using the microprobe at Virginia Tech and at the University of Massachusetts. Garnets were on-average dominantly almandine-rich but included up to one third mole fraction grossular. Every sample shows a smooth bell-shaped Mn profile (Figs. 3, 4, 5, 6, and 7) with the exception of 14BSY-38A which shows inverse Mn zonation changing from 0.028 mol fraction spessartine in the core to 0.160 mol fraction spessartine at the rim. When seen on an element map, the Mn increase is strikingly “stepped” in three discrete zones rather than increasing continuously (Fig. 7). Sample 06MSY-6E shows a somewhat lopsided profile which is taken to be the result of asymmetrical garnet growth as the same garnet was probed twice on two different microprobes and yielded the same results. It shows a standard chemical zonation profile until a stepped increase in Mn and decrease in Fe at the rim. The stepped nature of this transition is interpreted to mean that it does not result from resorption but is instead the result of a hiatus in growth or an abrupt change in bulk composition from fluid infiltration (Fig.7). Samples 14BSY-35D (Fig. 5) and 14RSY-8A (Fig. 4) show evidence for garnet resorption in the form of increased Mn at the rim. Sample 14BSY-37A has an irregular ring of increased Mn inside of a rim which shows the standard Mn decrease. The rim is interpreted to result from later growth around an earlier, partially-resorbed core (Fig. 6).

All samples with the exception of 14RSY-8A were modeled using `Perple_X`. Sample 14RSY-8A did not give robust age data, has evidence for extensive CO₂ fluid infiltration, and preliminary modeling attempts revealed it to be unpromising for modeling garnet growth.

Whole-rock XRF data for 06MSY-6E gives excellent garnet core isopleth intersections when models are run at water saturated conditions (as all models in this study are) with no CO₂ in the fluid phase, and with $Fe^{3+}/Fe^{tot} = 0.09$. Garnet core isopleths intersect at 728 K and 2.25 GPa (Fig. 15, Table 5). The sample was modeled at 86% garnet growth, a point chosen because it is just to the core-side of a small but abrupt step in Mn and Fe zonation (Fig. 3). This matrix composition was modeled with no CO₂ in the fluid phase and with $Fe^{3+}/Fe^{tot} = 0.21$ (Table 5). The ferric iron amount was chosen by simply subtracting garnet, which contains exclusively ferrous iron, from the initial 9% ferric whole rock composition. Eighty-six percent garnet growth isopleths intersect at 800 K and 2.39 GPa (Fig. 15). The spessartine fraction does not occur in the modeled space but is very low (0.006 mol fraction). Garnet rim composition was modeled, again with no CO₂ in the fluid and the ferric iron resulting from further garnet removal: $Fe^{3+}/Fe^{tot} = 0.27$. Rim intersections occur at 868 K and 1.74 GPa. Again, the measured mole fraction spessartine does not occur in the modeled space but is, again, very low (0.006).

Sample 14BSY-35D yields a garnet core isopleth intersection at 775 K and 2.32 GPa when the XRF composition is run with no CO₂ in the fluid at $Fe^{3+}/Fe^{tot} = 0.09$ (Fig. 16, Table 5). Because this sample has a resorption rim, the conditions of rim growth cannot be determined by the present day composition of the physical edge of the garnet. The microprobe point with the lowest mole fraction spessartine is considered to represent

the best composition to model garnet growth. This point is, unfortunately outside of only 75% of the garnet's volume (Fig. 5). The matrix was run with no CO₂ in the fluid and at Fe³⁺ /Fe^{tot} = 0.10 (Table 5). This was the only sample for which the Fe³⁺ /Fe^{tot} ratio could not just be allowed to evolve naturally with garnet subtraction. If the system was allowed to become more ferric due to garnet removal, the almandine component in modeled garnet was far lower than what was measured with the microprobe. Artificially altering the Fe³⁺ /Fe^{tot} ratio to be lower (increase the ferrous portion) increased the almandine component but it still barely plotted within the modeled P-T space. Isopleths for the 75% rim do not intersect well in the modeled pressure-temperature space and the mole fraction spessartine is so low as to not occur. The best intersection occurs at ~ 803 K and 2.42 GPa (Fig. 16)

Sample 14BSY-37A produces good core intersections at 755 K and 2.30 GPa when the XRF composition is run with 0.05 percent CO₂ in the fluid at Fe³⁺ /Fe^{tot} = 0.09 (Fig. 17, Table 5). The pyrope isopleth does not intersect well with the other three but this is the lowest mole fraction at the core so its poor intersection barely influences the others and was considered negligible. When all garnet is removed from the system, the rim isopleths cannot, with any combination of ferrous iron and carbon dioxide amount, be modeled. Thus, the next microprobe analysis in from the rim at 90% of the total garnet volume was modeled by subtracting 90% of the garnet from the whole rock. Additionally, 50% of the small amount of quartz in the sample was subtracted. This was to account for the fact that about half of the quartz totaled in the point count was present as an inclusion inside garnet (Fig 10C). When garnet grew this quartz was presumably sequestered. The matrix composition was run with 0.1% CO₂ in the fluid and at Fe³⁺ /Fe^{tot}

= 0.15, which is the ferric ratio produced when the garnet is removed from the whole rock (Table 5). Isopleths intersect well with the exception of the spessartine mole fraction which is not particularly far away in P-T space from the other three and, at 0.024, is the lowest mole fraction at the rim (Fig. 17).

Sample 14BSY-38A was unable to be modeled with the bulk rock composition or the garnet-absent matrix composition (Table 5). The bulk rock composition run with 0.1% CO₂ in the fluid at a Fe³⁺ /Fe^{tot} = 0.09 does not produce garnet which contains any of the garnet end-members in the measured amounts anywhere in the modeled pressure temperature space with the exception of the spessartine component at the rim (Fig. 18). No combination of carbon dioxide in fluid and iron oxidation states resolves this problem. The matrix composition tried at a similar range of conditions fails to grow any garnet at all, even though the system still contains 0.01 wt. % MnO which in other modeled samples was sufficient to grow garnet. Given the extensive evidence for open system behavior (the sample is a small boudin in a chemically different surrounding rock, has stepped Mn zonation with no evidence of resorption, and has unusual trace element patterns), it is reasonable to conclude that the chemical make-up of the sample today is not representative of the composition of the sample at the start of garnet growth or even at the cessation of garnet growth. Garnet growth in sample 14BSY-38A cannot be modeled with the thermodynamic modeling techniques applied to the other samples in this study.

5.4 THERMODYNAMIC MODELING AND WATER LOSS

Water loss during garnet growth is greatest for sample 06MSY-6E. Note that all thermodynamic modeling assumed initially water saturated conditions; thus calculated dehydration fluxes are maximum amounts. If starting compositions were not water saturated the actual dehydration would be lower. These calculations thus reflect a maximum capacity for initial water storage and subsequent loss. From core to rim this sample lost 5.13 weight percent water from the bulk rock (Table 6). The majority of this water loss (4 weight percent) occurred during the first 86 volume percent of garnet growth on an increasing-pressure and temperature path. The final 14 volume percent of garnet growth corresponds to the remaining 0.4 weight percent water loss and occurs on a decompression path. The next-greatest water loss during garnet growth is for sample 14BSY-35D. The sample lost 2.60 weight percent water during the 75 volume percent of garnet growth, which we were able to model on an increasing pressure and temperature path (Table 6). Sample 14BSY-37A lost 1.09 weight percent water during garnet growth on a decompression heating path (Table 6). The loss-on-ignition measured during XRF analysis is consistently greater than what is calculated at the end of garnet growth (Table 6). This can be explained by either the presence of carbonate or late rehydration. For example, sample 14BSY-37A presently contains ~7 vol percent glaucophane which, based on textural and chemical data is determined to be late (see previous sample description).

6.0 DISCUSSION

6.1 CHALLENGES AND SUCCESSES WITH SM/ND GARNET

GEOCHRONOLOGY

The largest challenge with $^{147}\text{Sm}/^{144}\text{Nd}$ geochronology is to effectively remove contaminating inclusions from the garnet so that the Sm and Nd isotopic signature from the inclusions do not mask the signature from pure garnet. This study had mixed results with the partial dissolution method but ultimately, three of the five samples were successfully cleansed of inclusions. Samples 14BSY-35D, 14BSY-37A, and 14BSY-38A all gave Sm/Nd ratios above 1 (generally considered the minimum ratio to ensure that contaminating inclusions have been adequately removed) for at least two garnet separates (Baxter and Scherer, 2012) (Table 3). Sample 14BSY-37A has Sm and Nd concentrations exactly in line with the lowest concentrations measured using LA-ICMPS, confirming that the material being measured on the TIMS after the laboratory procedures was, in fact, clean garnet (Fig. 13). Samples 14BSY-35D and 14BSY-38A have Sm concentrations in line with the lowest concentration measured with LA-ICMPS but have Nd concentrations above what was measured with LA-ICPMS (Fig. 13). This suggests that the garnets for both samples are not entirely cleaned and the true Nd concentration is lower. Whatever inclusions are left in these samples, they don't seem to be pulling the

garnet points *off* the isochron, just slightly *down* along the isochron. The MSWD for each sample indicates that the points statistically form a line, so they are not being perturbed off the isochron by inclusions (Fig. 11, Table 4).

Samples 06MSY-6E and 14RSY-8A were unable to be successfully cleaned during the partial dissolution procedure; neither sample had a garnet separate achieve a $^{147}\text{Sm}/^{144}\text{Nd}$ ratio above 1 (Fig. 11). Laser ablation ICPMS data reveals Nd and Sm concentrations in pure garnet well below those measured on the TIMS for 06MSY-6E, indicating that higher Nd and Sm concentration inclusions were contaminating the sample even after partial dissolution (Fig. 13). Laser ablation ICPMS for sample 14RSY-8A shows Nd concentrations only slightly lower than what was measured with the TIMS, a discrepancy similar to that seen with “clean” samples described above (Fig. 13). Given the low $^{147}\text{Sm}/^{144}\text{Nd}$ ratios it is surprising that concentration data is not more affected. It is possible that even the LA-ICPMS data is compromised by micro-inclusions smaller than the spot size.

Something about both samples makes them difficult or impossible to clean with the usual partial dissolution procedure. Previously, students working on garnet geochronology in this lab have identified epidote (Ramos, 2015), tourmaline (Stewart, 2015) and aluminous pyroxene (M. Cahill, personal communication, 8 Apr. 2016) as inclusions that might dissolve more slowly than, or at the same speed as, garnet in hydrofluoric acid. Were an inclusion to behave this way it would not be removed during the partial dissolution procedure. Figures 19 and 20 shows the isochrons for the uncleaned samples with every garnet that was measured. Note that the age reported in this figure for sample 14RSY-8A differs from the age given previously for that sample

because garnets with low $^{147}\text{Sm}/^{144}\text{Nd}$ ratios or extremely large error bars were excluded from the original age calculation. Also note that for 14RSY-8A, minutes in HF during the partial dissolution do not correlate exactly with an increase in the $^{147}\text{Sm}/^{144}\text{Nd}$ ratio. This is because two different garnet grain sizes were used during sample preparation (Fig.19, Table 2). The finer grain size requires less time in HF to reach the same $^{147}\text{Sm}/^{144}\text{Nd}$ ratio as the coarser grain size. If garnets 5, 6, 8, and 9 (garnets are numbered in Fig. 19) are considered, it seems clear that more time in hydrofluoric acid during the partial dissolution is, in fact, increasing the $^{147}\text{Sm}/^{144}\text{Nd}$ ratio by removing inclusions from the garnet. It also seems clear, however that this sample has hit the limit of that method; 99% of the sample was dissolved away at the “cleanest” point. Some inclusion in this sample must be dissolving at only a very slightly faster rate than garnet. That it does not change the concentration very much but distorts the isochron suggests that it is a low concentration phase with a very different isotopic composition than the garnet. If the issue is instead tourmaline or aluminous pyroxene, then there is no known way to optimally prepare this sample for $^{147}\text{Sm}/^{144}\text{Nd}$ garnet geochronology and it might be better dated with some other method.

Sample 06MSY-6E presents a slightly different picture. While it is true that garnet separates left in hydrofluoric acid for longer amounts of time lose more garnet, this does not always correlate with a higher $^{147}\text{Sm}/^{144}\text{Nd}$ ratio (Fig. 19). This suggests that some problematic inclusion is dissolving at the same rate as garnet and is present in different separates in different quantities by simple chance. Garnet 8 (see Fig. 20 for garnet numbers) was treated to a slightly different procedure than the rest. This garnet separate was put into hydrofluoric acid twice during the partial dissolution with a nitric

acid step in between. The two HF steps are greater than the sum of their parts; a 95 minute HF step followed by a 60 minute HF step generated a cleaner garnet separate than a 154 minute continuous HF step. Perhaps whatever phase is a problem quickly reaches its saturation point in 2 mL of HF while garnet continues to dissolve. If the acid is refreshed, the contaminating phase is dissolved more relative to garnet.

While bulk garnet geochronology proved successful for sample 14BSY-35D, the same sample preparation and partial dissolution procedure carried out on the rim and core separates was a failure. Garnet from the cores of crystals was not cleaned by the partial dissolution process while garnet from the rim was cleaned to a lesser extent than would be predicted by the results from the bulk garnet separate (Fig. 12). This is distinct from the problems described above where something intrinsic to the sample creates a problem for the standard inclusion cleansing procedure. Rather, something seems to have gone wrong during sample preparation or in the lab to make the previously-successful methods fail. It is intriguing, however, that when the prepared rim material was split into two parts and run through clean lab procedures separately and weeks apart (rim 1 and rim 2) the garnet separate seems to have behaved the same way in the partial dissolution. That is, a slightly longer time in the hydrofluoric acid step increased the $^{147}\text{Sm}/^{144}\text{Nd}$ by a small amount consistent with the first rim separate and inconsistent with the bulk separate. This suggests that whatever went wrong happened prior to clean lab work during sample preparation. Further, whatever went wrong affected the core more than the rim. While no explanation can presently be offered, it is worth noting that the rim powder plots at a lower $^{143}\text{Nd}/^{144}\text{Nd}$ ratio than would be expected if the rim powder was the result of mixing between the matrix and garnet material.

The three samples discussed above (06MSY-6E, 14RSY-8A, and the core from 14BSY-35D) do not yield precise ages but it is still possible that accuracy is not affected. If this is true, the imprecise but accurate age may still be useful for geologic interpretations.

The $^{147}\text{Sm}/^{144}\text{Nd}$ ratios for garnet points for sample 14RSY-8A are low. This, along with large error bars, contributes to the imprecise age. If a two-point isochron is made between a whole-rock point and each garnet point individually, there is a negative trend apparent between two-point isochron age and the $^{147}\text{Sm}/^{144}\text{Nd}$ of the garnet (Fig. 19, lower panel). This suggests that there is a non-garnet inclusion mixing with the clean garnet pulling it off the isochron. This inclusion pulls the isochron to older ages because as the garnet gets cleaner, the age decreases. Error bars on the two-point ages are large, however, and most ages overlap within error. The bulk age is, with the present data, older than the three best-constrained ages. Based on the trend described above, cleaner garnets would continue to pull the isochron to a younger age. The present age shows evidence of contamination from a phase not on the isochron and will not be used to interpret the geologic history of Syros.

Sample 06MSY-6E is the oldest bulk sample, even if the youngest point within the very large error bars is considered. In a plot of two-point isochron age and $^{147}\text{Sm}/^{144}\text{Nd}$ of the garnet measurement used to calculate the age, there is a positive trend; the opposite of the trend seen with 14RSY-8A (Fig. 20). The cleaner the garnets, the more the isochron is pulled to older ages. This suggests the presence of a contaminating inclusion which does not fall on the isochron and pulls the sample to younger ages, making the multi-point garnet age inaccurate. However, just as with sample 14RSY-8A,

the error bars on the two-point ages are so large as to make most the ages overlap within error and the positive linear trend seen in Figure 20 is defined mostly by garnet 8.

Regardless of whether the exact age calculated with the multi-point garnet isochron is accurate, what can be asserted is that this age is already older than any other ages in this study and at least one cleaner garnet point pulls the isochron to even older ages. This sample can be used to interpret the geologic history of the island; it is not only the most mafic, implicated in the most water loss, and from a different region of the island from the other samples, but it seems also to have a fundamentally different garnet growth history.

Zoned work on 14BSY-35D resulted in a core which suffers from poor precision and a maximum $^{147}\text{Sm}/^{144}\text{Nd}$ at 0.23 (Table 4). While it is reassuring that the core is older than the bulk garnet separate, suggesting that any contaminating inclusion is, at worst, pulling the isochron to older ages, the $^{147}\text{Sm}/^{144}\text{Nd}$ is so low that the accuracy of the age is highly uncertain. The rim presents a slightly better picture with reasonable precision but a fairly low maximum $^{147}\text{Sm}/^{144}\text{Nd}$ of 0.55. The rim is younger than the bulk garnet separate but error bars on both the rim and the bulk garnet are so large as to make them essentially indistinguishable. While the rim presents less cause for concern about accuracy than the core, it adds nothing new to the geochronology already established by the bulk garnet age.

6.2 REGIONAL IMPLICATIONS OF GARNET GEOCHRONOLOGY

Lagos et al. (2007) asserted on the basis of three Lu-Hf garnet ages with different Lu zonation from two locations on the island that Syros had seen one single high-pressure metamorphic event of a relatively brief (~2 Myr) duration centered at 52 Ma. In the present study, Sm-Nd ages refute the hypothesis that the Eocene HP-LT metamorphic event was short-lived and centered at 52 Ma; high-precision Sm-Nd garnet ages from this study span several million years and are up to 10 Ma younger than similarly robust Lu-Hf garnet ages from Lagos et al., (2007) (Fig. 21).

Is the spread in ages between the two studies due to differences between $^{147}\text{Sm}/^{144}\text{Nd}$ and $^{176}\text{Lu}/^{176}\text{Hf}$ dating or is there a geologic explanation? Differential diffusion rates and different closure temperatures of the isotopes used in the two dating methods has been argued to potentially create discrepancies between ages calculated with $^{147}\text{Sm}/^{144}\text{Nd}$ and $^{176}\text{Lu}/^{176}\text{Hf}$ (Bloch et al., 2015). However, modeled temperatures for the subduction zone rocks in this study are so low (maximum of 868 K/594 °C) that neither system would have been diffusively open (Bloch et al., 2015).

If the one older garnet age from this study (sample 06MSY-6E at $57.7 \pm 6.3\text{Ma}$) is disregarded on the basis of its low $^{147}\text{Sm}/^{144}\text{Nd}$ ratio and evidence for an off-isochron contaminating inclusion, then the simplest explanation for different garnet ages between the two studies might be the well-known preferential sequestration of Lu into garnet cores. However, Lagos et al., (2007) found this zonation in two of their garnets while the other garnet had more Lu at the rims. The differential Lu zonation between garnets giving overlapping ages was a large part of their argument that the metamorphic event was short lived. While presenting this data, they also discussed how it is difficult to accurately find

the middle of a garnet and mentioned that if the Lu peak were very narrow, they might have missed it. If this is the case, then the ~ 9 myr age span between precise ages in this study and precise ages in the Lagos et al., (2007) study can be attributed to sequestration of Lu into the core of garnets. Support for this comes from the fact that several garnets in this study were found to have large Lu peaks at the center of garnets, and that microsampled garnets on nearby Sifnos island showed ~8 myr of growth in a single crystal (Dragovic et al., 2012). Additionally, sample 14BSY-35D in this study gives an age intermediate between the old Lu-Hf ages and young $^{147}\text{Sm}/^{144}\text{Nd}$ ages ($48.1 \pm 2.3\text{Ma}$). This intermediate age could represent influence from an old core and a young rim.

If, however, the oldest garnet age in this study is (sample 06MSY-6E at $57.7 \pm 6.3\text{Ma}$), while not precise, is at least accurate, then the interpretation changes. Now the spread in ages between the two studies could have a geologic interpretation. It is worth noting, however, that while all other samples were found in outcrop, 14BSY-37A and 14BY-35D were collected as float on the Katergaki peninsula. There is no evidence that these rocks were transported from elsewhere so they are discussed below as having originated in the Katergaki peninsula area.

Of the three geographic areas (Katergaki, Kini, and Grizzas) from which eclogitic garnets were dated in this study and the Lagos et al., (2007) study, old ($>50\text{ Ma}$) and young ($<50\text{ Ma}$) ages do not occur in the same location. The oldest age in this study (sample 06MSY-6E at $57.7 \pm 6.3\text{Ma}$) is from near Kini, the same location as the Lagos et al. (2007) Ap21 which gave an age of $50 \pm 2\text{ Ma}$ (Fig. 1). These ages are in agreement within error, and with the Lagos et al. (2007) ages for eclogites further north from near

Grizzas (52.2 ± 0.3 Ma and 51.4 ± 0.4 Ma) (Fig. 1). The more southern Katergaki peninsula hosts samples that date from nearly 50 Ma (48.1 ± 2.3 Ma) to around 44 Ma (14BSY-37A at 43.6 ± 1.6 Ma and 14BSY-38A at 44.7 ± 1.0 Ma).

What is different structurally or lithologically between these three areas?

Unfortunately, this depends on which map you look at. Trotet et al. (2001a,b) map both the Grizzas and Kini locations as primarily “eclogite-blueschists” with some pods of “retrogressed blueschist” while they map the Katergaki location as the inverse: primarily retrogressed blueschist with pods of “eclogite-blueschist.” In their interpretation, this means that the Katergaki location was slightly lower in the structural pile compared to the other two locations and therefore underwent a similar prograde metamorphic history but a different exhumation history. A second lithologic and structural interpretation, which groups the two northern sites into a separate category from the Katergaki location, is that of Philippon et al. (2012), which deems Grizzas and Kini to be “meta-ophiolite” from the Pindos Ocean while Katergaki is mapped as being marble from the sedimentary cover of the ancient Adria micro-continent. In their interpretation, the Pindos Ocean rocks were thrust on top of the Adria sedimentary rocks during prograde high pressure metamorphism associated with subduction. In contrast to the above interpretations, Keiter et al. (2011) identify both Katergaki and Kini as “metabasic rocks” in a tectonic mélange but map Grizzas as being composed of “metavolcanics” and “metagabbro” that are “highly deformed” and were metamorphosed at high pressures. They do, however, include serpentinite outcrops in the metabasic rocks at Kini but omit them at Katergaki, allowing a small lithologic distinction between the two locations. In the process of conducting field work on the island, it was observed that the Kini and Grizzas locations

both host the classic *mélange* blocks rimmed with blackwall mineralization while the Katergaki location lacks obvious examples of these blocks and instead has more marble and quartz-mica schists.

If the two more northern sample locations can be both identified as an ophiolitic *mélange* from a structurally and lithologically distinct location from Katergaki, as in Trotet et al. (2001a, b) and Philippon et al. (2012), then this offers an explanation for the older ages in the northern two locations. The true tectonic *mélange* with a serpentinite matrix and eclogitic pods with blackwall rind grew prograde garnet earlier in the same metamorphic event than the tectonically different Katergaki location. Whether the Katergaki location is considered to be mostly retrogressed blueschist hosting some eclogite (Trotet et al., 2001a, b) or mostly marble hosting some eclogite (Philippon et al., 2012), the area is not ultramafic *mélange*. Even in the Keiter et al. (2011) interpretation, which maps Kini and Katergaki as the same unit, the Katergaki region lacks serpentinite. Perhaps during subduction the rocks of Katergaki were farther from the ultramafic *mélange* zone in an area with more sediment and less mantle material. These rocks and sediment started growing garnet later than the *mélange* zone rocks, perhaps simply because they entered the subduction zone slightly later. The P-T paths and conditions at which garnet grew will help to illuminate this.

Whether all rocks on the island experienced this metamorphism concurrently such that the age spans are simply related to HREE zonation or whether different lithologies in different structural positions experienced similar metamorphism at different times is unresolved. However, with either of these possibilities, the conclusion is the same: a conservative calculation - that is, ignoring the questionable 06MSY-6E age - is that high

pressure low temperature metamorphism on Syros spanned at least 52.2 ± 0.3 Ma to 43.6 ± 1.6 Ma, or a minimum duration of 8.6 ± 1.6 million years.

The possibility remains that sample 06MSY-6E is in fact much older than the age determined with the present low $^{147}\text{Sm}/^{144}\text{Nd}$ isochron and that cleaner garnet points would pull the isochron towards even older ages. In this case, the sample is not simply recording the earliest stages of the HP-LT metamorphic event but is instead showing evidence for a much earlier garnet growth event. Bröcker and Keasling (2006) dated jadeite blackwall material from the *mélange* in the northern part of the island using U-Pb in zircon and found ages of ~ 80 Ma. They argue that because jadeite is known to form exclusively by precipitation from high pressure fluids, this age must be a Cretaceous high pressure event distinct from the more broadly recognized Eocene event. Bröcker and Enders (1999) found the same age for zircons with inclusions of high pressure minerals (Fig. 22). The age of 57.7 ± 6.3 from sample 06MSY-6E is not as old as these ages but, as was discussed above, the trend in the sample is towards older ages as garnet is cleaned. If the linear relationship between garnet $^{147}\text{Sm}/^{144}\text{Nd}$ and two-point age seen in the lower graph in Figure 20 is extrapolated to 78 Ma, the corresponding $^{147}\text{Sm}/^{144}\text{Nd}$ value is 0.61 which is lower than that of a typical clean garnet $^{147}\text{Sm}/^{144}\text{Nd}$. However, as was mentioned above, this linear trend is defined by garnet 8; most of the other ages overlap within error (Fig. 20). The possibility that 06MSY-6E contains garnets that grew during a HP-LT event ~ 30 myr prior to the one during which most garnets in the study grew seems remote but is not ruled out by the data.

6.3 CHALLENGES AND SUCCESSES WITH THERMODYNAMIC MODELING

While the error associated with the geochronology presented in this study is rigorously quantified and expressed, the error associated with the thermodynamic modeling is not as well constrained. It can be difficult with heterogeneous metamorphic rocks to choose the correct equilibrium length scale, and it is little more than a guess to pick the ferric iron ratio and the amount and composition of fluid. All temperatures and pressures calculated from garnet isopleth intersections should certainly be considered approximate. Of note is that the three successfully modeled samples all show garnet overstepping by as much as 150 K. That is, the chemical composition of the garnet core occurs at a few volume percent garnet rather than at the predicted absolute initiation of garnet growth. This could be because we have failed to obtain perfect core transects or because reaction kinetics, along with thermodynamic principles, influence the growth of a phase and can lead to overstepped reactions (Carlson et al., 2015; Spear et al., 2014)

One way to assess the success of modeling is to compare the predicted mineralogy at the conditions determined for the termination of garnet growth to that determined from hand sample or thin section. The three samples for which rim P-T conditions could be reasonably established match predicted mineralogy with actual mineralogy to different extents (Table 7).

For sample 06MSY-6E, predicted mineralogy at termination of garnet growth is 45.6 vol% garnet, 27% clinopyroxene, 21.5% amphibole, 3% rutile, 2.3% chlorite, and 0.5% biotite (Table 6). This is broadly consistent with what is observed in hand sample (Fig. 9). The model slightly over-predicts garnet volume percent and amphibole while

under predicting clinopyroxene and rutile, but this variability is minor. Chlorite was measured with the microprobe and it was noted that chlorite occurring as inclusions in garnet had a higher Fe content than chlorite in the matrix which looked texturally late (Table 2). Chlorite composition predicted at core P-T conditions contains 3.3 mol FeO per formula unit and 1.7 mol MgO per formula unit, while that predicted at both rim compositions contains about 1.7 mol FeO and 3.3 mol MgO. Interestingly, magnesium-in-amphibole (MgO = 2.3 mol per formula unit), as measured on the microprobe (Table 2) and then plotted as an isopleth on each pseudosection, comes close to the location in P-T space of the rim but intersects best with the 86% garnet growth P-T location (Fig. 15). A silica-in-mica isopleth ($\text{SiO}_2 = 3.3$ mol per formula unit) plotted on each pseudosection also intersects the 86% garnet growth P-T location best (Fig 15). In fact, mica loses stability at higher pressure such that no mica and only biotite is predicted for the rim composition. No biotite is observed in hand sample. Mica and/or biotite are both predicted and observed to be very minor volumetric contributors to the rock so it is possible that minor biotite was optically overlooked. Or, as some have suggested, it is possible that the biotite model over-predicts the stability of biotite in these high pressure conditions (M. Caddick, personal communication, 26 June 2016.) and that the stability field of mica should be slightly larger which might make it stable at the rim conditions. This, however, is pure speculation. Overall, Mg in amphibole and Fe and Mg in chlorite support the location in P-T space of garnet rim growth.

Predicted mineralogy at 90% of garnet growth for sample 14BSY-37A is 79.5 volume percent clinopyroxene, 12.7% garnet, 3.3% lawsonite, 3.2 % dolomite, 1.0% mica, 0.2 % rutile and 0.1% amphibole (Table 7). This cannot be directly compared to the

mineralogy observed in thin section and hand sample because obviously that is at best the mineralogy at the cessation of garnet growth and at worst represents the changes in mineralogy after garnet growth. There are differences between the observed and predicted mineralogy in the lawsonite (3.3 predicted, 0 observed) and epidote (0 predicted, 7 observed). Also the amphibole (0.1 predicted, 7.0 observed) and omphacite (79.5 predicted, 65.0 observed). That the hand sample does not contain any lawsonite means that the sample must have become hotter before exhumation and crossed the lawsonite-out line (Fig. 17). The pseudosection predicts that lawsonite is converted to zoisite at some points across this line. The epidote in the sample today could be the remaining evidence of this transition. Amphibole is texturally late, occurring as large needles, so the 7 volume % observed in the sample today could be the result of late breakdown of omphacite to amphibole upon rehydration. The Mg in amphibole (1.8 mol MgO per formula unit) isopleth does not intersect either the core or rim P-T location, but does exist at lower P-T in the matrix composition (Fig. 17). The models were run with different amounts of carbon dioxide in the fluid; 0.05 mol % for the core and 0.1 mol % for the rim. The amount of carbon dioxide in each model run was determined empirically by trying several concentrations and using the one that best reproduced garnet isopleths and modal mineralogy. That carbon dioxide concentrations in fluid are predicted to change during garnet growth is interesting and suggests a potential explanation for a feature of the garnet major element zonation. There is a distinct resorption texture at about 50 volume percent across the garnet. This area of garnet resorption could have been caused by a temporary period of increased carbon dioxide concentration in fluid. Models of this sample show that when carbon dioxide concentrations are high, the onset of garnet

stability is pushed to hotter temperatures as Mn carbonate is stabilized over a greater P-T space (Fig. 5). The garnet-in line from a model run at 1 % carbon dioxide is traced on the matrix pseudosection (Fig. 17). Potentially, garnet growth initiated at 0.05 percent carbon dioxide in the fluid, garnet breakdown occurred when the system was temporarily infiltrated by fluid with a higher carbon dioxide concentration, and then garnet growth resumed as carbon dioxide concentration in the fluid subsided, not far in P-T space from where it had started. Fluid composition could vary locally but as a point of reference, Schumacher et al (2008) determined that CO₂ in fluid in equilibrium with glaucophane-bearing marbles did not reach above 3% which is greater than the 1% CO₂ in fluid needed to push garnet growth to higher temperatures.

Predicted mineralogy at 75% of garnet growth for sample 14BSY-35D is 35.1 volume % mica, 9.7% garnet, 9.5% amphibole, 9.7% lawsonite, and 5.1% quartz (Table 7). Two immiscible clinopyroxenes are predicted at the rim location: 26.2 volume % of a more omphacitic (higher relative Ca and Mg) composition and 4.6 % of a more aegiritic version (higher relative Fe³⁺ and Na). It is difficult to compare the predicted mineralogy to the mineralogy in the sample today because the predicted mineralogy is for only 75% of garnet growth. The most striking differences between the predicted and observed mineralogy is the amount of clinopyroxene (54.0 % observed, 30.8 % predicted), the amount of amphibole (1.0 % observed, 9.7% predicted) and the amount of lawsonite (0.0 % observed, 9.7% predicted). Amphibole and clinopyroxene volume percent isopleths are very tightly spaced at this point in P-T space; a relatively minor increase in temperature quickly decreases the amount of amphibole and increases the amount of omphacite. The lack of lawsonite observed in the rock means that the sample must have crossed the

lawsonite-out line by increasing temperature or decreasing pressure (Fig. 16). The matrix pseudosection shows that when this occurs the assemblage becomes largely what is seen in the rock today; mica + garnet + clinopyroxene + quartz. The Si in mica isopleth (3.44 moles SiO per formula unit) intersects well with the core P-T conditions (Fig. 16).

14BSY-38A was unable to be modeled successfully with the method applied to the other samples. The rock shows extensive evidence for open system behavior. First, the inverse Mn zonation in garnet occurs as steps, as if new Mn was introduced to the system in pulses (Fig. 7). Second, concentration ratios of K/Ti and Na/Ti increase from core to rim; that these mobile elements increase relative to Ti is suggestive of external fluid added to the system (Fig. 14). The physical setting of the sample as a small boudin, about ~ 30 cm by ~10 cm in a much larger volume of quartz mica glaucophane schist (Fig. 18) presents a conundrum. On one hand, the small boudin is surrounded by calcite mineralization suggesting the lithologic contact between the eclogite boudin and the schist provide a conduit for large-scale fluid flow similar to what is described by Breeding et al. (2003). On the other hand, the boudin preserved its mineralogy distinct from the surrounding rock and appears to lack a diffusive boundary, suggesting that whatever fluid flow it experienced didn't alter its composition very much or allow chemical communication with the surrounding rock.

One thing we can assert is that neither the rim nor the core garnet isopleths are present in the modeled P-T space, despite the overall mineral assemblage (mica-calcite-garnet-clinopyroxene-titanite) being generally reproduced, with the exception of minor amounts of epidote and feldspar which are presumed to be late (Fig. 18). One problem seems to be that if the bulk XRF composition is used, the model simply will not grow

garnet with the low mole fraction spessartine seen in the core of the garnets (Fig. 7). This alone suggests that Mn has been added to the system. A second problem is that the model drastically over-predicts the mole fraction grossular at the expense of the mole fraction almandine. Attempts to systematically remove MnO, CaO, and both together from the whole rock to try to re-create the composition of the system at core growth are similarly unsuccessful. It may be that if Ca and Mn were being transported by an external fluid, so too were other elements, making it difficult to know which to remove to try to create the composition at core growth. Unfortunately, the composition today is unable to model rim growth, with or without removing garnet from the bulk composition. This suggests that the open system behavior that grew garnet didn't end when garnet growth ended. As removal of CaO and MnO was not successful, the composition of the surrounding quartz mica glaucophane schist, sample 14BYS-38B was substituted to model garnet growth. This composition gives good garnet rim isopleth intersections and the core isopleths are lacking only Mn (which, as previously discussed, is very low) (Fig. 18). A hybrid lithology, mixing 14BSY-38B and 14BSY-38A at a 90 to 10 ratio respectively, was created to investigate whether there was some kind of slight initial chemical difference between the present-day eclogite and surrounding schist. This hybrid lithology shows even better core isopleth intersections and the same mix with garnet removed from the 14BSY-38A composition creates an excellent rim isopleth intersection.

These models are far from conclusive yet are certainly interesting. The obvious field interpretation of the relationship between the eclogite boudin and the surrounding schist is that the eclogite represented some kind of initial heterogeneity in the protolith which generated a mineralogical and then rheological difference between the two rocks.

An alternative idea suggested by this modeling is that both the boudin and the surrounding schist reached HP-LT conditions with very little chemical differences. Then, as garnet started to grow in a very Mn and Ca-poor rock, external fluid entered the system and was channelized along the future eclogite, maybe because of difference in porosity. This pulse of fluid spurred garnet and omphacite growth and as these minerals grew in the presence of an exotic fluid they took elements from this fluid. Even after the fluid left the system, the rock left behind had a different composition from the surrounding rock that had formerly been its chemical twin. This system may have initially had a diffusional contact but once the chemical difference had been established a rheological difference now existed. Subsequent deformation meant that the eclogitized region was stretched and sheared and eventually boudinaged such that the original contact between it and the surrounding schist was obscured. Channelized fluid flow causing local chemical changes is widely documented in subduction zones (Bebout and Barton, 1989), (Marschall et al., 2006). Spandler et al. (2011) described eclogite facies veins in the Monviso ophiolite 5-10 cm thick and 0.5 to 1 m long with sharp contacts with surrounding rock. Of course, these veins were morphologically decidedly veins – they had branching structures and cross cut foliation - unlike the boudinaged eclogite blob that is 14BSY-38A. If this sample is deemed of further interest, a first step would be to date and chemically analyze the small garnets in the surrounding schist to see how the age and chemistry compares to those in 14BSY-38B. At the moment, the interpretation for this sample is unclear so the P-T conditions of growth will not be discussed alongside the three successfully modeled samples.

6.4 REGIONAL IMPLICATIONS OF THERMODYNAMIC MODELING

The three successfully modeled eclogites show fairly similar core to rim P-T paths (Fig. 23). This is despite the fact that the three samples record a range in ages of almost 9 myr, and that eclogite does not generally occur as large continuous units on Syros but is instead present as discontinuous blobs in more voluminous schists. It is difficult to use the P-T paths calculated in this study to inform the difference between the three locations where garnet geochronology was conducted because only two of the locations (Katergaki and Kini) have rocks that were modeled. However, sample 06MSY-6E from the Kini location shows garnet growth at 50 MPa less pressure and 30 K lower temperature than the start of garnet growth in 14BSY-37A from the Katergaki location and 70 MPa less pressure and 50 K lower than 14BSY-35D also from Katergaki. Perhaps, in addition to different tectonic settings (one within an ultramafic *mélange*, the other away the *mélange* interface), the three locations modeled yield different ages because the composition of the rocks at Kini suggests that they start growing garnet sooner.

The P-T paths for the three modeled rocks show samples beginning garnet growth along a similar P-T path but then achieving different maximum pressure (Fig. 23). Unfortunately, because only one sample showed garnet growth along an exhumation path, it is not known if the three samples followed similar exhumation paths which would have allowed testing of the Trotet et al. (2001b) tectonic model. The P-T path for sample 14BSY-37A is different from the other two modeled rocks. This sample is from Katergaki where 14BSY-35D was also found but 14BSY-35D follows a path that looks much more like 06MSY-6E from Kini in that it reaches the same very high pressures (around 2.4 GPa). Sample 14BYS-35D, was also the oldest garnet age from Katergaki

(48.1 ± 2.3 Ma). The two higher-pressure rocks show older garnet growth ages than the lower pressure rock. This suggests that higher-pressure samples were buried earlier and stayed at depth longer to be exhumed at the same time as the lower pressure rocks.

These differences add some nuance to the idea that the Kini and Grizzas regions experienced earlier subduction *mélange* metamorphism while Katergaki experienced garnet growth later and slightly removed from the ultramafic *mélange*. The eclogites modeled from Katergaki were both found as float. The in-place sample that was unable to be modeled was found as a small boudin. It seems like these small eclogite pods or boudins at Katergaki record different P-T histories from one another yet ended up entrained in the same unit, perhaps late in the exhumation process. A P-T path for sample 14BSY-38A, which is from Katergaki, was found in outcrop, and has a young age, would allow more clarity on this situation but, unfortunately, that sample was unable to be modeled.

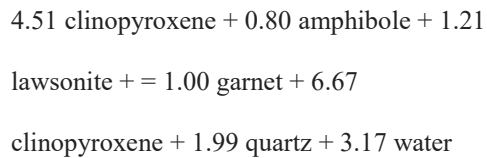
The pressure-temperature paths modeled here are all notably deeper but comparable in temperature to the garnet growth paths modeled by Dragovic et al. (2012) on Sifnos (Fig. 23). In fact, the pressure temperature paths here are markedly higher than most other pressure estimates for Syros. The lowest P-T estimates for peak metamorphism come from Putlitz et al. (2005) who placed maximum conditions for a phengite-bearing eclogite at 1.4 GPa and 550 °C (832 K) based on thermodynamic modeling which predicted kyanite above 1.4 GPa when none was observed in their sample. Schumacher et al. (2008) placed the maximum pressure and temperature experienced by marbles on Syros at 1.6 GPa and 480 °C (753 K) based on the modeled stability of aragonite and glaucophane. However, some authors have predicted deeper

paths; Trotet et al. (2001b) used TWEEQ (Berman, 1991) to calculate the intersection of 39 reaction lines for 10 end-members in an eclogite to determine that Syros and Sifnos reached the same maximum pressure at 1.9 GPa while Syros was slightly cooler (525 °C/798 K to Sifnos' 580 °C/853 K). Schmadicke and Will (2003) calculated the maximum pressure and temperature conditions for blueschists from Sifnos to be 2.0 GPa and 550-600 °C (823-873 K) using the garnet-clinopyroxene thermometer (from Ellis and Green 1979), the garnet phengite thermometer (Green and Hellman 1982), and the phengite barometer (Massonne and Schreyer 1989). Philippon et al. (2013) modeled lawsonite bearing blueschists on Syros and calculated maximum pressure temperature conditions of 2.0 GPa and 550 °C (823 K). Okrush and Bröcker (1990) placed a maximum of 2.0 GPa on eclogites from Syros and Sifnos based on the location of the kyanite-in line. The P-T paths calculated for this study are significantly deeper than any of these previous estimates. The only calculations that align with these data are those of Holley et al., (2004) and Gitahi (2004) who used the geothermobarometer of Ravna and Terry (2004) on eclogite facies knockers from Syros, obtaining conditions of 1.9-2.4 GPa and 500-580 °C (773-853 K). It is entirely possible that the pressures calculated in this study are erroneous for one reason or another but the fact that most previous studies finding lower pressures have not focused exclusively on eclogites, and that early work on the Ravna and Terry geothermobarometer seems to support these pressures for at least mafic and ultramafic knockers, is encouraging. Alternative thermobarometers such as the REE-in-garnet-clinopyroxene method developed by Sun and Liang (2015) could prove useful in resolving the pressure-temperature path discrepancies.

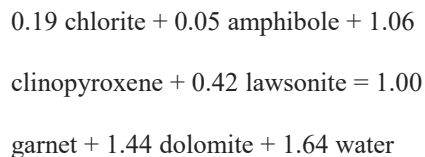
Schumacher et al. (2008) suggests a tectonic interpretation to reconcile the different pressure temperature predictions for mafic and ultramafic rocks from Holley et al. (2004) and Gitahi (2004) as compared to lower pressures calculated for marbles. They reason that all rocks on Syros from the marble and schist units to the ultramafic mélange experienced the same episode of deformation; thus, for a while their P-T paths had to be the same. However, they suggest that perhaps the mafic and ultramafic rocks were metamorphosed earlier and deeper and then got attached to the upper plate and began to be exhumed. The marbles and schists, meanwhile, began to be subducted and then got scraped off the down-going slab at ~1.5 GPa and caught up with the ultramafic and mafic material on its exhumation path. This scenario sets up the testable hypothesis that marbles and schists should have younger ages than the mafic and ultramafic material. If the tectonic interpretation discussed above is accepted, then this study combined with data from Lagos et al. (2007) does in fact see older ages for eclogites from the ultramafic mélange and younger ages for eclogites from an area with more marble. However, even the young eclogites modeled here (43.6 ± 1.6 Ma) show high pressures. Anything younger than ~40 Ma is usually attributed to the greenschist facies overprint (i.e. Bröcker et al. 2013).

All modeled samples released water during garnet growth. Lawsonite is capable of holding 2 moles of water per formula unit (~14 weight %) The most striking observation from the water loss predictions is how much more water was able to be held and then lost during garnet growth in sample 06MSY-6E than in either of the other two successfully-modeled samples (Table 6). 14BSY-37A and 14BSY-35D could have continued to release water during garnet growth that is not recorded here because neither

was modeled to the completion of garnet growth. The amount of water each would have lost would depend strongly on the exhumation path taken; sample 06MSY-6E loses so much water in part because it continues to heat upon decompression and so crosses the lawsonite-out line. However, 06MSY-6E held more water initially than either of the other two samples. Water loss during garnet growth for 14BSY-35D from the core to the 75 volume percent garnet modeled rim is represented in the following net reaction normalized to one mole of garnet:



Water loss during 90 volume percent garnet growth for 14BSY-37A is similarly expressed:



While water in 14BSY-35D and 14BSY-37A was bound dominantly in lawsonite, 06MSY-6E held water in lawsonite and also in chlorite. Below is the net reaction for water loss during garnet growth normalized to one mole of garnet:

0.48 chlorite + 0.61 lawsonite + 0.26

clinopyroxene = 1.00 garnet + 0.12

amphibole +3.03 water

Chlorite stability in 06MSY-6E is assumed to be enhanced by the very high iron content of the sample (~22 weight % Fe_{tot} as measured by XRF, see Table 1). Chlorite has been recognized as an important phase for carrying water in subduction zones in ultramafic rocks (VanKecken et al., 2011). Water release from all the samples modeled here was greater than modeling results for a blueschist and a quartz mica schist from Sifnos. The difference between 14BSY-37A and 14BSY-35D and the Sifnos samples lies not in the ability of the rock to hold water, but in the amount of water released during garnet growth. The eclogite samples modeled here came closer to the lawsonite-out line in P-T space and thus lost more water from lawsonite breakdown. A combination of P-T path and chemical composition determines how much water is released during garnet growth.

7.0 CONCLUSIONS

- This study proves that dating eclogites with $^{147}\text{Sm}/^{144}\text{Nd}$ garnet geochronology is not only possible but capable of providing high precision ages (± 1.0 Ma). However, additional work is needed to determine why certain samples cannot be sufficiently cleaned of inclusions for optimal $^{147}\text{Sm}/^{144}\text{Nd}$ garnet geochronology. Such research would aid in identification of promising samples for future work.
- Successfully dated garnets show, on average, younger ages than previously published garnet ages (using $^{176}\text{Lu}/^{176}\text{Hf}$) on the island, suggesting that HP-LT metamorphism event in Syros lasted at least 8.6 ± 1.6 million years.
- $^{147}\text{Sm}/^{144}\text{Nd}$ garnet ages from eclogites do not all overlap within error meaning that discrete packages of rock were metamorphosed to eclogite facies at different times.
- Successfully modeled eclogite samples showed similar garnet growth P-T paths to one another, despite differing mineralogy, bulk chemistry, garnet chemistry, sample location, and garnet growth ages. This suggests that the subduction geotherm was well established for the duration of metamorphism.
- Peak pressures vary between samples, with the higher pressure samples showing older ages. Samples which reached higher pressure may have reached those

pressures earlier and then stayed at depth longer to be later exhumed with the younger, lower pressure rocks.

- Using nearly identical modeling techniques, the P-T paths for Syros are at a higher pressure than those reported on Sifnos. They are at a higher pressure by at least 500 MPa than any other estimate for rocks from Sifnos with the exception of studies using a garnet-clinopyroxene geothermobarometer. Further work is needed to investigate the differences between pressures determined in this study and the more widely accepted values.
- Similar P-T paths for garnet growth do not mean that modeled samples held or released similar amounts of structurally bound water during garnet growth. In contrast, water released by samples during garnet growth varies dramatically from 5.13 to 1.09 weight percent. This study suggests that the carrying capacity of water in ultramafic samples is higher than mafic samples due to greater chlorite stability.

8.0 TABLES

Table 1 Oxide weight percent data from XRF

sample	06MSY-6E	14RSY-8A	14BSY-35D	14BSY-37A	14BSY-38A	14BSY-38B
SiO ₂	41.56	45.22	52.93	51.28	53.10	77.27
TiO ₂	3.44	0.84	1.02	0.29	0.56	0.19
Al ₂ O ₃	15.73	14.72	19.03	13.13	13.16	11.92
MnO	0.36	0.11	0.14	0.30	0.19	0.08
MgO	4.73	4.82	3.48	5.09	5.58	0.53
CaO	7.66	13.33	5.94	12.28	11.85	2.38
Na ₂ O	3.17	3.96	3.75	5.61	6.77	4.74
K ₂ O	0.05	2.45	3.72	0.10	1.22	0.40
P ₂ O ₅	0.04	0.77	0.42	0.05	0.03	0.01
Fe ₂ O ₃ tot.	22.12	8.10	9.07	11.46	7.20	2.58
Fe ₂ O ₃ from titration	10.22	3.04	2.56	5.96	no data	no data
FeO if max Fe ₂ O ₃	10.71	4.55	5.86	4.95	no data	no data
max Fe ₂ O ₃ /Fetot	0.46	0.38	0.28	0.52	no data	no data
LOI	1.49	6.37	2.60	0.89	2.18	0.49
total (without LOI)	98.86	94.32	99.50	99.59	99.66	100.10

Next page:

Table 2 Microprobe analyses for all samples in oxide weight percent.

If a mineral is not listed here but is reported in the text and in Figure 2, that is because no microprobe data was obtained for that mineral in that particular rock. Garnet oxide weight percent reported here is a volumetric average of microprobe spot analyses from rim to rim across up to two garnet crystals. The number of analyses included in a garnet average range from 42– 246 individual microprobe analyses, depending on the size of the garnet. An asterisk (*) after a mineral name indicates that the reported oxide weight percent data is from a single analysis. All other reported data (except garnet) is an average of from 2 to 15 microprobe spot analyses. Details of microprobe parameters in text. (mtx) = mineral in the matrix; (in gt) = mineral analyzed was an inclusion in garnet

Table 2 Microprobe analyses for all samples in oxide weight percent.

06MSY-6E	SiO₂	TiO₂	Al₂O₃	MgO	CaO	MnO	FeO	Fe₂O₃	Na₂O	K₂O	Total
garnet	37.13	0.12	21.57	2.56	8.19	0.36	29.31	0.00	0.04	0.00	99.27
mica*	51.70	0.25	29.26	3.28	0.03	0.04	3.59	0.00	0.26	10.50	98.91
omphacite	54.83	0.06	9.63	7.58	12.12	0.02	6.42	0.16	7.17	0.01	97.99
amphibole	55.59	0.04	10.26	10.75	1.52	0.05	9.86	0.00	6.64	0.04	94.75
epidote	38.01	0.09	24.69	0.00	23.54	0.34	0.00	12.99	0.02	0.01	99.68
chlorite (mtx)	25.04	0.03	19.48	12.68	0.03	0.38	24.90	0.90	0.05	0.00	83.48
chlorite (in gt)	22.81	0.04	20.01	3.39	0.06	1.31	41.95	0.00	0.03	0.00	89.60
rutile	0.02	92.24	0.00	0.00	0.09	0.01	0.62	0.05	0.03	0.01	93.07
14RSY-8A	SiO₂	TiO₂	Al₂O₃	MgO	CaO	MnO	FeO	Fe₂O₃	Na₂O	K₂O	Total
garnet	39.25	0.06	21.81	2.09	10.51	0.73	28.28	0.00	0.05	0.01	102.80
mica	50.59	0.23	26.58	3.75	0.03	0.01	2.40	0.00	0.47	10.58	94.64
omphacite	56.58	0.04	11.53	6.62	12.23	0.03	5.50	1.17	7.48	0.02	101.20
amphibole (mtx)	58.03	0.00	12.22	9.79	0.77	0.03	10.61	0.00	6.99	0.03	98.48
amphibole (in gt)	56.28	0.04	11.50	6.63	0.80	0.13	16.91	0.00	6.79	0.02	99.09
epidote	38.88	0.12	28.21	0.04	23.75	0.04	0.00	7.74	0.00	0.00	98.79
titanite	31.08	35.32	3.52	0.02	29.25	0.02	0.38	0.00	0.06	0.01	99.67
calcite in vein	0.04	0.01	0.02	0.67	64.79	0.03	0.14	0.00	0.04	0.02	65.77
14BSY-35D	SiO₂	TiO₂	Al₂O₃	MgO	CaO	MnO	FeO	Fe₂O₃	Na₂O	K₂O	Total
garnet	36.72	0.08	21.28	1.58	8.81	0.74	29.95	0.00	0.03	0.01	99.21
mica	52.16	0.23	27.18	2.80	0.01	0.01	2.70	0.00	0.47	10.87	96.43
omphacite	56.48	0.05	12.49	5.24	10.08	0.07	4.27	4.00	9.14	0.01	101.83
amphibole	58.68	0.01	11.47	9.15	0.28	0.07	11.54	0.56	7.19	0.01	98.96
epidote	37.77	0.08	26.51	0.00	23.52	0.13	0.00	9.83	0.01	0.01	97.86
titanite	31.14	36.64	2.50	0.00	28.71	0.03	0.34	0.00	0.05	0.11	99.53
quartz	98.32	0.01	0.00	0.00	0.01	0.00	0.09	0.00	0.01	0.00	98.45
14BSY-37A	SiO₂	TiO₂	Al₂O₃	MgO	CaO	MnO	FeO	Fe₂O₃	Na₂O	K₂O	Total
garnet	37.46	0.08	21.18	1.72	9.72	1.69	28.09	0.00	0.03	0.02	99.98
omphacite 1	55.99	0.06	9.85	5.17	11.67	0.11	7.75	4.06	7.55	0.01	102.22
omphacite 2	57.06	0.04	11.49	7.17	12.32	0.02	5.20	1.35	7.51	0.00	102.15
omphacite (in gt)	56.79	0.04	10.10	6.37	12.57	0.00	5.51	3.59	7.53	0.01	102.51
amphibole	59.08	0.01	11.24	8.83	0.34	0.02	12.83	0.61	7.07	0.00	100.03
epidote	39.53	0.08	28.15	0.02	24.23	0.04	0.00	8.96	0.02	0.00	101.04
quartz	99.63	0.00	0.02	0.00	0.04	0.00	0.28	0.00	0.01	0.01	100.00
14BSY-38A	SiO₂	TiO₂	Al₂O₃	MgO	CaO	MnO	FeO	Fe₂O₃	Na₂O	K₂O	Total
garnet	38.20	0.05	22.16	1.64	11.89	4.01	23.68	0.58	0.03	0.01	102.26
mica	54.23	0.22	28.61	3.71	0.04	0.02	0.00	2.48	0.52	10.66	100.50
omphacite	57.69	0.07	10.86	6.32	11.74	0.09	4.70	3.54	7.97	0.00	102.97
feldspar	50.08	0.03	41.60	0.22	0.20	0.02	0.43	0.00	7.07	0.94	100.58
epidote*	39.03	0.11	25.26	0.00	23.38	0.46	0.00	12.37	0.00	0.02	100.63
titanite	31.53	36.82	2.53	0.00	29.01	0.03	0.25	0.00	0.02	0.00	100.19
carbonate	0.03	0.01	0.04	0.00	57.06	0.00	0.09	0.00	0.00	0.03	57.27

Table 3: Isotope data from TIMS analysis

	147Sm/14 4Nd	143Nd/14 4Nd	147Sm/144 Nd error	143Nd/144 Nd error	ng Nd	ng Sm	ppm Nd	ppm Sm	minutes in HF	mg garnet to start	percent loss during partial	mesh size fraction	
06MSY-6E	gt1	0.277013	0.513035	8.547E-06	8.671E-06	35.51	16.26	2.39	1.09	47	67.7	55	140-230
	gt2	0.255789	0.513027	6.344E-06	5.689E-06	48.93	20.69	2.76	1.17	62	93.8	60	140-230
	gt3	0.345952	0.513062	2.394E-05	1.046E-05	27.04	15.47	1.50	0.86	92	132.9	71	140-230
	gt4	0.364820	0.513063	1.394E-05	6.879E-06	19.26	11.61	1.27	0.77	130	140	89	140-230
	gt5	0.362042	0.513075	3.756E-05	9.814E-06	4.44	0.00	1.42	0.85	110	50.5	93	140-230
	gt6	0.320582	0.513057	4.124E-05	1.182E-05	5.26	2.79	1.76	0.93	120	97.7	96	140-230
	gt7	0.373877	0.513069	5.994E-05	1.441E-05	2.98	1.84	1.99	1.23	154	91.2	98	140-230
	gt8	0.402718	0.513096	3.622E-05	8.610E-06	4.92	3.28	1.23	0.82	95 + 60	49.98	92	140-230
	gt 8 leachate	0.337814	0.513059	1.653E-05	7.897E-06	10.05	5.61	-	-	-	-	-	140-230
	WR AQ1	0.178288	0.513005	1.459E-05	5.510E-06	9.10	2.68	18.57	5.47	-	-	-	<100
14BSY-8A	gt1 (excl.)	0.206618	0.512640	2.473E-05	5.607E-06	35.75	12.20	1.71	0.59	120	78	73	100-200
	gt3	0.432744	0.512706	5.667E-05	5.140E-06	17.99	12.87	0.56	0.40	180	168	81	100-200
	gt4 (excl.)	0.315374	0.512654	4.119E-05	2.100E-05	2.70	1.41	0.62	0.32	120	100.9	96	140-230
	gt5 (excl.)	0.670533	0.512736	8.467E-04	3.355E-05	0.60	0.66	0.33	0.37	180	137.3	99	140-230
	gt6	0.492033	0.512715	3.624E-04	1.695E-05	3.07	2.50	0.41	0.33	120	87	91	140-230
	gt7 (excl.)	0.356733	0.512661	5.719E-03	2.929E-04	0.24	0.14	0.45	0.27	180	104.3	99.5	140-230
	gt8	0.458797	0.512710	5.551E-05	8.774E-06	3.29	2.50	0.47	0.35	120	87.7	91	140-230
	gt9	0.411274	0.512691	2.897E-05	7.095E-06	6.02	4.10	0.70	0.48	87	29	70	140-230
	WR XRF AQ1	0.095212	0.512593	7.474E-06	4.766E-06	16.22	2.55	48.84	7.69	-	-	-	-
	WR AQ1	0.091552	0.512593	1.071E-05	4.339E-06	43.42	6.57	53.20	8.05	-	-	-	-
WR AQ2 (excl.)	0.136968	0.512579	2.334E-05	3.029E-05	10.23	2.32	52.53	11.90	-	-	-	-	
WR AQ3 (excl.)	0.079066	0.512603	2.285E-04	1.154E-05	17.07	2.23	53.07	6.94	-	-	-	-	
	“(excl.)” indicates an analysis was excluded from the isochron												

Table 3 cont.

	147Sm/144Nd	143Nd/144Nd	147Sm/144Nd error	143Nd/144Nd error	ng Nd	ng Sm	ppm Nd	ppm Sm	minutes in HF	mg garnet to start	percent loss during partial	mesh size fraction	
14BSY-37A	gt1	0.763102	0.512550	8.376E-05	7.155E-06	7.45	9.39	0.34	120	61.3	65	100-200	
	gt3	1.114857	0.512662	2.224E-04	1.210E-05	3.12	5.74	0.19	180	148	89	100-200	
	gt4	1.016684	0.512610	1.210E-04	1.275E-05	5.61	9.43	0.25	120	95.2	76	140-230	
	gt5 (excl.)	0.839135	0.512617	1.153E-03	2.083E-04	0.43	0.59	0.16	150	100.2	97	140-230	
	gt6 (excl.)	0.831397	0.512573	2.579E-04	6.456E-05	0.51	0.69	0.17	180	135.1	98	140-230	
	gt7	1.390799	0.512730	1.289E-04	1.763E-05	2.91	6.68	0.16	120	120	85	140-230	
	gt8	1.371591	0.512719	1.168E-04	1.951E-05	1.89	4.28	0.14	150	140	90	140-230	
	WR AQ1	0.142527	0.512367	2.035E-05	7.087E-06	11.94	2.81	14.54	3.43	-	-	-	-
	WR2 AQ1	0.139348	0.512373	5.188E-04	5.891E-06	9.92	1.55	15.17	3.49	-	-	-	-
	WR AQ2	0.094449	0.512369	6.316E-06	1.185E-05	7.18	1.65	14.41	2.25	-	-	-	-
14BSY-38A	gt1	3.932808	0.513799	1.392E-03	7.504E-05	0.89	5.75	0.05	120	96	83	140-230	
	gt2	3.363788	0.513645	4.059E-04	2.619E-05	2.14	11.87	0.07	90	86.8	65	140-230	
	gt3	1.281442	0.513033	9.025E-05	1.045E-05	12.05	25.53	0.19	30	97.7	33	140-230	
	gt4	2.433768	0.513359	5.305E-04	1.672E-05	4.86	19.56	0.09	63	104.2	50	140-230	
	gt5	1.616862	0.513141	6.160E-05	7.103E-06	8.14	21.76	0.14	45	100.4	43	140-230	
	WR AQ1	0.172143	0.512709	4.335E-05	1.167E-05	3.28	0.93	5.05	1.44	-	-	-	

“(excl.)” indicates an analysis was excluded from the isochron

Table 4: Garnet ages

Sample	isochron components	Age (Ma)	2 σ uncertainty	MSWD
06MSY-6E	1 wr+ 8 gts + 1 leacheate	57.7	6.3	1.9
14RSY-8A	2 wr+ 4 gts	48.8	3.2	0.67
14BSY-35D	1 wr + 3 gts	48.1	2.3	2.4
14BSY-37A	1 wr + 5 gts	43.6	1.6	2
14BSY-38A	1 wr + 5 gts	44.7	1	1.4
14BSY-35D core	1 wr + 1 pwd + 1 gt	66	15	1.4
14BSY-35D rim	1 mtx + 1 pwd + 2 gts	47.1	3	1.4

sample	06MSY-6E			14BSY-35D		14BSY-37A		14BSY-38A		14BSY-38B		
	WR	Wr (-86% gt)	Matrix (-100%gt)	WR	Matrix (-75%gt)	WR	Matrix (-90%gt)	WR	Matrix (-99%gt)	WR	hybrid with 38A WR	hybrid with 38A matrix
SiO ₂	42.93	47.02	48.19	53.87	55.60	52.33	54.13	53.65	54.46	77.38	75.01	75.09
TiO ₂	3.55	5.69	6.33	1.04	1.13	0.30	0.34	0.57	0.59	0.19	0.23	0.23
Al ₂ O ₃	16.25	13.03	12.03	19.37	19.16	13.40	12.21	13.30	12.88	11.94	12.07	12.03
MnO	0.37	0.21	0.18	0.14	0.08	0.31	0.01	0.19	0.01	0.08	0.09	0.07
MgO	4.89	6.92	7.28	3.54	3.75	5.19	6.02	5.64	5.84	0.53	1.04	1.06
CaO	7.91	7.21	7.13	6.05	5.82	12.53	13.35	11.97	11.99	2.38	3.34	3.34
FeO	18.70	11.14	9.05	7.58	5.44	9.08	5.73	5.96	5.08	2.10	2.49	2.40
Fe ₂ O ₃ tot.	2.07	3.37	3.77	0.80	0.64	1.04	1.13	0.65	0.68	0.25	0.29	0.29
Na ₂ O	3.27	5.32	5.94	3.82	4.20	5.73	6.97	6.84	7.18	4.75	4.96	4.99
K ₂ O	0.05	0.08	0.09	3.79	4.17	0.10	0.12	1.23	1.29	0.40	0.48	0.49
total	100.00	99.99	100.00	100.00	99.99	100.00	100.00	100.00	100.00	100.00	100.00	99.99
Fe ₂ O ₃ /Fetot	0.09	0.21	0.27	0.09	0.10	0.09	0.15	0.09	0.11	0.10	0.09	0.10
mol. % CO ₂	0.00	0.00	0.00	0.00	0.05	0.05	0.10	0.10	0.10	0.05	0.05	0.05

Table 5: Compositions used for thermodynamic modeling

Table 6: Water loss during garnet growth

sample		volume percent garnet	weight percent water	volume percent garnet adjusted	weight percent water adjusted	core to rim water loss*	LOI from XRF
06MSY-6E	core	4.67	5.50	0.00	5.84		
	middle	17.50	1.46	34.00	1.13		
	rim	9.35	1.14	40.00	0.71	5.13	1.49
14BSY-35D	core	2.11	3.81	0.00	3.92		
	rim'	2.43	2.98	10.00	1.32	2.60	2.60
14BSY-37A	core	5.52	1.37	0.00	1.47		
	rim'	0.23	0.45	13.50	0.38	1.09	0.89

*water loss core to *modeled* rim which for 14BSY-35D is 75% of garnet growth and for 14BSY-37A is 90% of garnet growth

Table 7 Comparison of modal mineralogy observed in samples to that predicted by modeling

		vol % observed in hand sample	vol % predicted by modeling
06MSY-6E	Chl	6.3	2.3
	Ilm	0.0	0.0
	Bio	0.0	0.5
	Mica	0.1	0.0
	Gt	40.0	45.6
	Amph	17.0	21.5
	Cpx	29.3	27.0
	ru	6.0	3.0
14BSY-35D	Mica	30.0	35.1
	Gt	10.0	9.7
	Amph	1.0	9.5
	Cpx	54.0	4.6
	Cpx		26.2
	law	0.0	9.7
	q	1.0	5.1
	ru	1.0	0.0
	Chl	1.0	0.0
	ep	1.0	0.0
14BSY-37A	Mica	0.0	1.0
	Do	0.5	3.2
	Gt	15.0	12.7
	Amph	7.0	0.1
	Cpx	65.0	79.5
	law	0.0	3.3
	ru	0.5	0.2
	ep	7.0	0.0

9.0 FIGURES

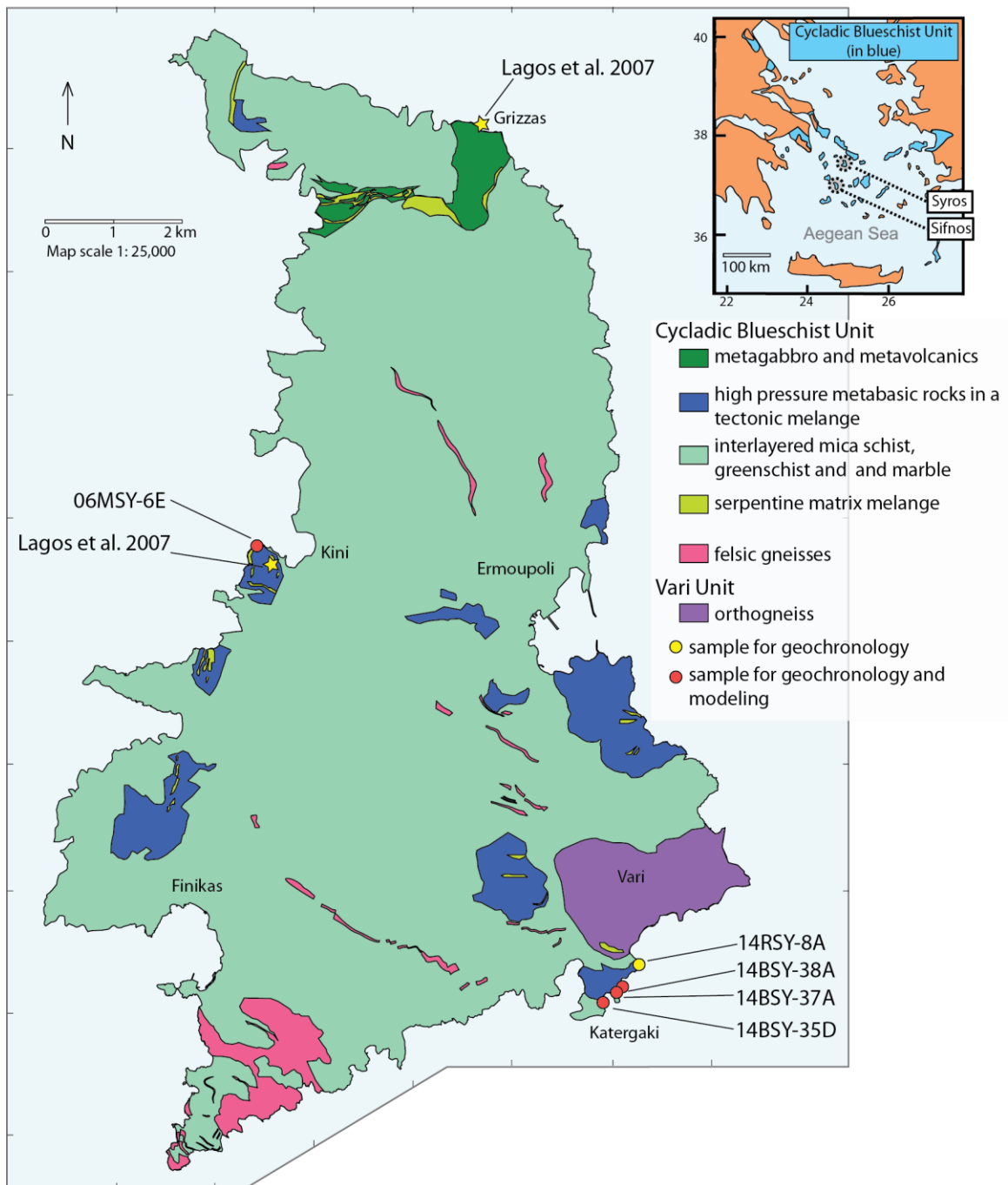


Figure 1 | Simplified geologic map of Syros Island in the Cyclades modified from Keiter et al. (2011). Sample locations for this study are shown with yellow and red circles. The locations of eclogite samples from Lagos et al. (2007) are shown with yellow stars. All samples are from the Cycladic Blueschist Unit. Syros Island is circled and labeled in the inset map, as is Sifnos Island. All samples in this study come from Syros but studies carried out on Sifnos are referenced in the text and the tectonic and metamorphic history of the two islands is often compared.

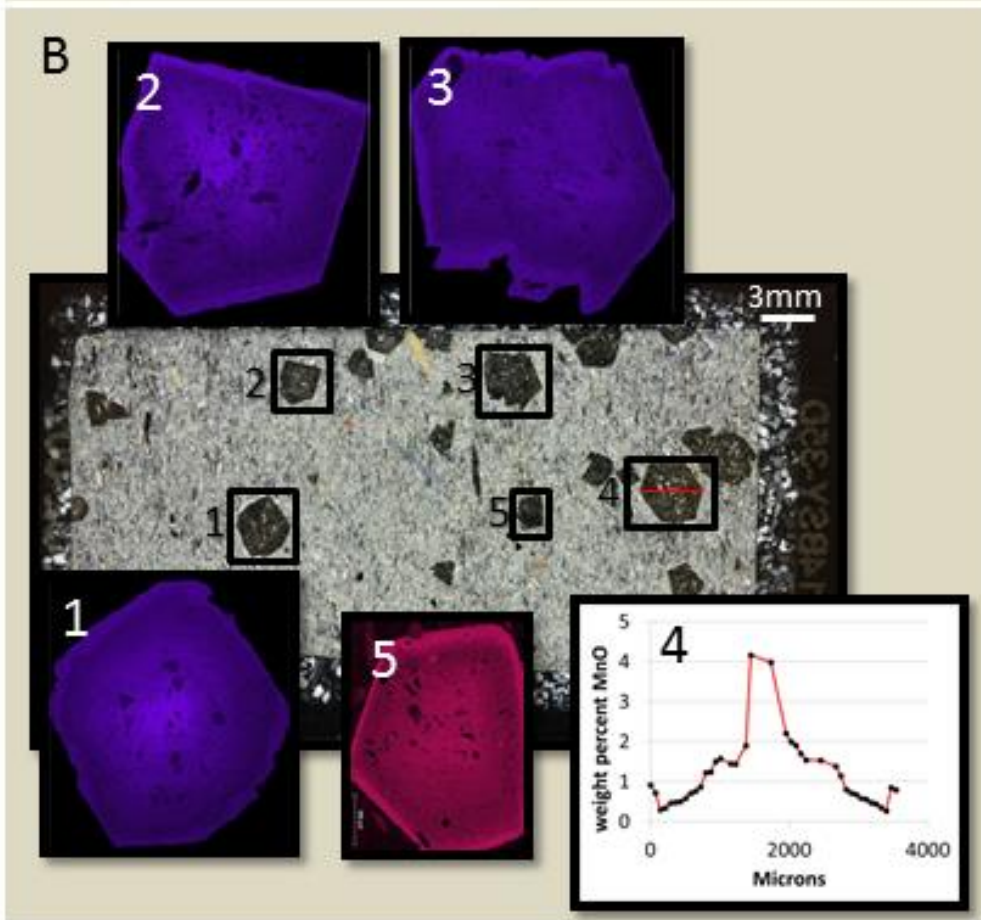
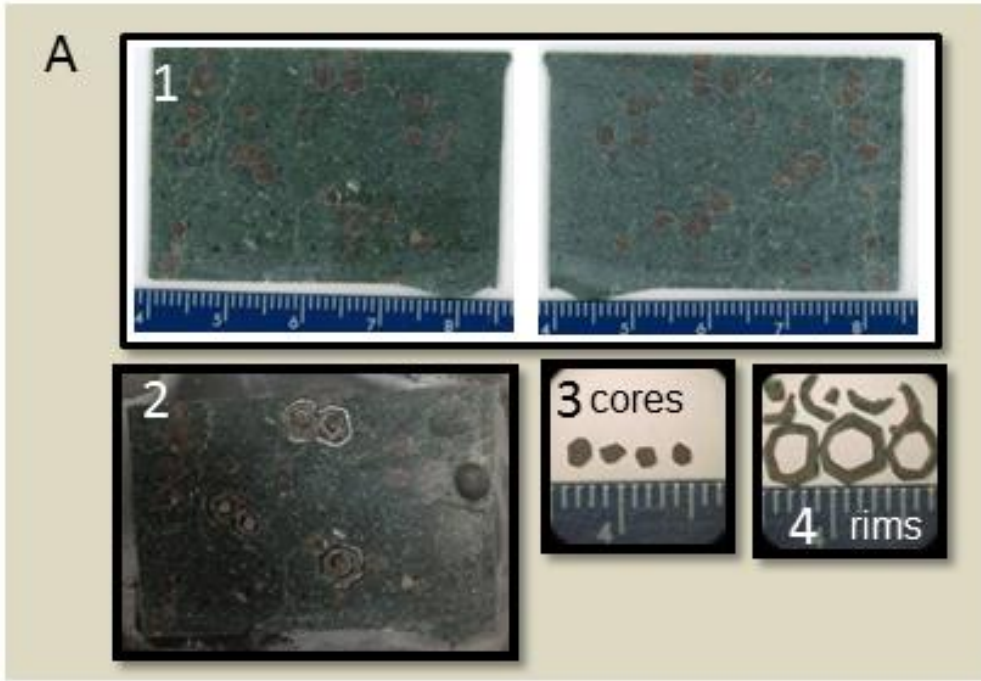


Figure 2 | A) Example of sample preparation for microdrilling for sample 14BSY-35D. 1) Front and back of 0.5 mm slice cut from whole rock. 2) Front of slice after drilling. Drill trenches around cores and rims are visible. 3) Cores after removal from drill setup. 4) Rims after removal from drill setup. Rims were drilled so that a layer of matrix was left around the edge of the garnet. 12 slices were cut, 39 garnets were microdrilled.

B) Photomicrograph of sample 14BSY-35D in crossed polarized light. Insets 1, 2, and 3 are maps of Mn concentration in garnet from an scanning electron microscope. Inset 4 is a MnO weight percent transect across a garnet from rim to rim from the microprobe. Inset 5 is a map of Mn concentration in garnet from the microprobe. The maps are qualitative but demonstrate that every garnet measured shows the same chemical pattern: high Mn in the core, which falls towards the rim and then increases again in what is interpreted as a resorption feature.

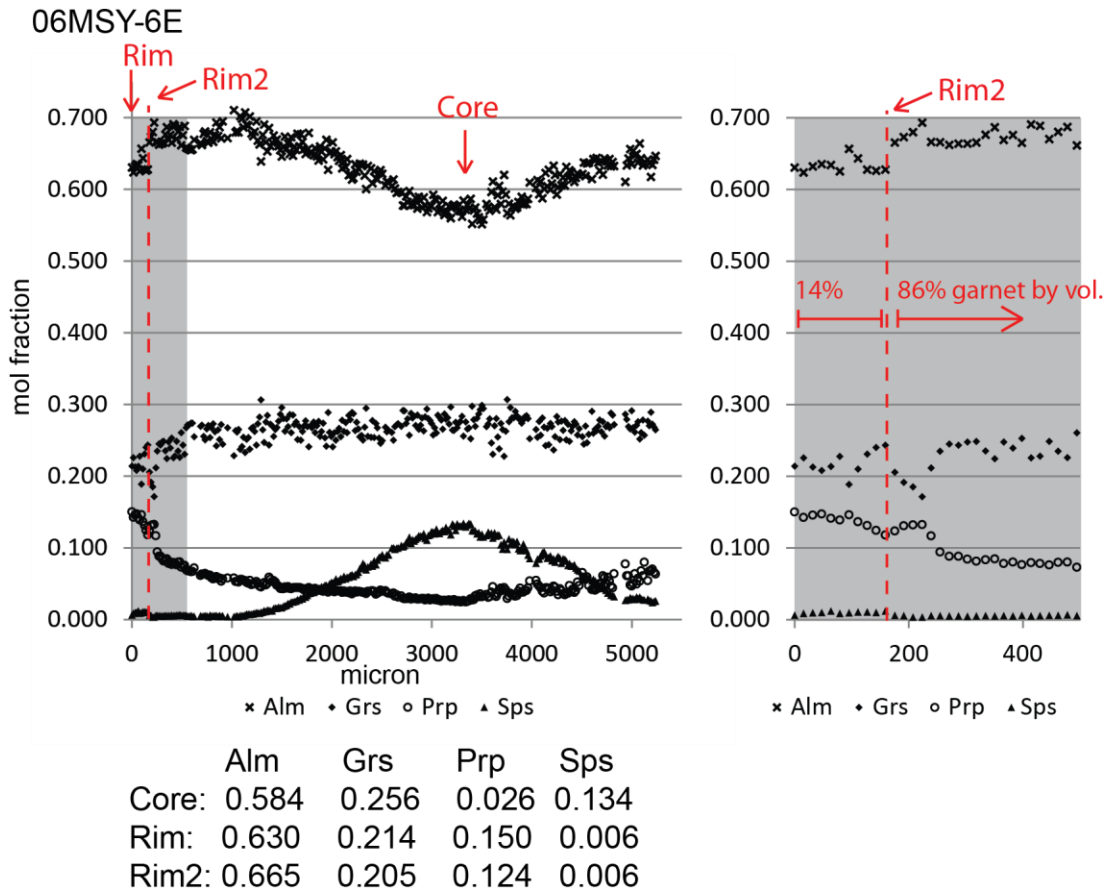


Figure 3 | Rim to rim garnet transect for sample 06MSY-6E. Garnet composition is calculated on the basis of 12 oxygen atoms from microprobe measured oxide weight %. The mole fraction of garnet end members at the core and rims are listed. These values are used to calculate isopleths, during thermodynamic modeling, to determine P-T conditions of core and rim growth. Gray area at left edge of graph is expanded to the right. What is labelled as Rim2 is visible in this expansion.

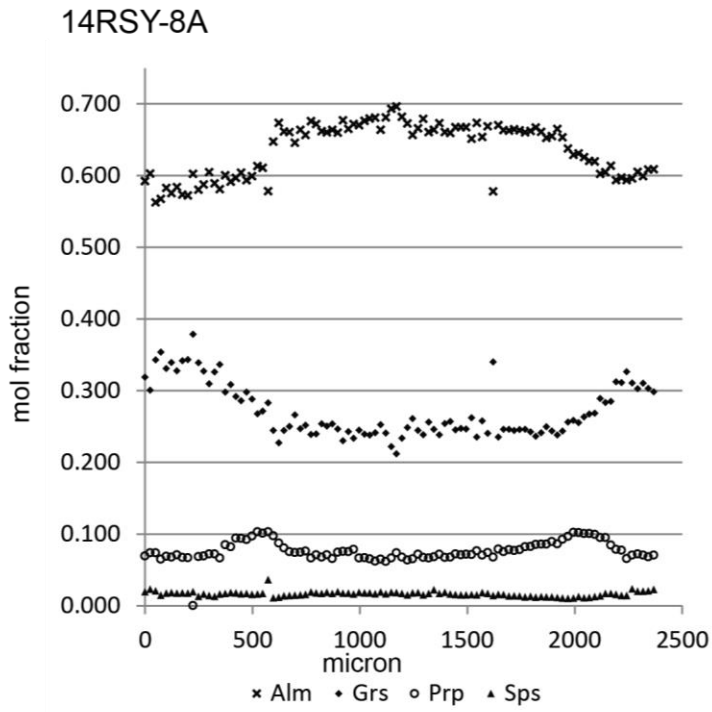


Figure 4 | Rim to rim garnet transect for sample 14RSY-8A. Core and rim values are not displayed as this sample was not used for thermodynamic modeling.

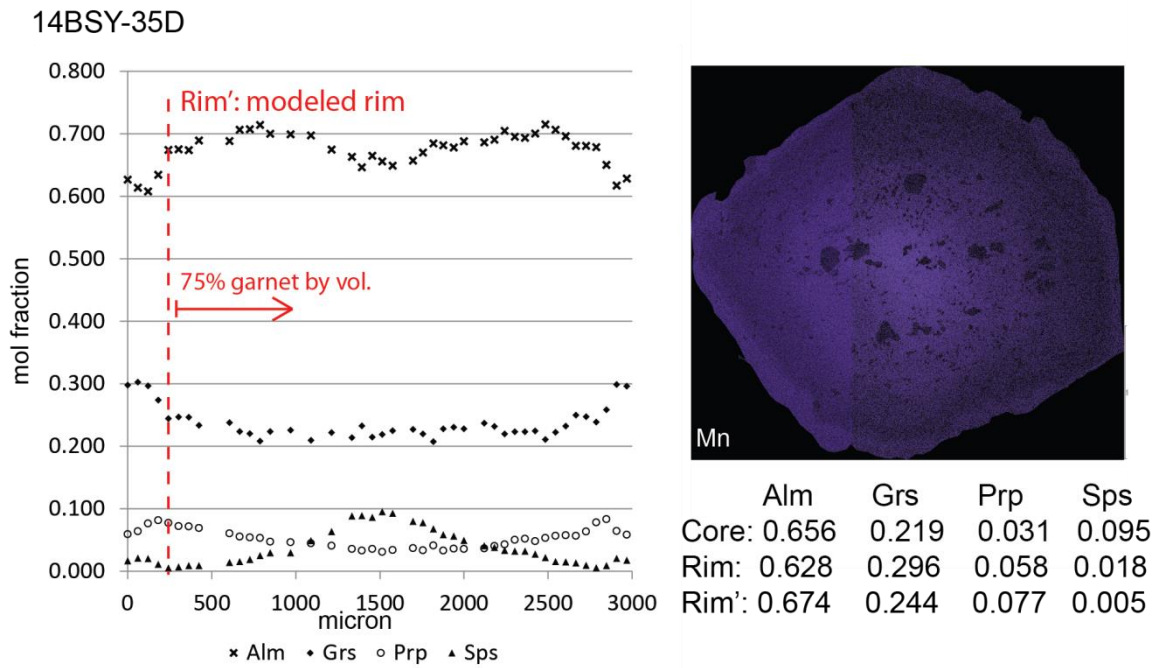


Figure 5 | Rim to rim garnet transect for sample 14BSY-35D. Manganese map of a different garnet from the same sample is shown to the right. The mole fraction of garnet end members at the core and rims are listed. Rim' is the point chosen to be just inside the resorption rim. Core and Rim' were used for thermodynamic modeling while the rim was not.

14BSY-37A

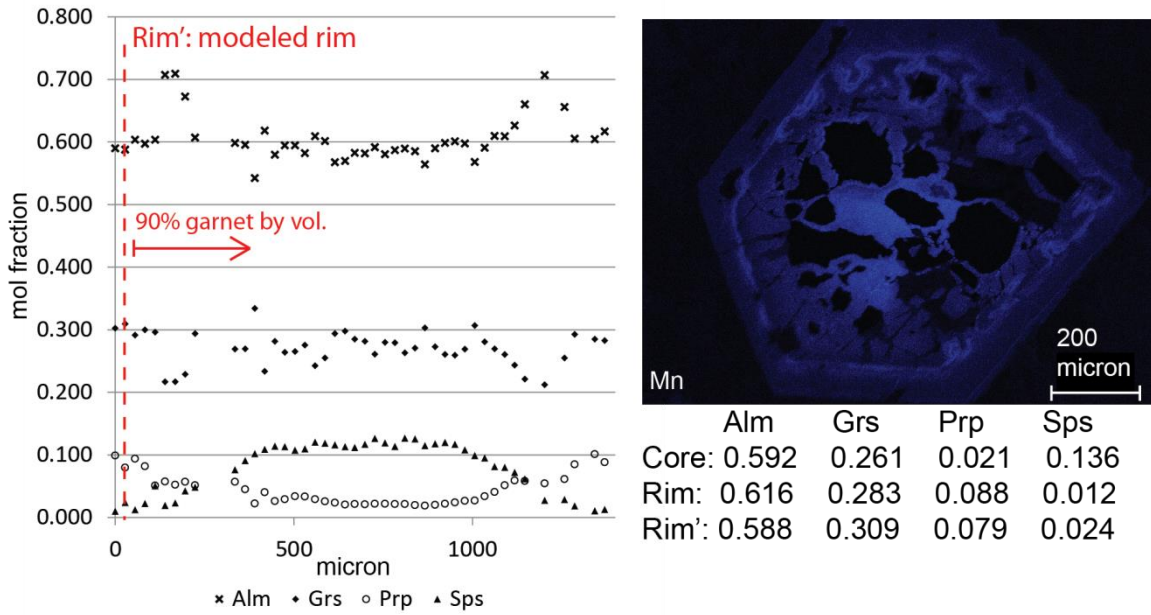


Figure 6 | Rim to rim garnet transect for sample 14BSY-37A. Manganese map of a different garnet from the same sample is shown to the right. The mole fraction of garnet end members at the core and rims are listed. The true rim was unable to be modelled, therefore Rim' values were utilized instead. Core and Rim' were used for thermodynamic modeling while the rim was not.

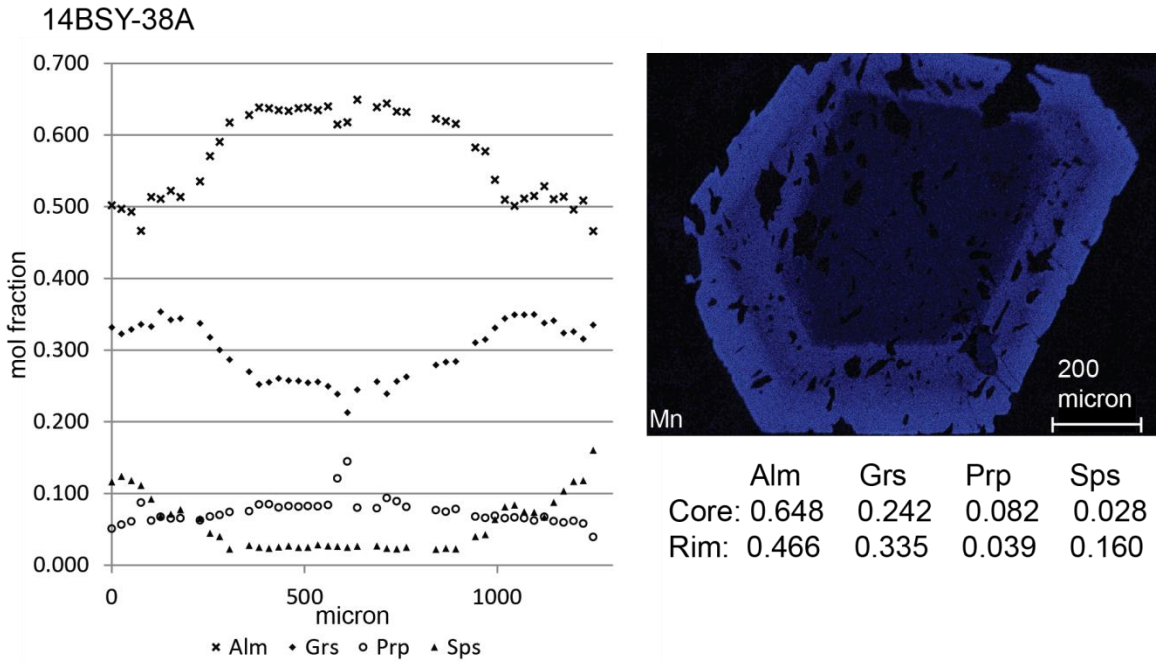


Figure 7| Rim to rim garnet transect for sample 14BSY-38A. Manganese map of a different garnet from the same sample is shown to the right. The mole fraction of garnet end members at the core and rim are listed. Note the unusual inverse manganese zonation and how zonation appears stepped rather than continuous.

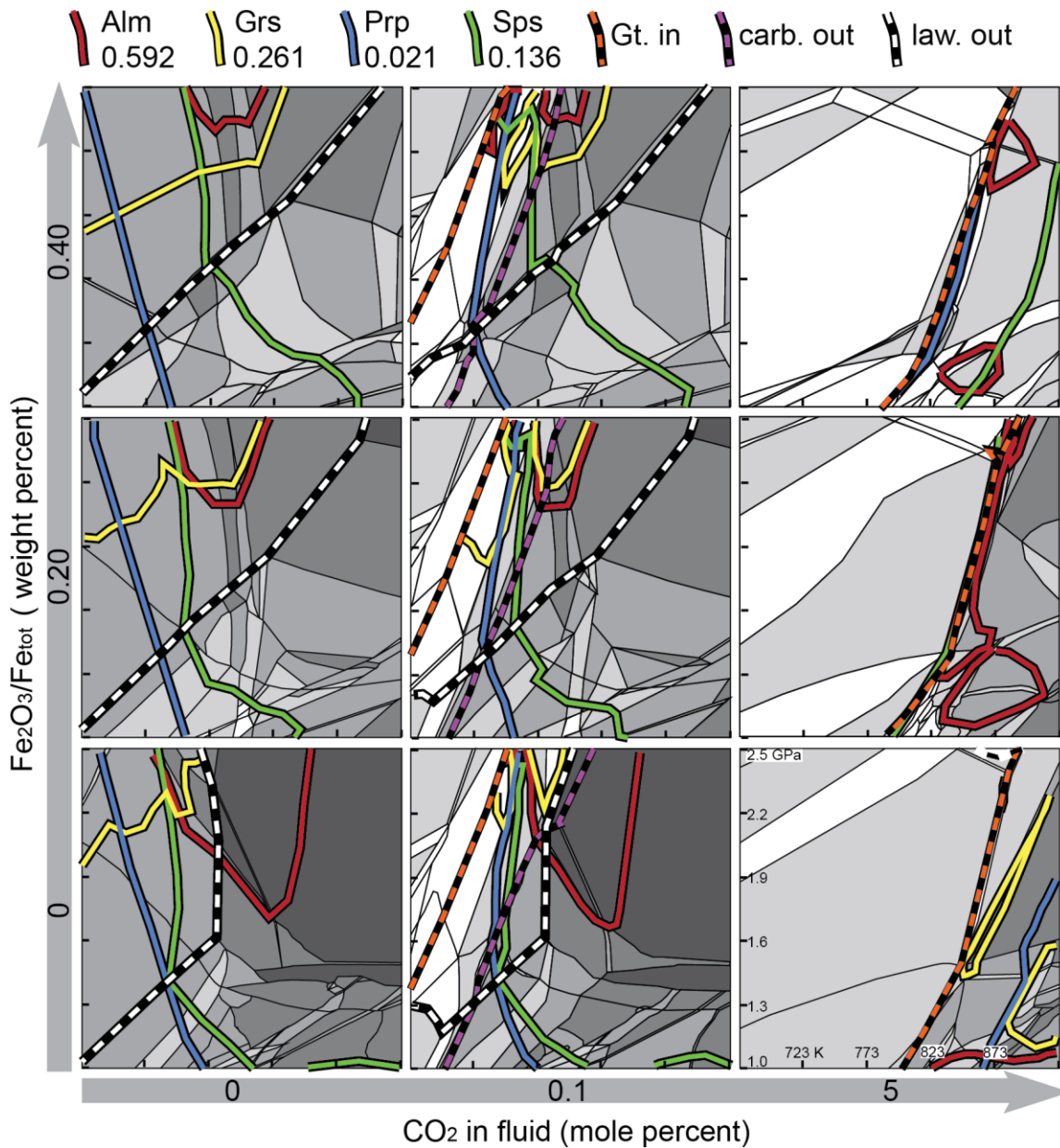


Figure 8| Pseudosections for 14BSY-37A whole rock composition. Axes are the same for each pseudosection and are labeled on the bottom-right pseudosection. Temperature for each plot varies from 673 K to 923 K and pressure varies from 10 to 25 kbar. $\text{Fe}_2\text{O}_3/\text{Fe}_{\text{tot}}$ ratio is 0 for the bottom three pseudosections, 0.20 for the middle (horizontal row) three pseudosections, and 0.40 for the uppermost three pseudosections. Carbonate in fluid is 0 for the left-most three pseudosections, 0.1 mole percent for the center (vertical column) three pseudosections, and 5 mole percent for the right-most three pseudosections. Red, yellow, blue, and green lines are garnet core compositional isopleths. The three pseudosections with the highest carbonate in the fluid are missing isopleths because they did not occur in this P-T space. The upper-right pseudosection is missing a grossular isopleth because predicted grossular content was everywhere higher than 0.261 mol fraction. The middle-right pseudosection is missing a grossular isopleth for the same reason and is also lacking a pyrope isopleth because predicted pyrope content was everywhere higher than 0.021. The lower-right pseudosection is missing a spessartine isopleth because predicted spessartine content was everywhere lower than 0.136. Dashed lines are lawsonite out (white dash), carbonate phases out (purple dash) and garnet in (orange dash). Note that almandine isopleth moves towards higher pressures as ferric iron increases. Note that the garnet-in line moves towards higher

temperatures as carbonate in the fluid increases. The parameters which were determined to be best for this sample are $\text{Fe}_2\text{O}_3/\text{Fe}_{\text{tot}} = 0.09$ and CO_2 in fluid = 0.05 mole percent and are shown in Figure 17.

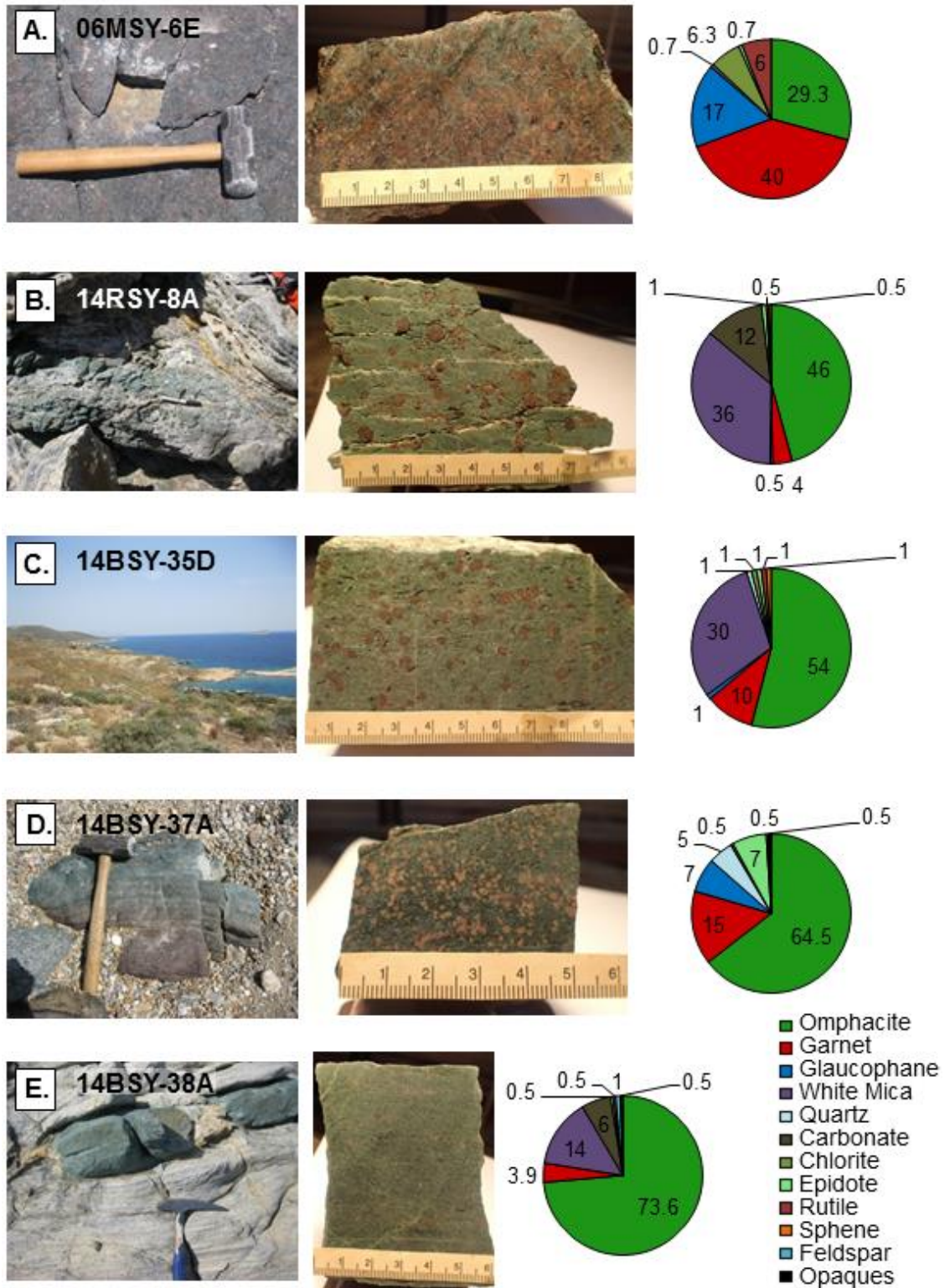


Figure 9 | Field photographs, sample photographs, and modal mineralogy for five eclogite samples in this study. Sample 14BSY-35D was found as float and field photograph shown here is of the general sample location. Sample 14BSY-37A was found as float and field photograph shows size of float as it was found. All samples are dominantly made of omphacite and garnet. Most samples include white mica.

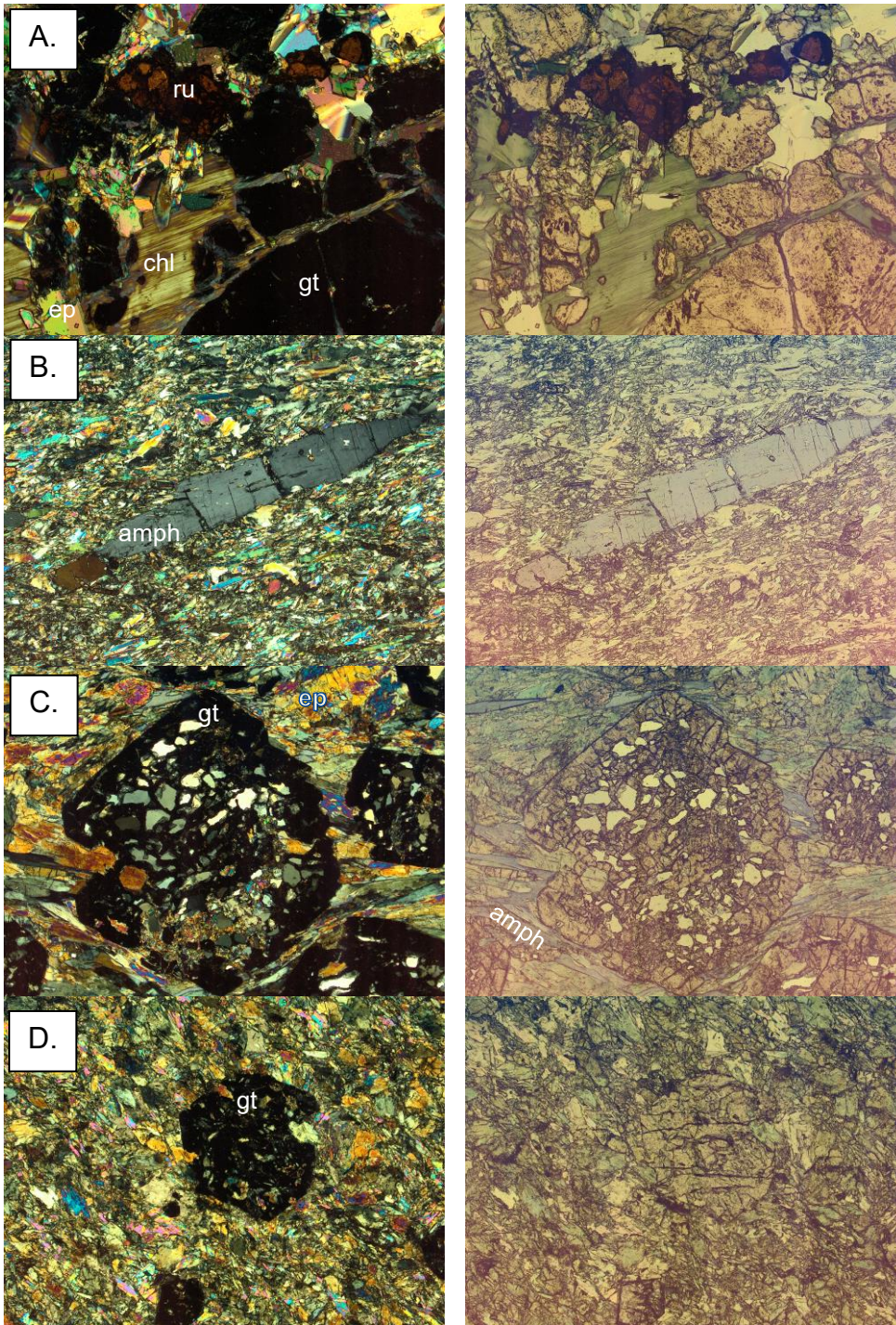


Figure 10 | Representative photo micrographs for the four modeled samples. Width of each image is 3.5 mm A) Sample 06MSY-6E. Note chlorite, garnet, and large clots of rutile. B) Sample 14BSY-35D. Glaucophane porphyroblasts in fine grained omphacite and mica matrix. C) Sample 14BSY-37A. Garnet in omphacite matrix with late glaucophane needles. Inclusions are dominated by quartz. D) Sample 14BSY-38A. Garnet in omphacite and mica matrix

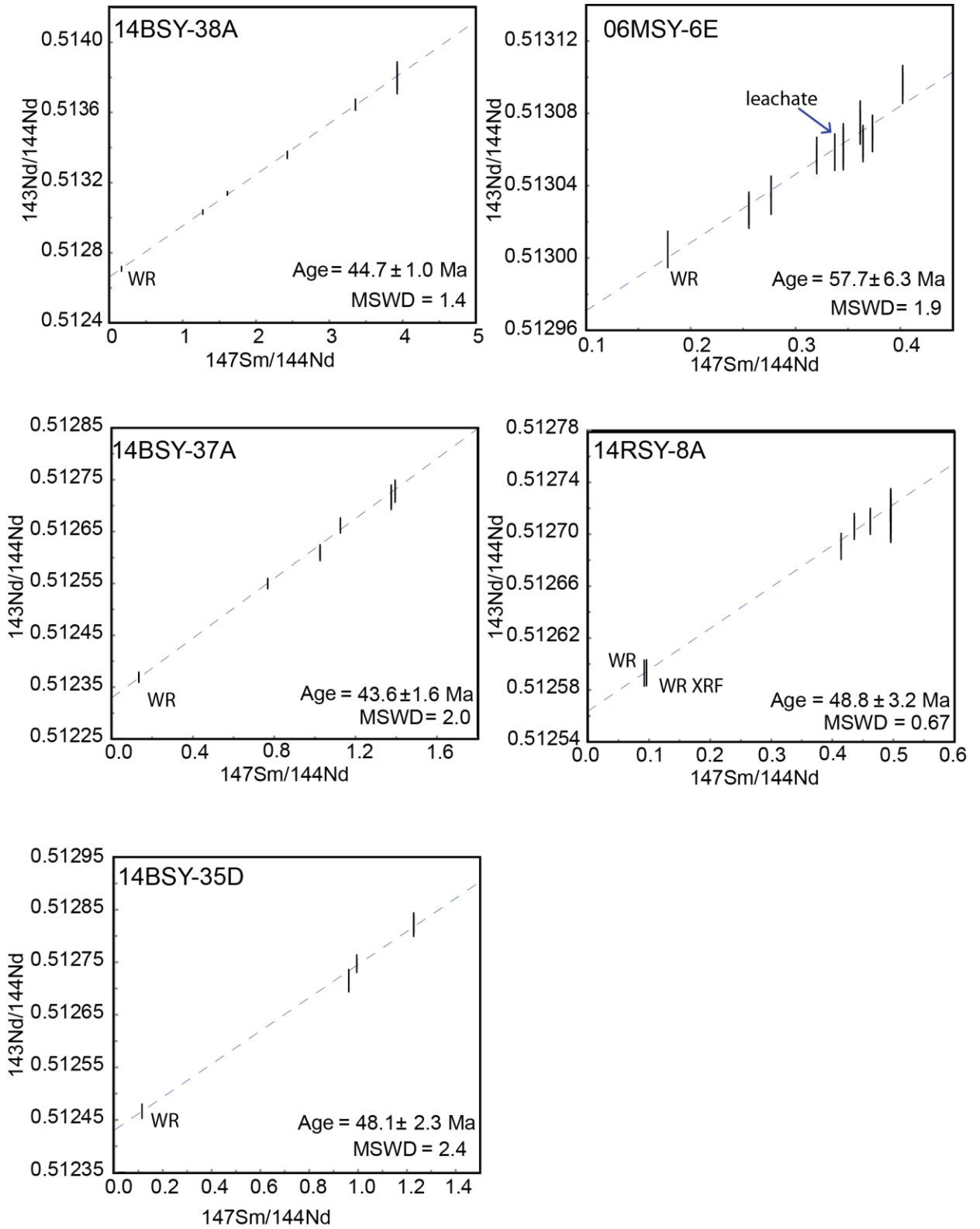


Figure 11 | Isochrons for five eclogites from Syros, Greece. All error bars are 2-sigma. All points not labeled are garnet measurements.

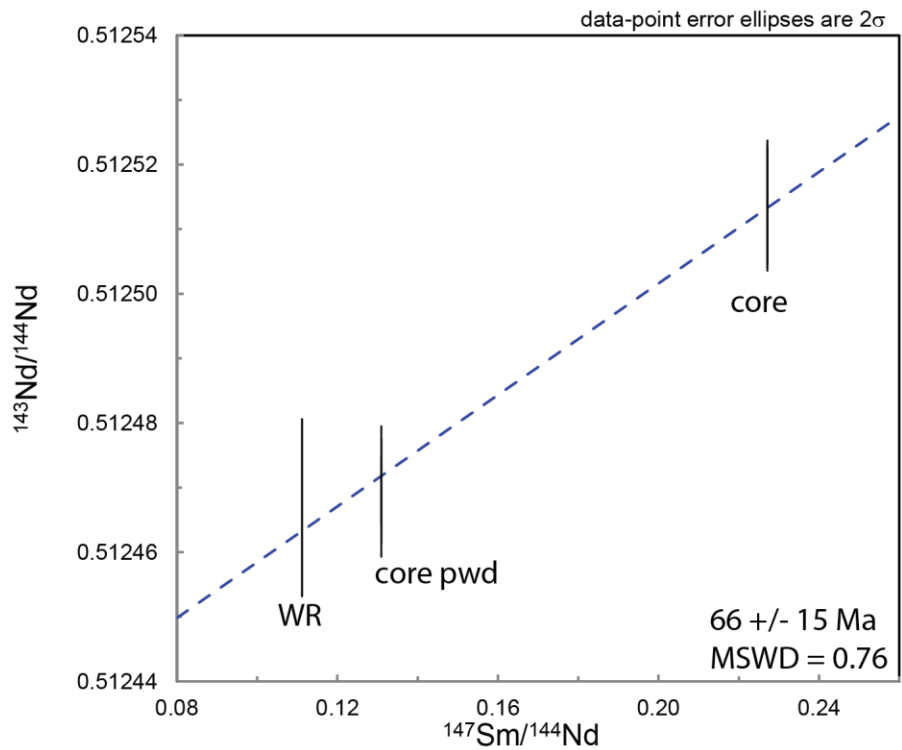
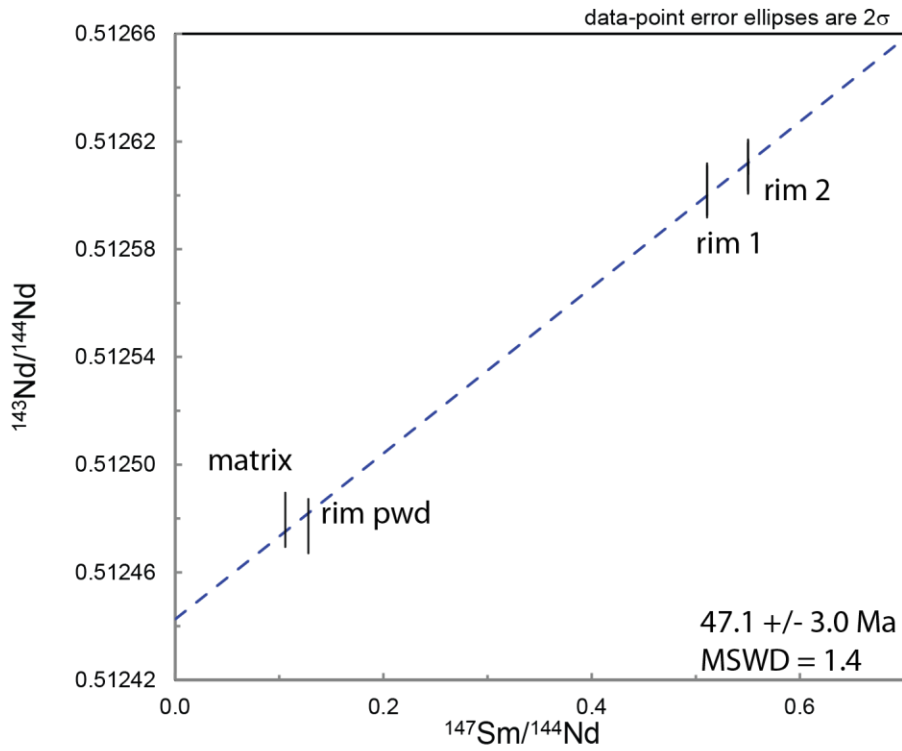


Figure 12 | Isochrons for core and rim ages for sample 14BSY-35D.

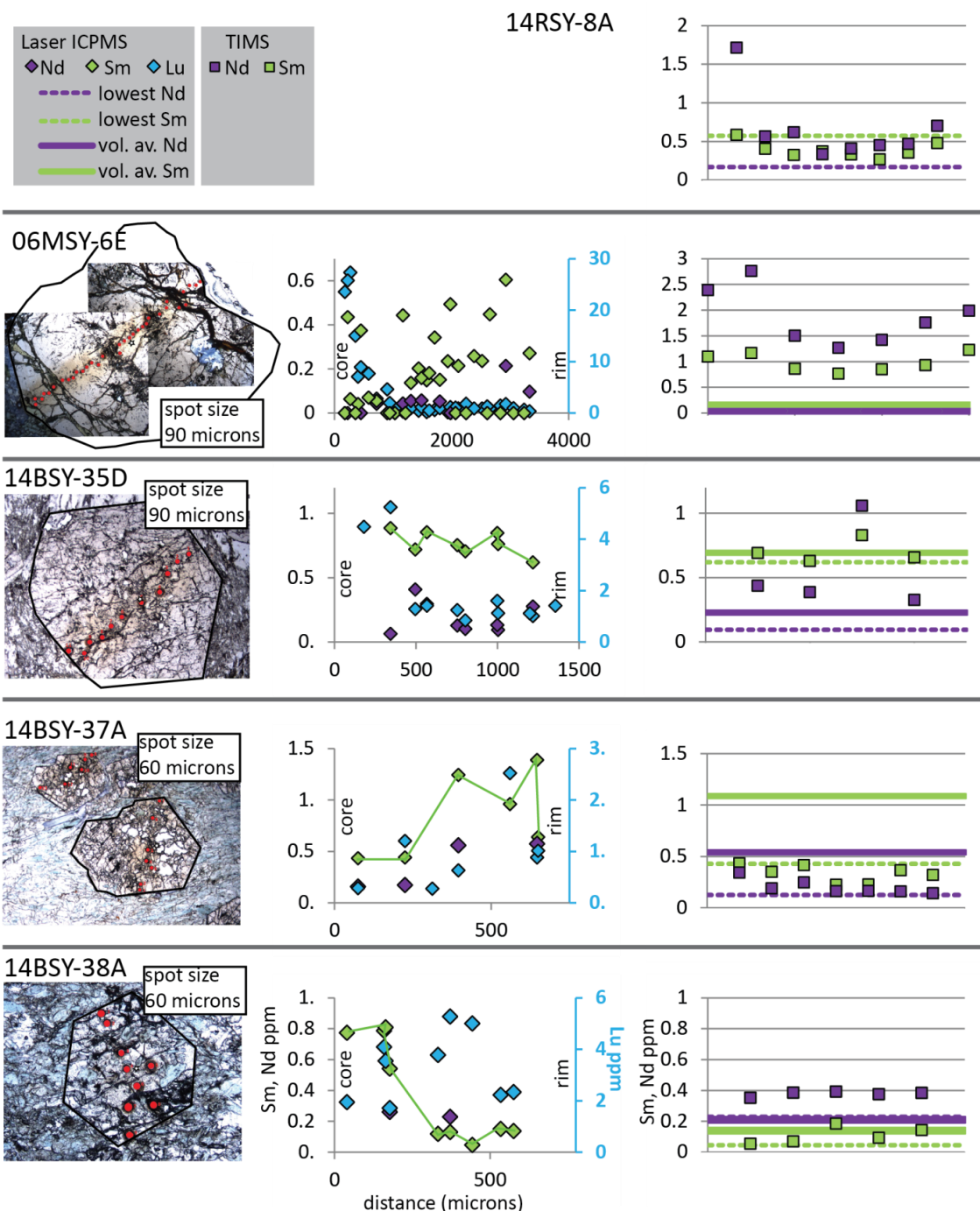


Figure 13 | Photo micrographs with laser ablation spots are shown at left. Concentration of Sm, Nd, and Lu are plotted across garnets from core to rim. Note that lutetium is plotted on a secondary y-axis (blue). Graphs at right show Nd and Sm concentrations for garnet separates as measured with the TIMS, plotted as squares. Dashed purple and green lines represent the lowest Nd and Sm concentrations measured with LA-ICPMS. Solid purple and green lines represent the volumetric average of Nd and Sm measured with LA-ICPMS.

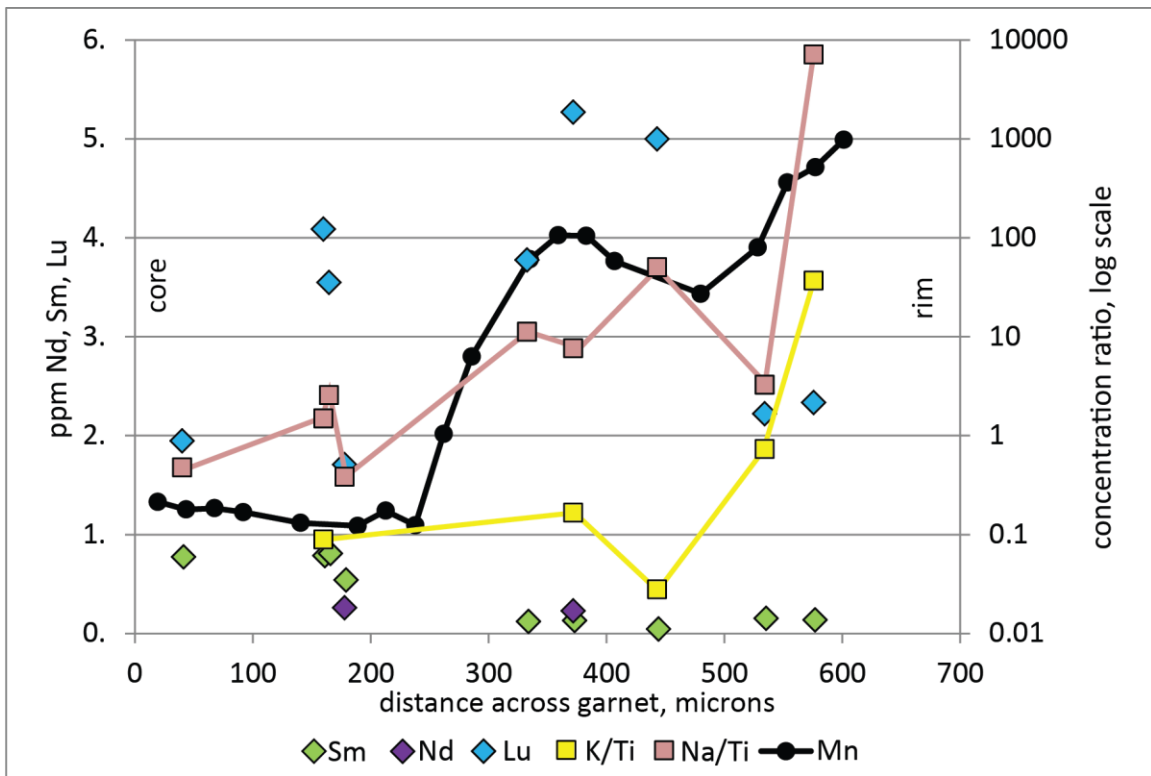


Figure 14 | Sm, Nd, and Lu concentrations measured with LA-ICPMS for sample 14BSY-38A are plotted from core to rim across the garnet. The ratio of Na concentration to Ti concentration and ratio of K concentration to Ti concentration are also plotted. Mn profile measured on the same garnet crystal is plotted *without scale* to show comparison of location in garnet of Mn increases.

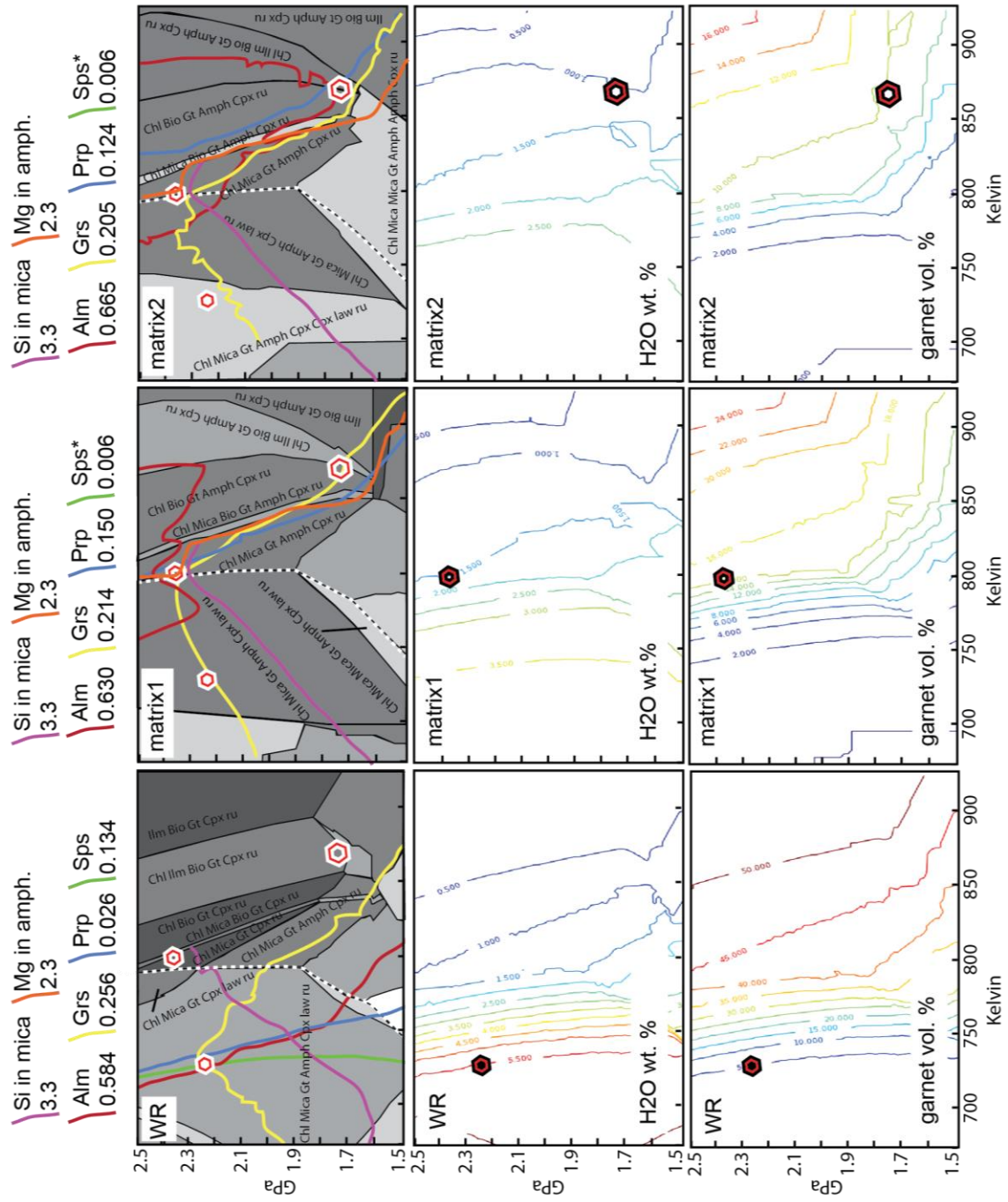


Figure 15 | Pseudosections for sample 06MSY-6E in the system $\text{SiO}_2\text{-TiO}_2\text{-Al}_2\text{O}_3\text{-Fe}_2\text{O}_3\text{-FeO-MgO-CaO-MnO-K}_2\text{O-Na}_2\text{O-H}_2\text{O-CO}_2$. Garnet end member mole fraction isopleths are plotted. Lawsonite out line is shown as dashed white line. Silica in white mica (purple) and magnesium in amphibole (orange) are also plotted. Hexagon icons are placed at core and rim P-T conditions as determined by isopleth intersections. Second row of diagrams shows weight % water held in rock. Note this weight % does not represent the adjusted value calculated in the text. Third row shows garnet volume %. Pseudosections with fully labeled fields are given in Appendix E. Amph=amphibole; arag=aragonite; Bio=biotite; Chl=chlorite; Cpx=clinopyroxene; Do=dolomite; Ep=epidote; Gt=garnet; Ilm=ilmenite; law=lawsonite; Mag=magnesite; Mica=whit mica; q=quartz; ru=rutile; sph=sphene; stlp=stilpnomelene; vsv=vesuvianite; zo=zoisite.

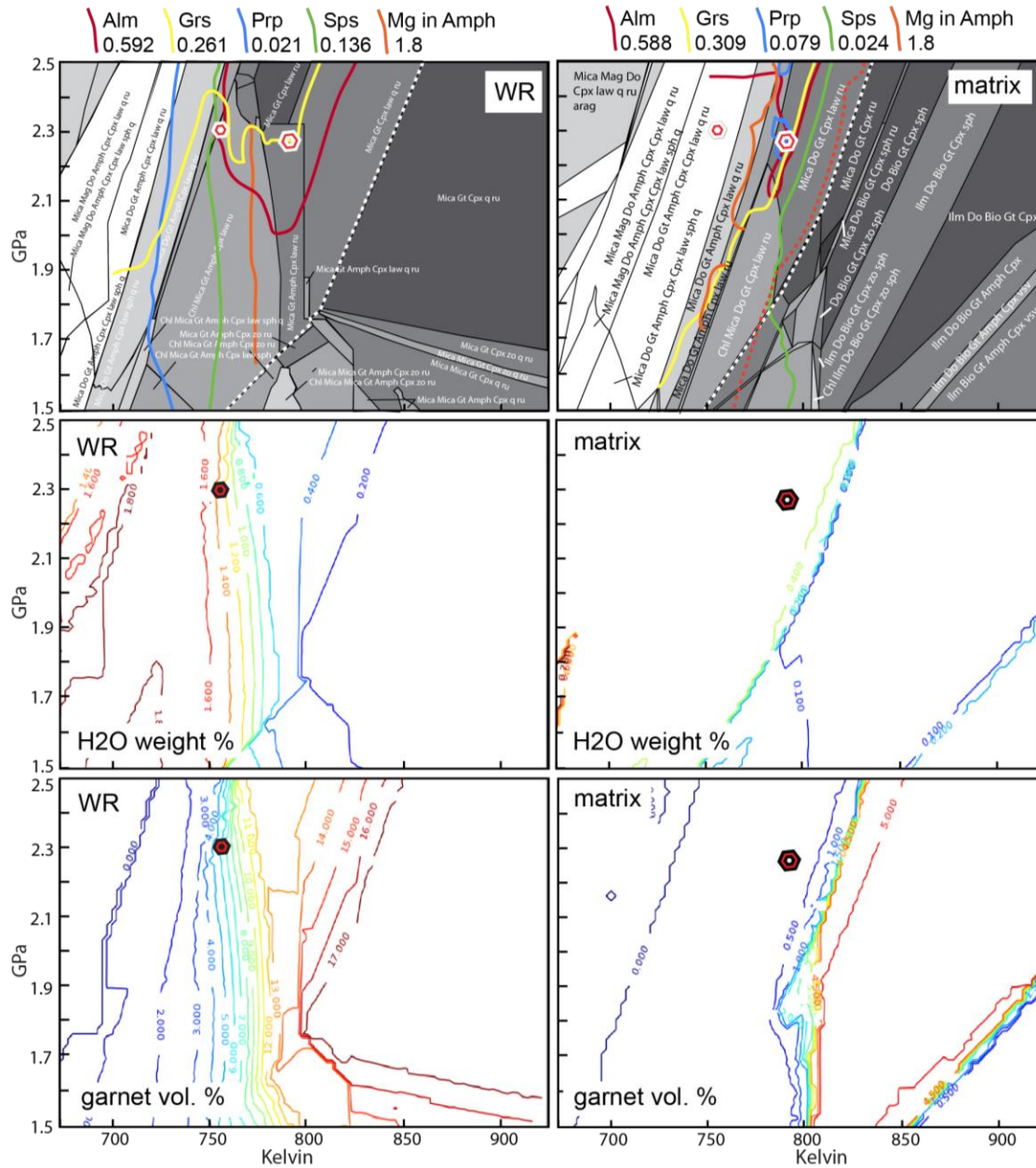


Figure 17 | Pseudosections for sample 14BSY-37A in the system $\text{SiO}_2\text{-TiO}_2\text{-Al}_2\text{O}_3\text{-Fe}_2\text{O}_3\text{-FeO-MgO-CaO-MnO-K}_2\text{O-Na}_2\text{O-H}_2\text{O-CO}_2$. Garnet end member mole fraction isopleths are plotted. Lawsonite out line is shown as dashed white line. Magnesium in amphibole (orange) is plotted. Hexagon icons are placed at core and rim P-T conditions as determined by isopleth intersections. Second row of diagrams shows weight % water held in rock. Note this weight % does not represent the adjusted value calculated in the text. Third row shows garnet volume %. Pseudosections with fully labeled fields are given in Appendix E. Amph=amphibole; arag=aragonite; Bio=biotite; Chl=chlorite; Cpx=clinopyroxene; Do=dolomite; Ep=epidote; Gt=garnet; Ilm=ilmenite; law=lawsonite; Mag=magnesite; Mica=whit mica; q=quartz; ru=rutile; sph=sphene; stlp=stilpnomelene; vsv=vesuvianite; zo=zoisite.

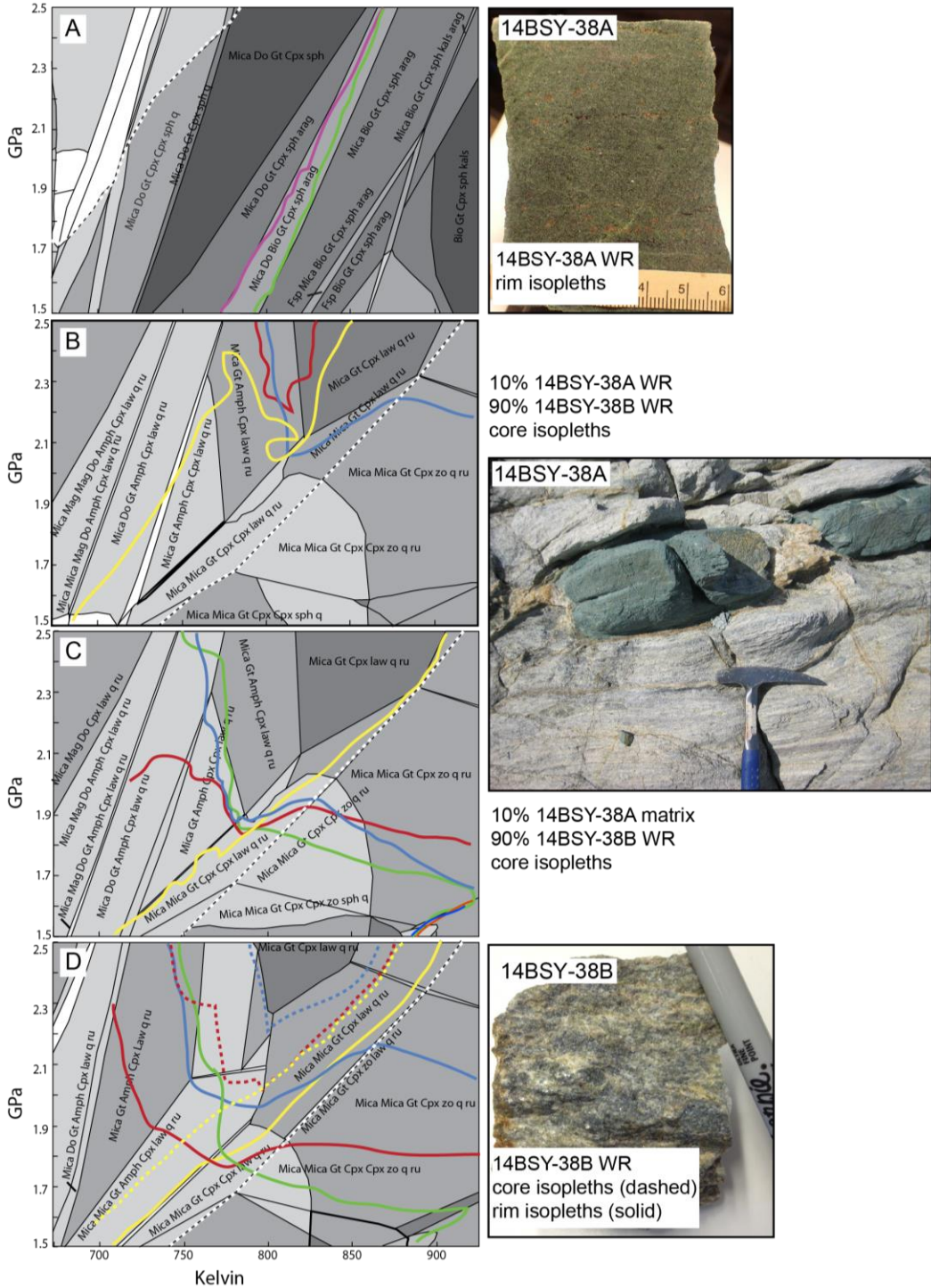


Figure 18 | Pseudosections for sample 14BSY-38A, 14BSY-38A and 14BSY-38B hybrids, and 14BSY-38B in the system $\text{SiO}_2\text{-TiO}_2\text{-Al}_2\text{O}_3\text{-Fe}_2\text{O}_3\text{-FeO-MgO-CaO-MnO-K}_2\text{O-Na}_2\text{O-H}_2\text{O-CO}_2$. Garnet end member mole fraction isopleths are plotted. Lawsonite out line is shown as dashed white line. Silica in mica (purple) is plotted for 14BSY-38A. Sample photos are shown at right. Only the garnet end member isopleth for spessertine at the rim is found in P-T space for 14BSY-38A. For 14BSY-38B, garnet core isopleths are plotted as dashed lines. Pseudosections with fully labeled fields are given in Appendix E. Amph=amphibole; arag=aragonite; Bio=biotite; Chl=chlorite; Cpx=clinopyroxene; Do=dolomite; Ep=epidote; Gt=garnet; Ilm=ilmenite; law=lawsonite; Mag=magnesite; Mica=white mica; q=quartz; ru=rutile; sph=sphene; stlp=stilpnomelene; vsv=vesuvianite; zo=zoisite.

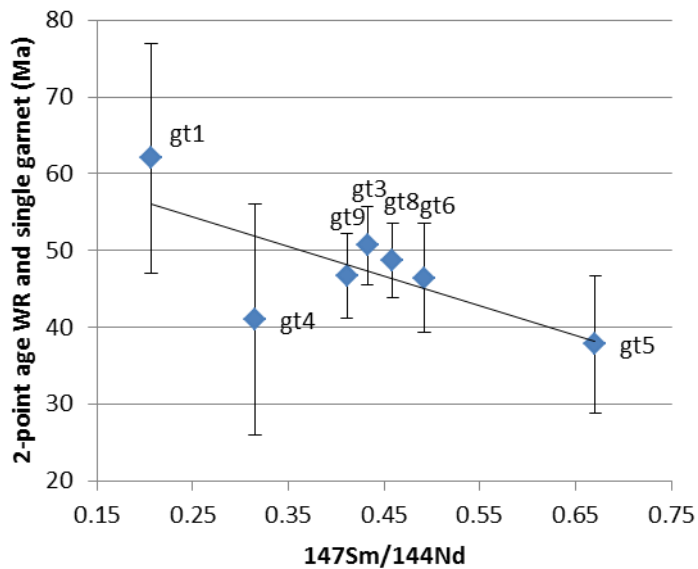
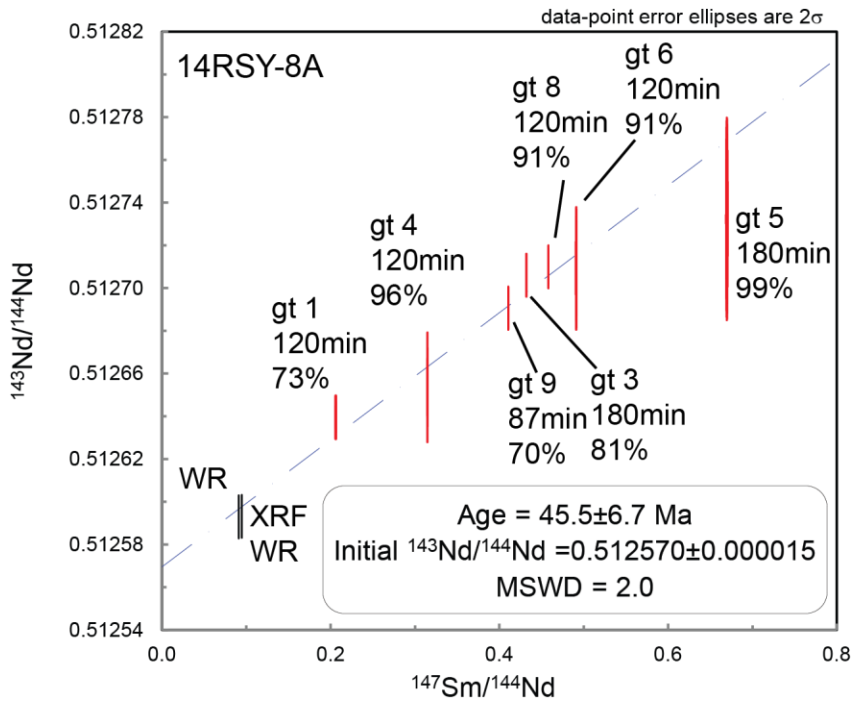


Figure19| Top: Isochron for sample 14RSY-8A. Points are labeled with the name of the garnet separate (gt1, gt2, etc, which will correspond to Table 3), the amount of time the separate was kept in hydrofluoric acid during the partial dissolution, and the percent of the starting sample mass that was lost during the partial dissolution. Bottom: Plot of $^{147}\text{Sm}/^{144}\text{Nd}$ vs the age given by creating an isochron with the whole rock and a single garnet point. Age decreases with “cleaner” (higher $^{147}\text{Sm}/^{144}\text{Nd}$) garnets.

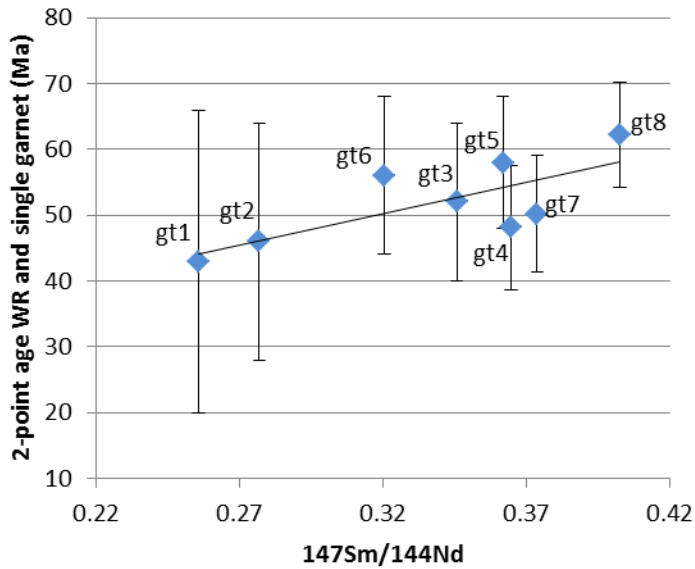
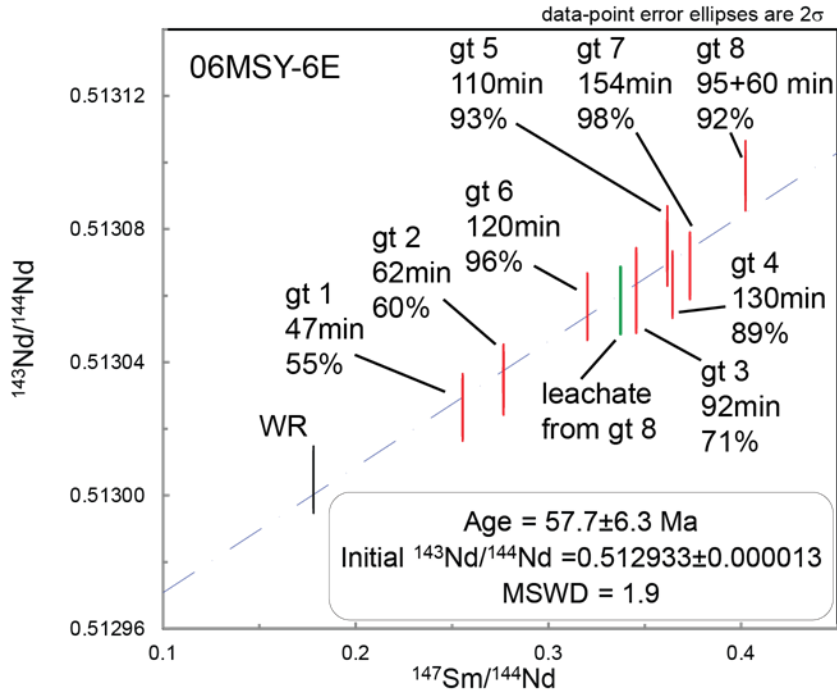


Figure20 | Top: Isochron for sample 06MSY-6E. Points are labeled with the name of the garnet separate (gt1, gt2, etc), the amount of time the separate was kept in hydrofluoric acid during the partial dissolution, and the percent of the starting sample mass that was lost during the partial dissolution. Bottom: Plot of $^{147}\text{Sm}/^{144}\text{Nd}$ vs the age given by creating an isochron with the whole rock and a single garnet point. Age increases with “cleaner” (higher $^{147}\text{Sm}/^{144}\text{Nd}$) garnets.

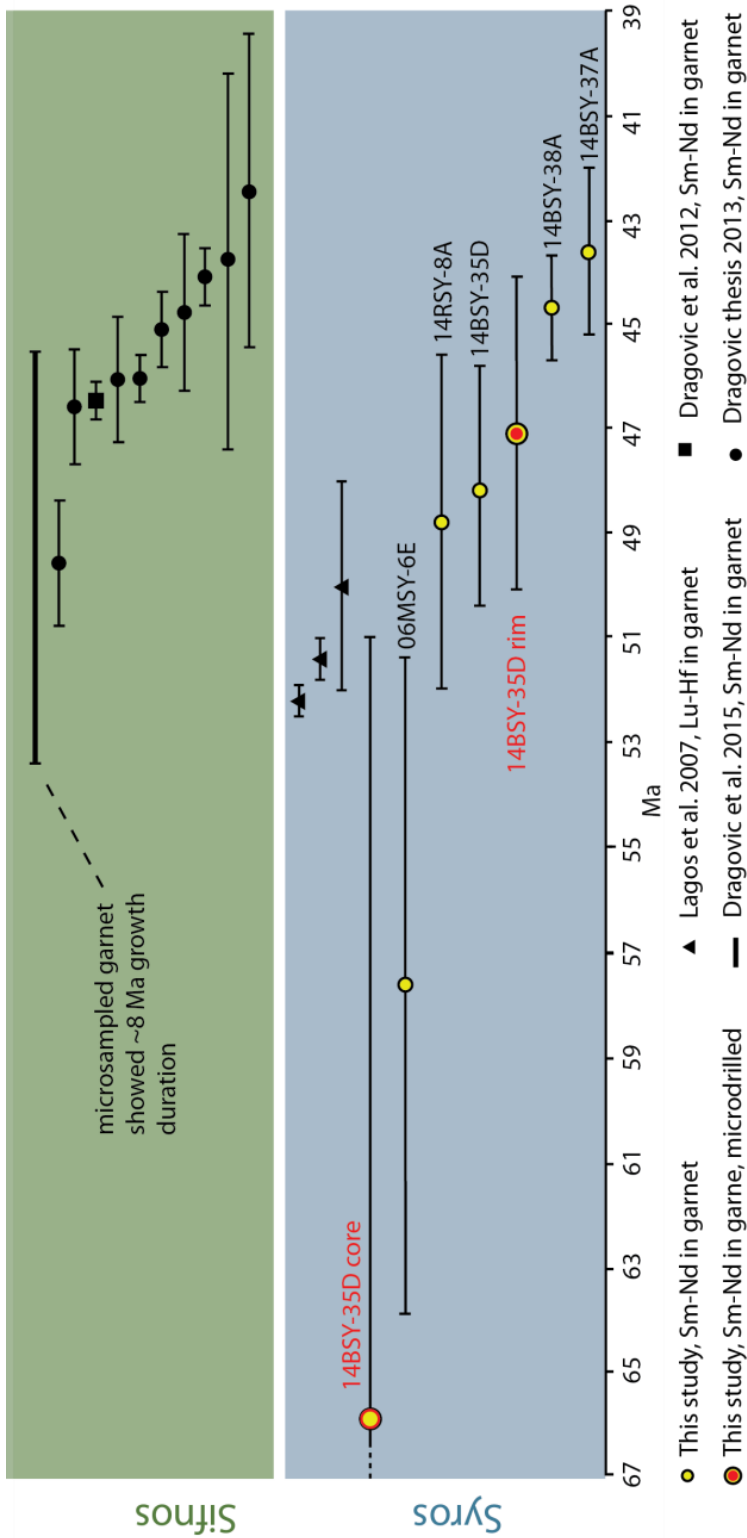


Figure 21 | Garnet ages from Sifnos and Syros islands, spread of ages is similar on both islands. Ages from this study contradict conclusions by Lagos et al., (2007) that peak metamorphism on Syros was a single short event. Core and rim ages for 14BSY-35D are displayed here despite large error bars for 14BSY-35D core. The age is considered unreliable.

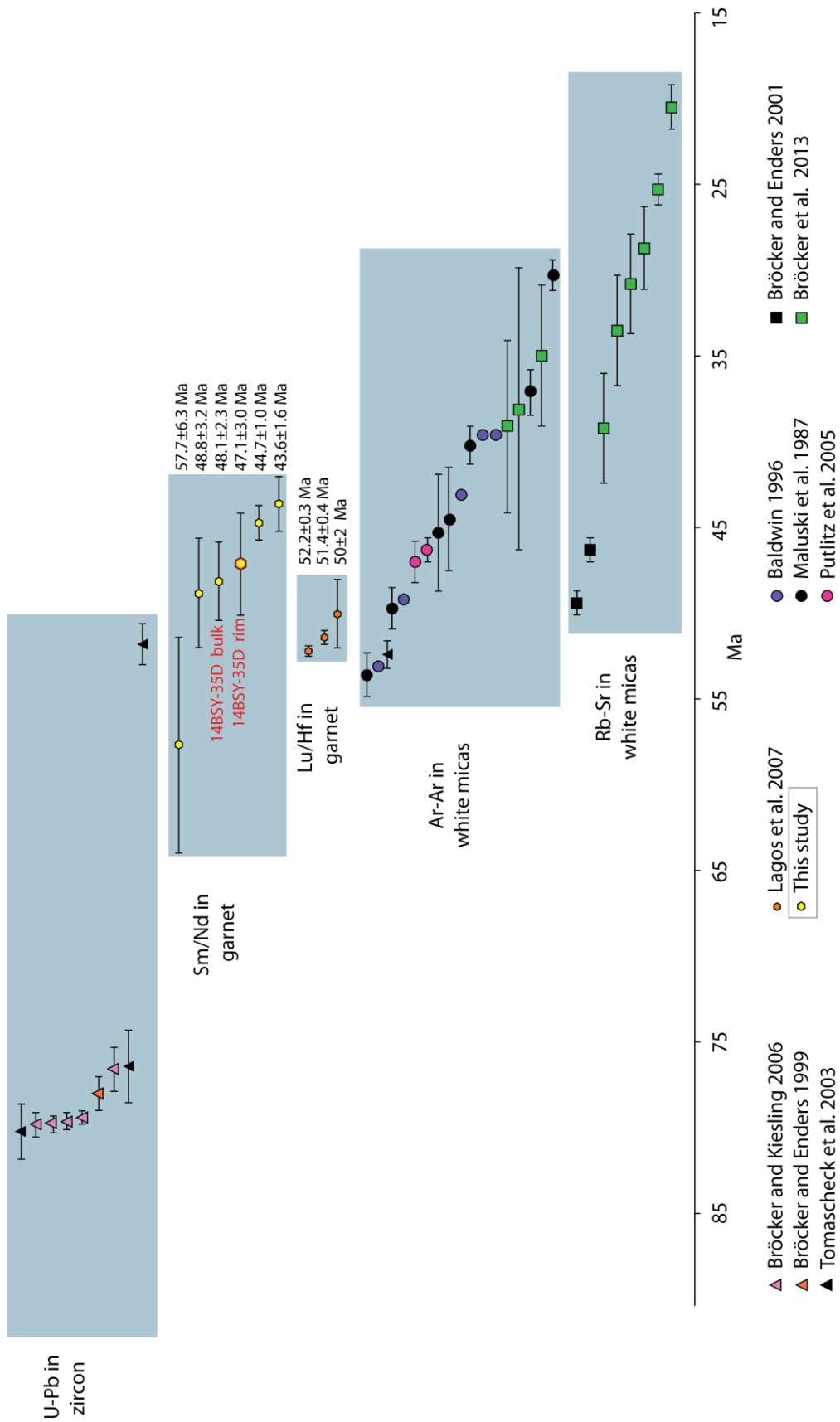


Figure 22 | All geochronology carried out on Syros island. Only one study had previously looked at the age of peak metamorphism using garnet. Core age for 14BSY-35D is not displayed because it is neither accurate nor precise.

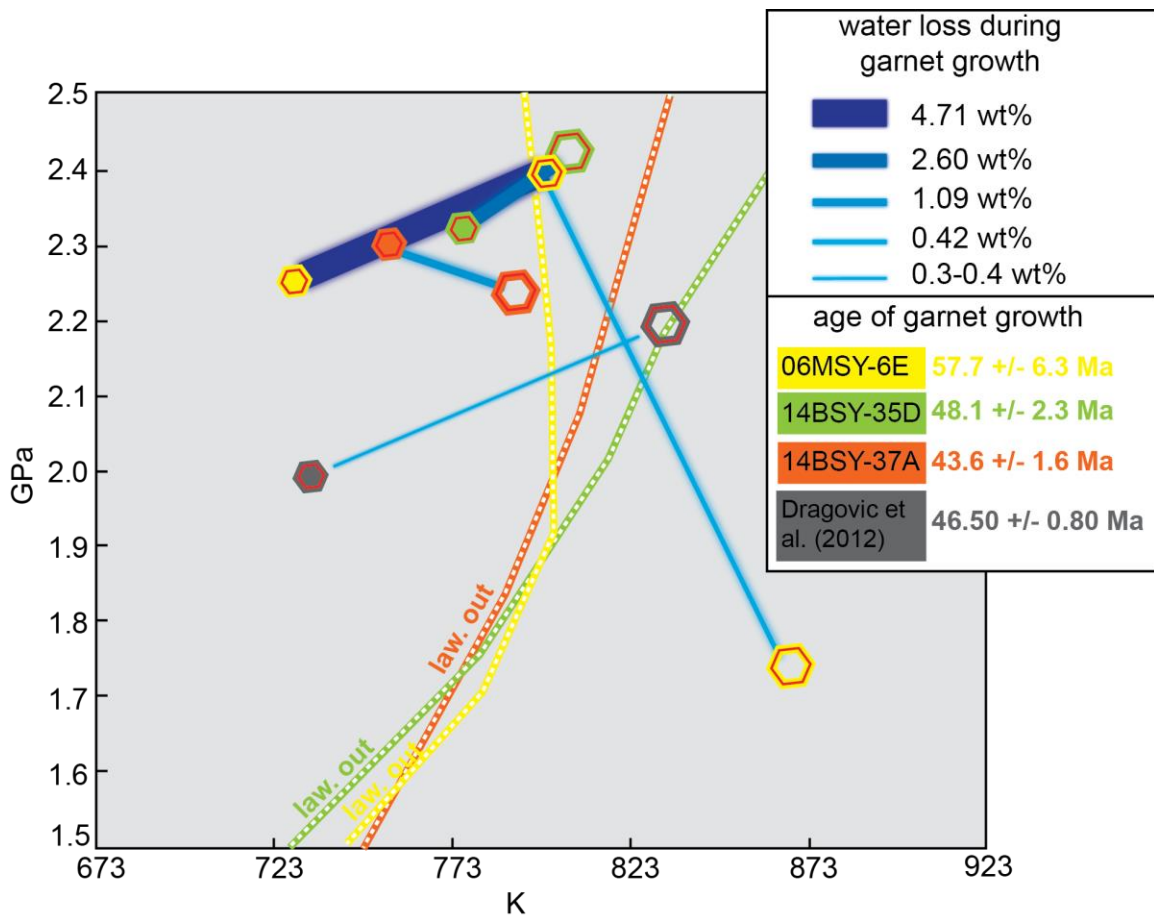


Figure 23 | P-T conditions of garnet core and rim growth determined from thermodynamic modeling are plotted as closed (core) and open (rim) hexagon icons. Icons are color coded by sample. The lawsonite-out line for each sample is also plotted. Blue lines show water loss during garnet growth. Only sample 06MSY-6E crosses the lawsonite out line during garnet growth. This sample also holds and releases the most water, though this is due largely to chlorite stability rather than lawsonite breakdown. A blueschist sample from Sifnos modelled by Dragovic et al. (2012) is shown as a comparison. While the age of garnet growth appears to be comparable between the two islands, P-T conditions of eclogites on Syros appear to be deeper than what has been modeled on Sifnos.

10.0 APPENDICES

10.1 APPENDIX A: TIMS STANDARDS AND BLANKS

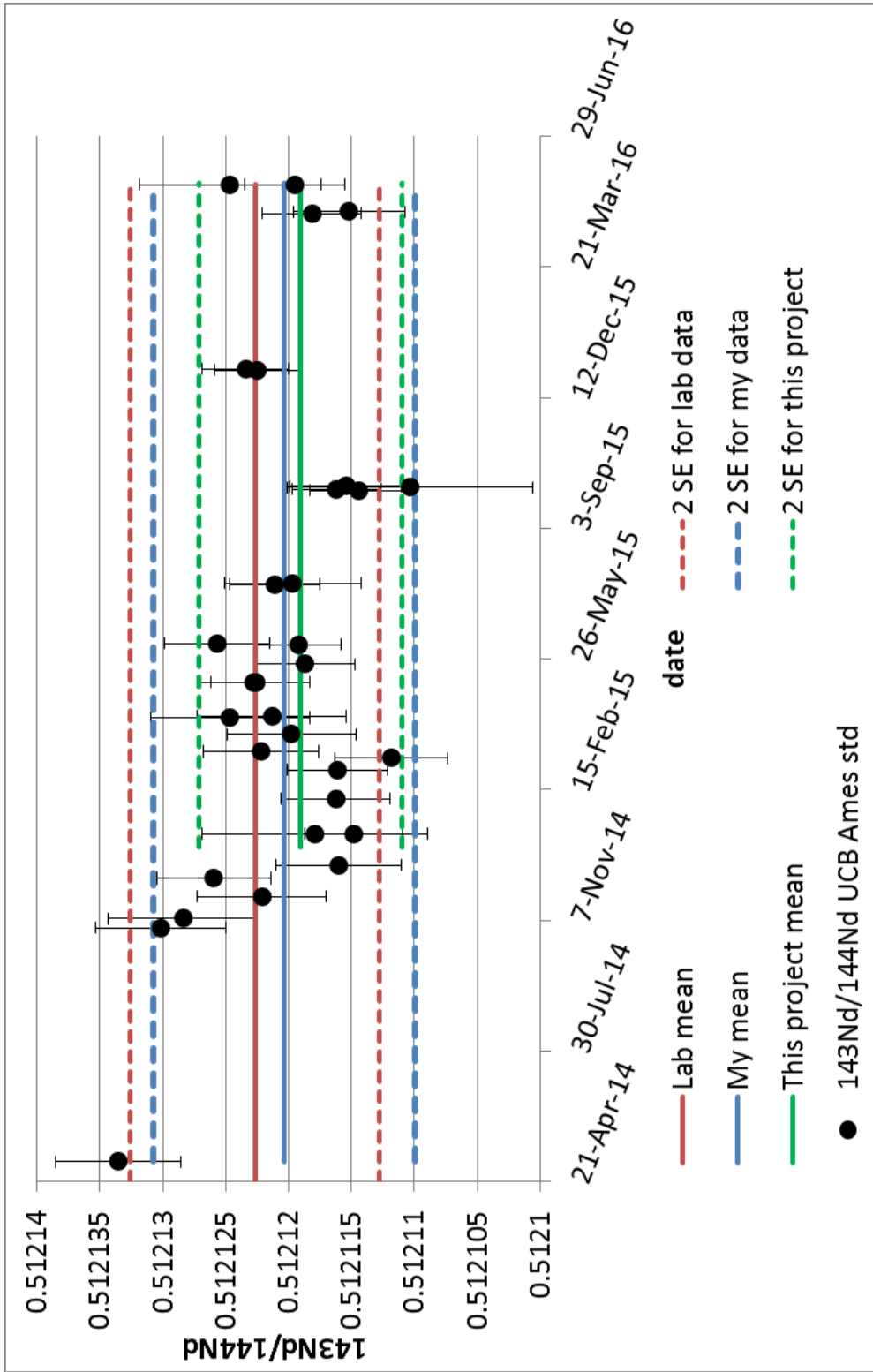


Figure A1: $^{143}\text{Nd}/^{144}\text{Nd}$ UCB Ames standards through time. Standards measured by all users in the lab since April 2013 (red) give an average of $^{143}\text{Nd}/^{144}\text{Nd} = 0.5121226 \pm 0.0000098$ (19.3 ppm, 2RSD, n= 154). Standards measured only by the author for the duration of her time working in lab (blue) give an average of $^{143}\text{Nd}/^{144}\text{Nd} = 0.5121203 \pm 0.0000104$ (20.0 ppm, 2 RSD, n=32). Standards measured by the author for the duration of this project (green) give an average of $^{143}\text{Nd}/^{144}\text{Nd} = 0.5121190 \pm 0.0000081$ (15.7 ppm, 2RSD, n = 26).

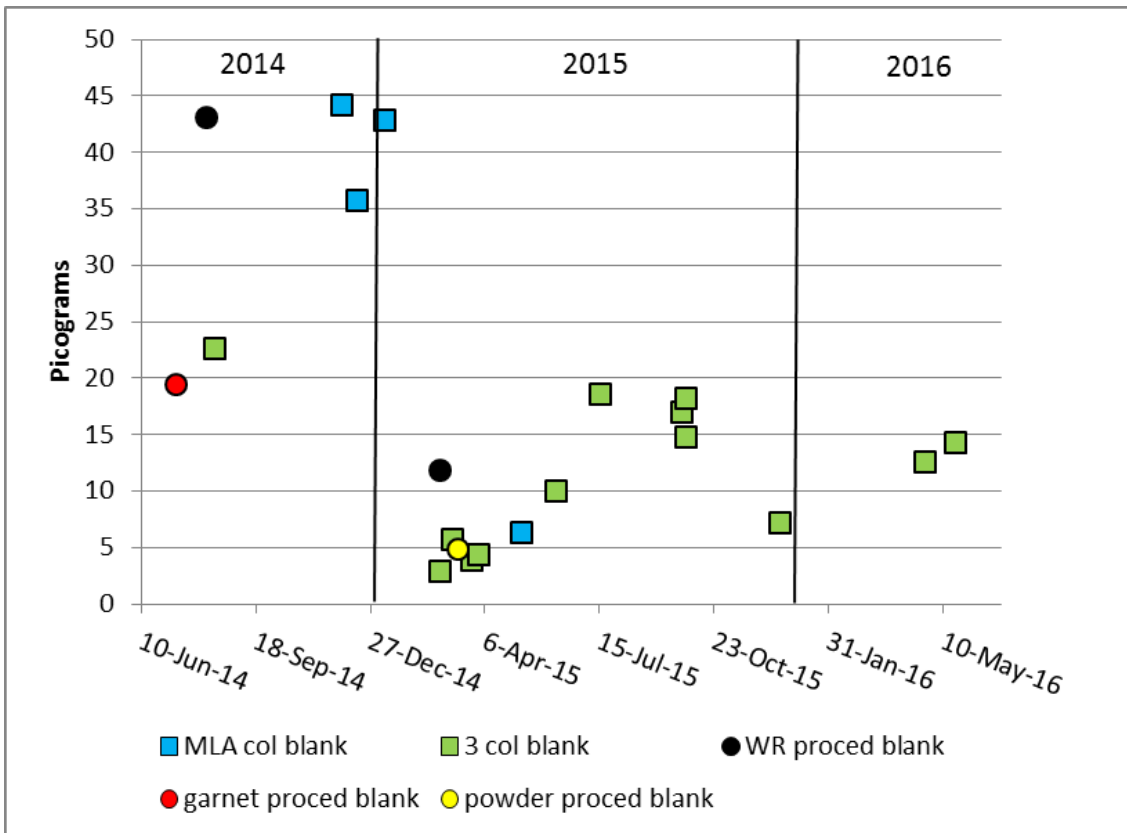


Figure A2: col = column; proced = procedural. Picograms of Nd in blanks through time. MLA column blank refers to the blank measured after running just an MLA column. Three-column blank refers to the blank measured after running iron columns, tru-spec columns, and MLA columns. WR procedural blank is the blank measured after all clean lab steps including dissolution for a whole rock sample. Garnet procedural blank is the blank measured after all clean lab steps for a garnet sample, including a partial dissolution and a full dissolution. A powder procedural blank is the blank measured after all clean lab steps for a garnet powder sample. The average of 3-column and full procedural blanks for the duration of this study is 10.4 picograms of Nd.

10.2 APPENDIX B: SLICES OF ROCK SENT FOR XRF



Figure A3: Images of the pieces of rock sent for XRF. No photo exists of sample 14BSY-35D. Top two photos have permanent marker for scale. Bottom photo shows a standard piece of paper in landscape orientation; the side that is visible is the 11 inch (27.94 cm) side of a piece of paper.

10.3 APPENDIX C: PARAMETERS FOR PERPLE_X RUNS

Example of "my_project" file for 14BSY-37A rims

hp04ver.dat thermodynamic data file
print | no_print suppresses print output
plot | no_plot suppresses plot output
solution_model.dat | solution model file, blank = none

perplex_option.dat | Perple_X option file

5 calculation type: 0 - composition, 1 - Schreinemakers, 3 - Mixed, 4 - gwash, 5 - gridded min, 7 - 1d
fract, 8 - gwash 9 - 2d fract, 10 - 7 w/file input

0 unused place holder, post 06

1 number component transformations

15 number of components in the data base

FE2O3 13 component transformation

0.00 0.00 0.00 0.00 0.00 0.00 0.00 0.00 2.00 0.00 0.00 0.00 0.50

0.00 0.00

1 component amounts, 0 - molar, 1 weight

0 unused place holder, post 06

0 unused place holder, post 06

0 unused place holder, post 05

5 ifug EoS for saturated phase

2 gridded minimization dimension (1 or 2)

0 special dependencies: 0 - P and T independent, 1 - P(T), 2 - T(P)

0.00000 0.00000 0.00000 0.00000 0.00000 Geothermal gradient polynomial coeffs.

begin thermodynamic component list

SiO2 1 54.127 0.00000 0.00000 weight amount

TiO2 1 0.342 0.00000 0.00000 weight amount

Al2O3 1 12.211 0.00000 0.00000 weight amount

MgO 1 6.020 0.00000 0.00000 weight amount

CaO 1 13.354 0.00000 0.00000 weight amount

MnO 1 0.005 0.00000 0.00000 weight amount

FeO 1 5.731 0.00000 0.00000 weight amount

FE2O3 1 1.126 0.00000 0.00000 weight amount

Na2O 1 6.965 0.00000 0.00000 weight amount

K2O 1 0.120 0.00000 0.00000 weight amount

end thermodynamic component list

begin saturated component list

end saturated component list

begin saturated phase component list

H2O

CO2

end saturated phase component list

begin independent potential/fugacity/activity list

end independent potential list

begin excluded phase list

h2oL

ts

parg

gl

oilm

dilm

end excluded phase list

begin solution phase list

Omph(GHP2)

cAmph(DP2)

IlGkPy

Ep(HP)

Mica(CHA)

Gt(WPPH)

feldspar

Chl(HP)

Sp(WPC)

Bio(HP)

Ctd(HP)

M(HP)

oCcM(HP)

end solution phase list

26000.	923.00	0.00100000	0.0000	0.0000	max p, t, xco2, u1, u2
12000.	673.00	0.00100000	0.0000	0.0000	min p, t, xco2, u1, u2
0.0000	0.0000	0.00000000	0.0000	0.0000	unused place holder post 06

2 1 3 4 5 indices of 1st & 2nd independent & sectioning variables

Anotated Solution Models:

Omph(GHP2)	diopside-jadeite-hedenbergite-acmite solution Green et al. (2007) model modified by Diener and Powell (2011)
cAmph(DP2)	clinoamphibole Diener et al. 2008 JMG modified by Diener et al., (2011)
IlGkPy	Ilmenite, Geikielite, Pyrophanite ideal mixing model, no citation
Ep(HP)	clinozoisite-Fe-epidote solution Holland & Powell (1998)
Mica(CHA)	white mica (Ca-Na) no Tschermaks sub allowed Coggon & Holland(2002), Auzanneau et al. (2010)
Gt(WPPH)	margules Ca-Fe ²⁺ -Mg-Al-Fe ³⁺ White et al. (2005)
feldspar	ternary margules or ideal Fuhrman & Lindsley (1988)
Chl(HP)	Chlorite Holland et al. (1998)
Sp(WPC)	Spinel ideal or margules White et al. (2002)
Bio(HP)	Ti-Fe-Mg-Mn Biotite margules Powell & Holland (1999)
Ctd(HP)	Chloritoid White et al. (2000)
M(HP)	magnesite siderite margules Holland & Powell (1998)
oCcM(HP)	asymmetric calcite-magnesite-dolomite solution Holland & Powell (2003)

Example of 'PerpleX_Option' file for 14BSY-37A rims

```

-----
| Run-time Perple_X 6.6.8 options:
| Comments must be preceded by the "|" character.
| Keywords and values are case sensitive!
| For documentation refer to:
|   www.perplex.ethz.ch/perplex_options.html
|-----
1d_path          40 150 | exploratory and autorefine (grid parameters keyword group)
approx_alpha     T   | use approximation  $\exp(x) \sim 1+x$  to evaluate expansivity effect on volume
Anderson-Gruneisen F | Anderson-Gruneisen parameter correction for polythermal Murnaghan
and Birch-Murnaghan
auto_refine      aut | auto, manual, or off (auto_refine keyword group)
auto_refine_factor_I  2 | refine factor for gridded minimization and phase fractionation
(auto_refine keyword group)
auto_refine_factor_II 6 | refine factor for composition and mixed variable diagrams (auto_refine
keyword group)
auto_refine_factor_III 2 | refine factor for Schreinemakers diagrams (auto_refine keyword group)
auto_refine_file  F   | echo auto-refine data to my_project_auto_refine.txt
bad_number       NaN | any number or NaN (not-a-number)
bounds           VRH | [VRH] HS; Voigt-Reuss-Hill or Hashin-Shtrikman, see vrh/hs_averaging
closed_c_space   T   | T[rue] or F[alse], default is T => closed composition space for gridded
minimization
composition_constant F | T[rue] or F[alse], default is F; allows constants in composition
expressions
composition_phase mol | mol or wt; phase compositions in WERAMI output
composition_system wt | mol or wt; system composition in WERAMI mode 2-4 output
console_messages on | on or off
dependent_potentials on | on or off
efficiency       3 | 1->5
explicit_bulk_modulus T | T[rue] or F[alse], default is F; T => use explicit function for K if
available
fd_expansion_factor 2 | [2], nth order finite difference increment is increased by
fd_expansion_factor^(n-1)
final_resolution  1e-2 2.5e-4 | >0, <1, default 1e-3; exploratory and autorefine
finite_difference_p 1d4 1d-2 | threshold [1d4] and fraction [1d-2] for 1st order finite difference
increment on pressure
global_reach_increment 0 | >= 0; overridden by reach_factor specified in solution model file
grid_levels      1 4 | exploratory and autorefine (grid parameters keyword group)
hard_limits      off | on or off; on => use compositional limits specified in solution model
increment        0.1 0.025 | 0, <1; exploratory and autorefine
initial_resolution 0.060 | >0, <1, default 1e-2
interpolation    on 2 | value 1: on or off [on]; value 2, 1->99 [2]
iteration         3 4 | value 1: 2->99 [3]; value 2: 1->7 [4]
linear_model     on | on or off
logarithmic_p    F   | T[rue] or F[alse], default is F
melt_is_fluid    F   | T[rue] or F[alse], default is F
option_list_files T | T[rue] or F[alse], T => echo run-time options to
my_project_PROGRAM_options.txt
order_check      on | on or off, on => compare order-disorder solutions with fully ordered and
disordered states
pause_on_error   T   | T[rue] or F[alse], T => wait for user response after errors
pc_perturbation  5d-3 | perturbation to pseudo-compound compositions, for Schreinemakers
and Mixed-variable calculations

```

poisson_ratio on 0.35 | value 1: on, off or all; value 2: 0->0.5; poisson ratio estimates for shear
 moduli
 poisson_test F | T[rue] or F[alse], default is F, T => use poisson ratio to check for valid
 results
 proportions vol | vol or wt; phase proportions
 pseudocompound_file F | echo static pseudocompound compositions to
 my_project_pseudocompound_list.txt
 reach_increment_switch on | all, on, off; default is on; all consumes more resources
 reaction_format minimum | minimum, full, stoich, S+V, or everything
 reaction_list off | on or off
 seismic_output some | all, some, none
 short_print on | on or off
 site_check T | T[rue] or F[alse], T=> reject solution compositions with negative site
 fractions
 solution_names abb | mod[el], abb[reviation], ful[l]
 solvus_tolerance auto | auto or 0->1 [0.05] should be > initial_resolution/auto_refine_factor
 solvus_tolerance_II 0.3 | 0->1 [0.25]
 speciation_tolerance 1d-3 | tolerance for order-disorder speciation calculations, >0,<1 [1d-3]
 speciation_max_it 100 | max number of iterations permitted in speciation/order-disorder
 calculations
 species_output T | T[rue] or F[alse], T => output phase speciation in MEEMUM/WERAMI
 mode 1 output
 spreadsheet T | T[rue] or F[alse], T => include independent variable values in werami tab
 output files
 stretch_factor 0.016 | >0, <1
 subdivision_override off | off, linear, or stretch
 T_melt 873. | melt solution model endmember temperature (K) cut off
 T_stop 0. | equilibration temperature (K) cut off
 variance 1 99 | 1->99; exploratory and autorefine
 vrh/hs_weighting 0.5 | 0->1, weighting factor for the stiff average in VRH/HS averaging (see
 bounds)
 x_nodes 5 10 | exploratory and autorefine (grid parameters keyword group)
 y_nodes 5 10 | exploratory and autorefine (grid parameters keyword group)
 zero_mode 1e-6 | 0->1
 zero_bulk 1e-6 | 0->1

10.4 APPENDIX E: EXPLORATORY GEOCHRONOLOGY

Seven samples not included in this study were processed during exploratory geochronology. Of the seven samples, five were blueschists, one was a quartz-mica schist, and one was an eclogite (Table A3). All samples proved to be non-ideal for geochronology as evidenced by low $^{147}\text{Sm}/^{144}\text{Nd}$ after partial dissolution (Table A4).

Table A1: Samples used in exploratory geochronology

Sample name	Description
14BSY-2A1	Quartz mica schist with ~2cm garnet heavily retrogressed to chlorite
14BSY-17A	Blueschist with garnets, omphacite and lawsonite pseudomorphs
14CSY-20A	Pale blue blueschist with small garnets and lawsonite pseudomorphs
14BSY-31B	Blueschist with garnet, relict pillow structure
14BSY-35C2	Eclogite with 1 cm garnet and blueschist needles
14BSY-67C	Blueschist with small garnets and lawsonite pseudomorphs
Horst	Blueschist with large (~5cm) garnet porphyroblast

Table A2: Exploratory isotopic data

	147Sm/14 4Nd	143Nd/14 4Nd	147Sm/144 Nd error	143Nd/144 Nd error	ng Nd	ng Sm	ppm Nd	ppm Sm	minutes in HF	mg garnet to start	percent loss during partial	mesh size fraction
14BSY-2A1	gt1	0.184157	0.512751	8.340E-04	4.930E-06	27.23	8.29	0.75	0.23	150	100	63.5
	gt2	0.170469	0.512742	2.906E-05	4.694E-06	31.38	8.84	1.16	0.33	90	63	57
	gt3	0.293493	0.512787	1.236E-04	2.384E-05	1.73	0.84	0.20	0.10	120	106	85
14BSY-17A	WR XRF AQ1	0.137843	0.512729	1.055E-04	5.805E-06	11.53	2.63	22.70	5.17	-	-	-
	gt1	0.17992	0.512871	1.750E-04	1.285E-05	2.04	0.61	0.16	0.05	150	71	82
14CSY-20A	WR XRF AQ1	0.19681	0.512889	6.385E-05	5.451E-05	5.48	1.78	6.76	2.20	-	-	-
	gt1	0.169637	0.512947	8.814E-05	1.817E-05	2.50	0.70	0.25	0.07	150	69.4	85
	gt2	0.17023	0.51295	2.243E-05	9.170E-06	9.90	2.79	0.37	0.11	~105	-	140-230
	gt3	0.172617	0.512959	3.388E-05	5.827E-06	10.73	3.06	0.40	0.11	110	-	140-230
	gt pwd AQ1	0.160943	0.512935	8.966E-06	4.999E-06	18.71	4.98	4.79	1.27	-	-	-
WR XRF AQ1	0.164601	0.512929	5.490E-05	7.180E-06	8.73	2.38	17.58	4.79	-	-	-	-

Table A2 cont.

	147Sm/14 4Nd	143Nd/14 4Nd	147Sm/144 Nd error	143Nd/144 Nd error	ng Nd	ng Sm	ppm Nd	ppm Sm	minutes in HF	mg garnet to start	percent loss during partial	mesh size fraction
14BSY-31B	gt1	0.170182	0.513005	6.151E-04	8.251E-06	7.23	2.03	0.66	0.18	60	96	140-230
	gt2	0.231716	0.513021	2.685E-05	2.038E-05	2.13	0.82	0.21	0.08	120	129	140-230
	gt pwd AQ1	0.163031	0.513003	2.799E-05	5.262E-06	20.20	5.44	4.87	1.31	-	-	-
	WRAQ1	0.174369	0.512994	1.137E-04	9.883E-06	14.22	4.10	17.51	5.05	-	-	-
	WR XRF AQ1	0.183179	0.513016	1.430E-05	1.003E-05	13.97	4.23	17.18	5.20	-	-	-
14BSY-35C2	gt1	0.245204	0.512515	4.491E-05	6.411E-06	9.65	3.91	0.64	0.26	150	63.7	100-200
	gt pwd AQ1	0.116643	0.512489	1.699E-05	4.869E-06	45.53	8.78	11.09	2.14	-	-	-
	WR XRF AQ1	0.101256	0.512475	1.205E-05	6.021E-06	12.62	2.11	15.50	2.59	-	-	-
14BSY-67C	GT2.1 gt1	0.196902	0.513004	5.462E-05	8.784E-06	9.27	3.02	0.63	0.20	120	-	140-200
	GT2.1 gt2	0.197166	0.513008	2.255E-04	9.011E-06	5.82	1.90	0.59	0.19	120	-	140-200
Horsf	gt1	0.337219	0.513034	8.671E-04	2.522E-05	1.65	0.92	0.28	0.15	150	67	100-200
	gt2	0.363303	0.513054	1.525E-04	1.555E-05	2.42	1.45	0.36	0.22	120	-	140-230
	gt pwd AQ1	0.164858	0.512993	8.643E-06	6.291E-06	37.28	10.16	9.12	2.49	-	-	-
	WR XRF AQ1	0.182956	0.513008	4.439E-05	7.179E-06	12.09	3.66	24.27	7.34	-	-	-

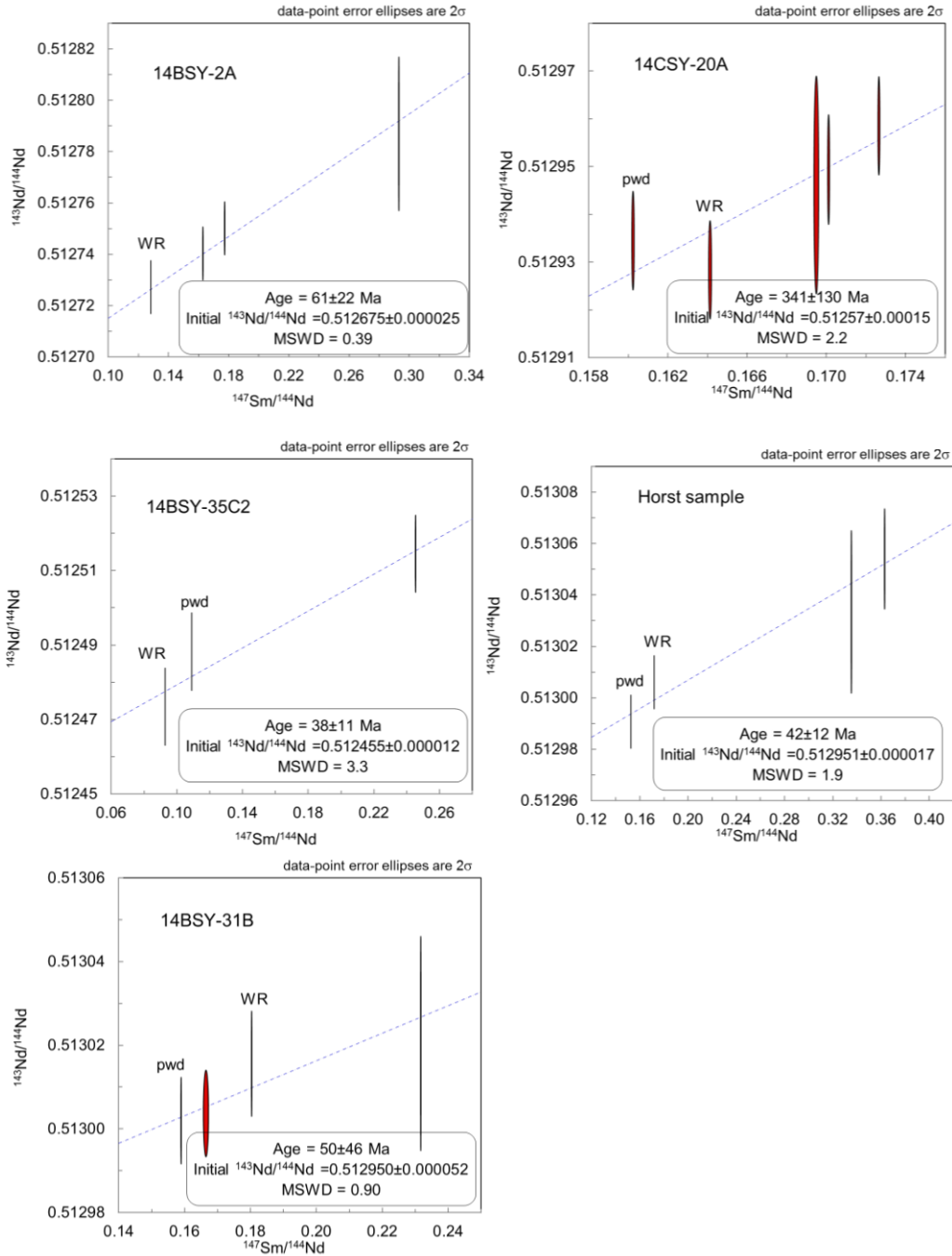


Figure A4: Isochrons for exploratory geochronology. Samples 14BSY-17A and 14BSY-67C are not included. Whole rock (WR) and powder (pwd) points are labeled. Unlabeled points are garnet measurements.

10.5 APPENDIX D: LABELED PSEUDOSECTIONS

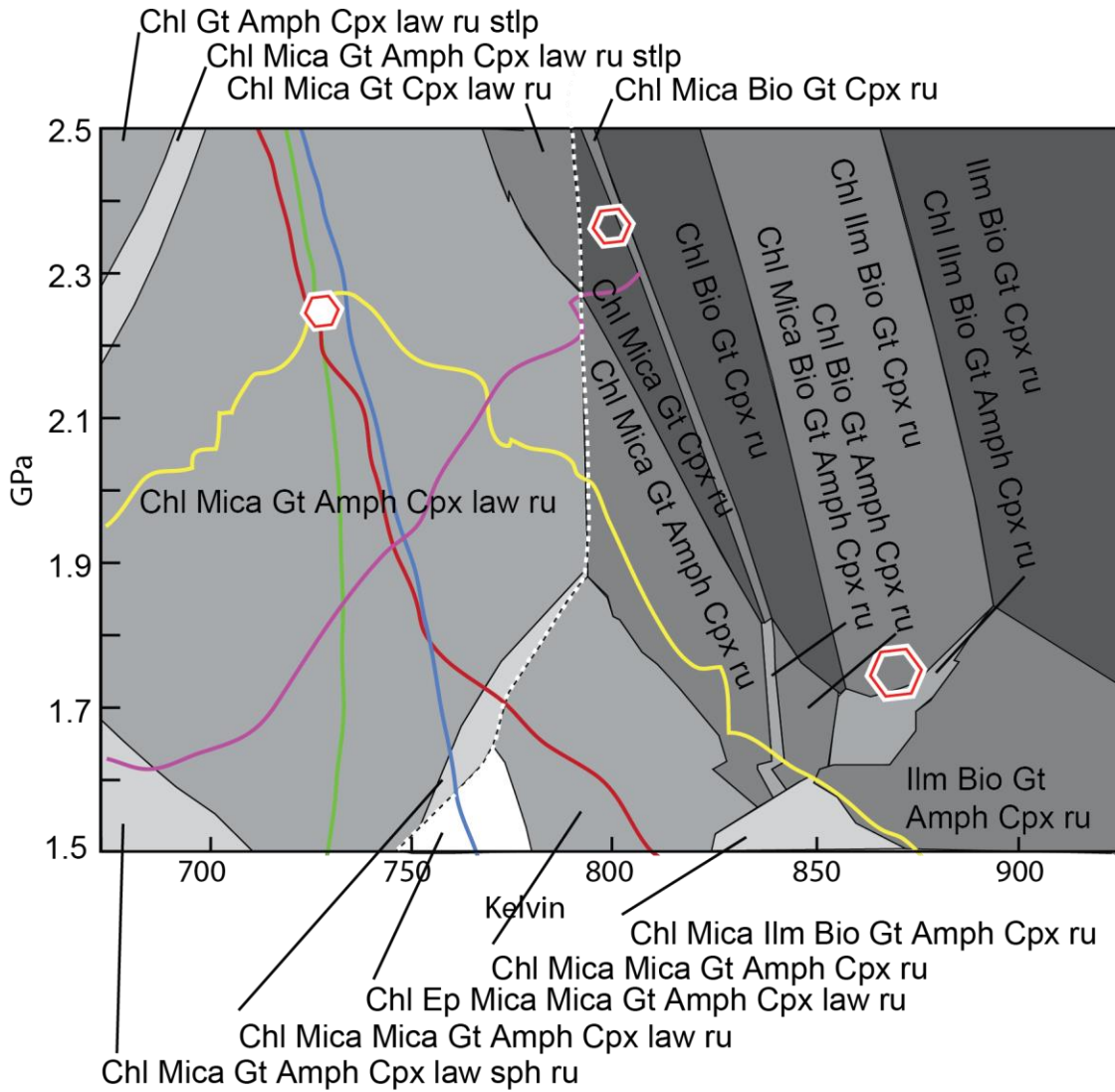


Figure A5: 06MSU-6E pseudosection for the WR with core intersection

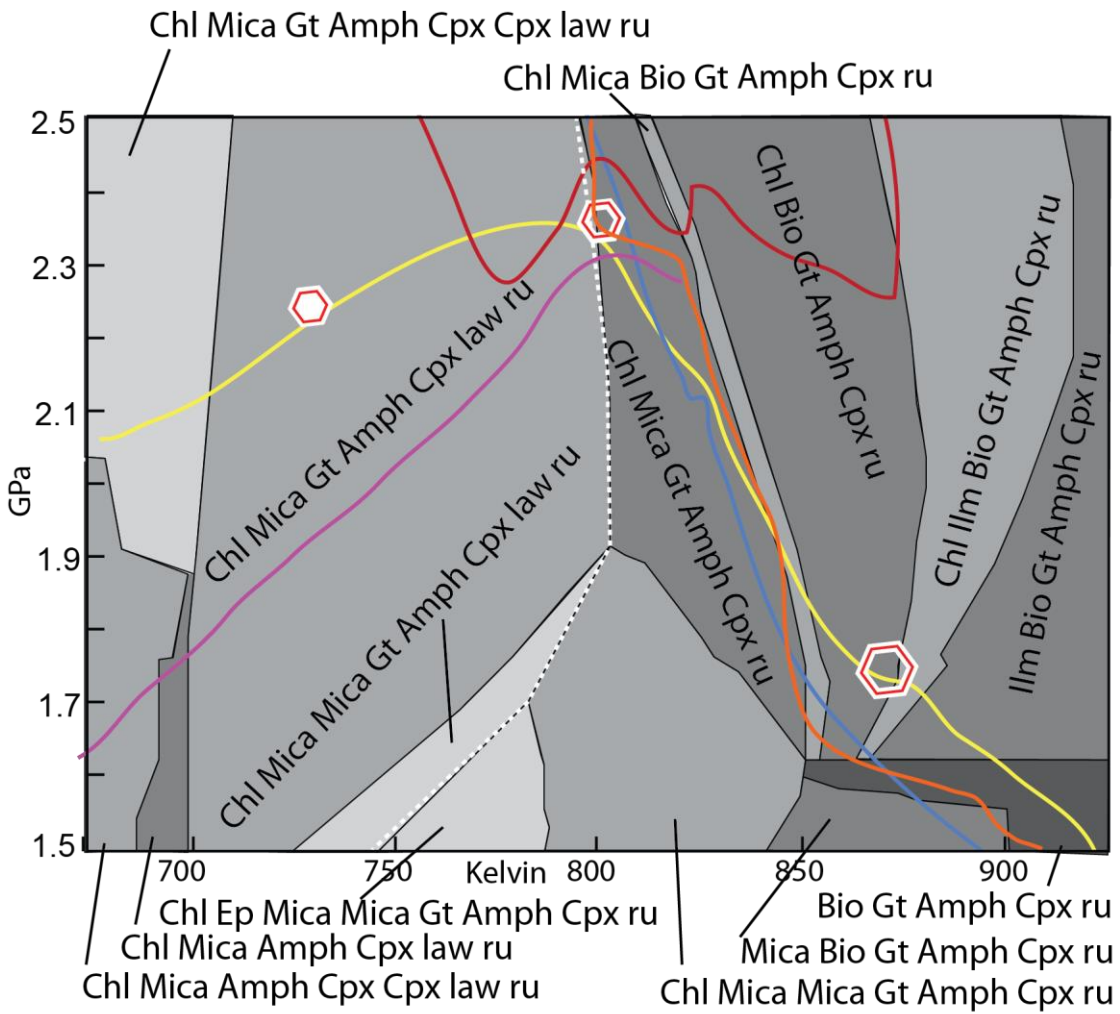


Figure A6: 06MSY-6E pseudosection for matrix with 86% garnet isopleths

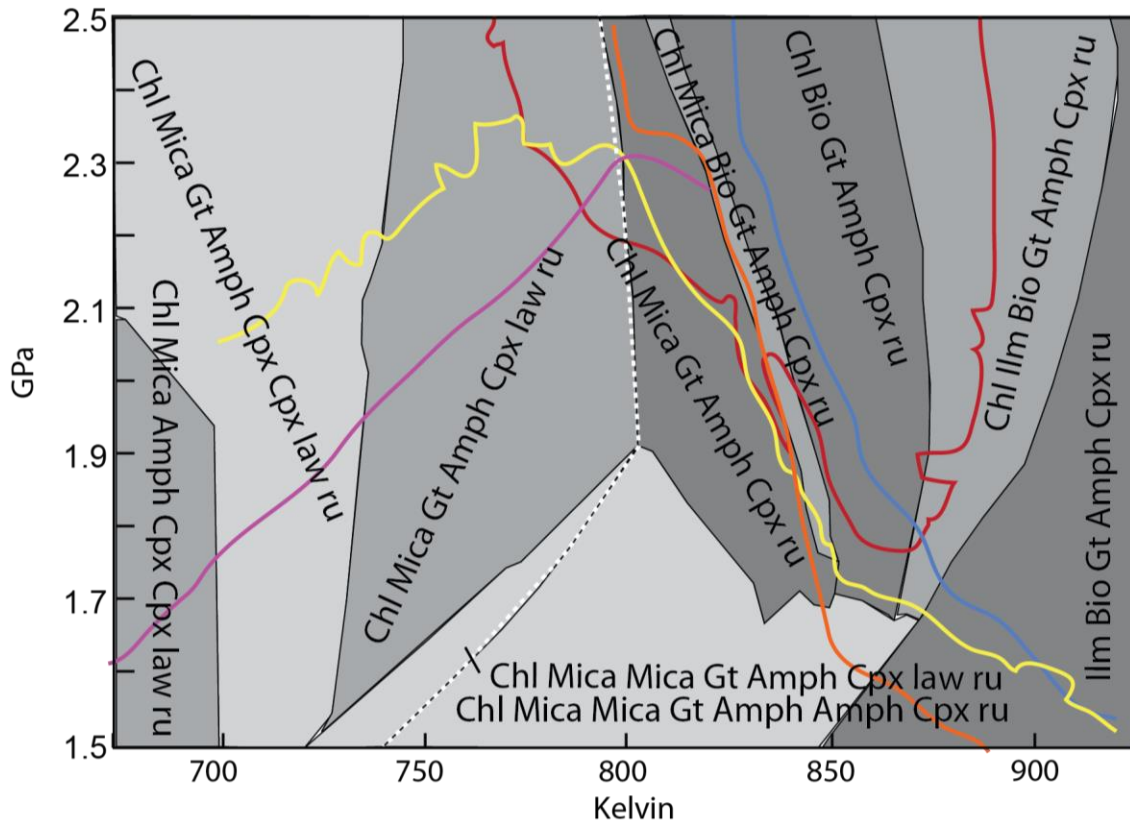


Figure A7: 06MSY-6E pseudosection for matrix with rim isopleths

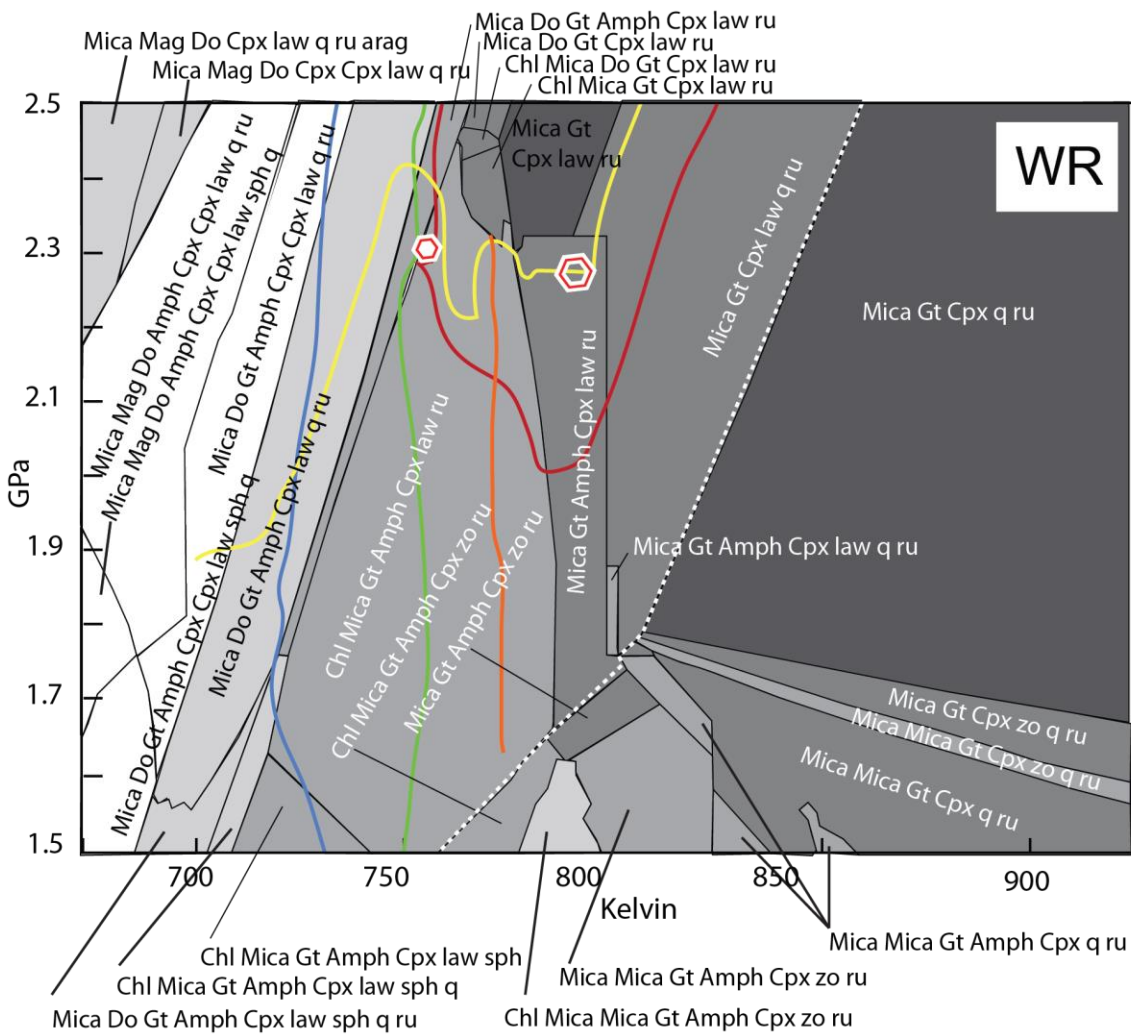


Figure A8:14BSY-37A pseudosection for WR with core isopleths

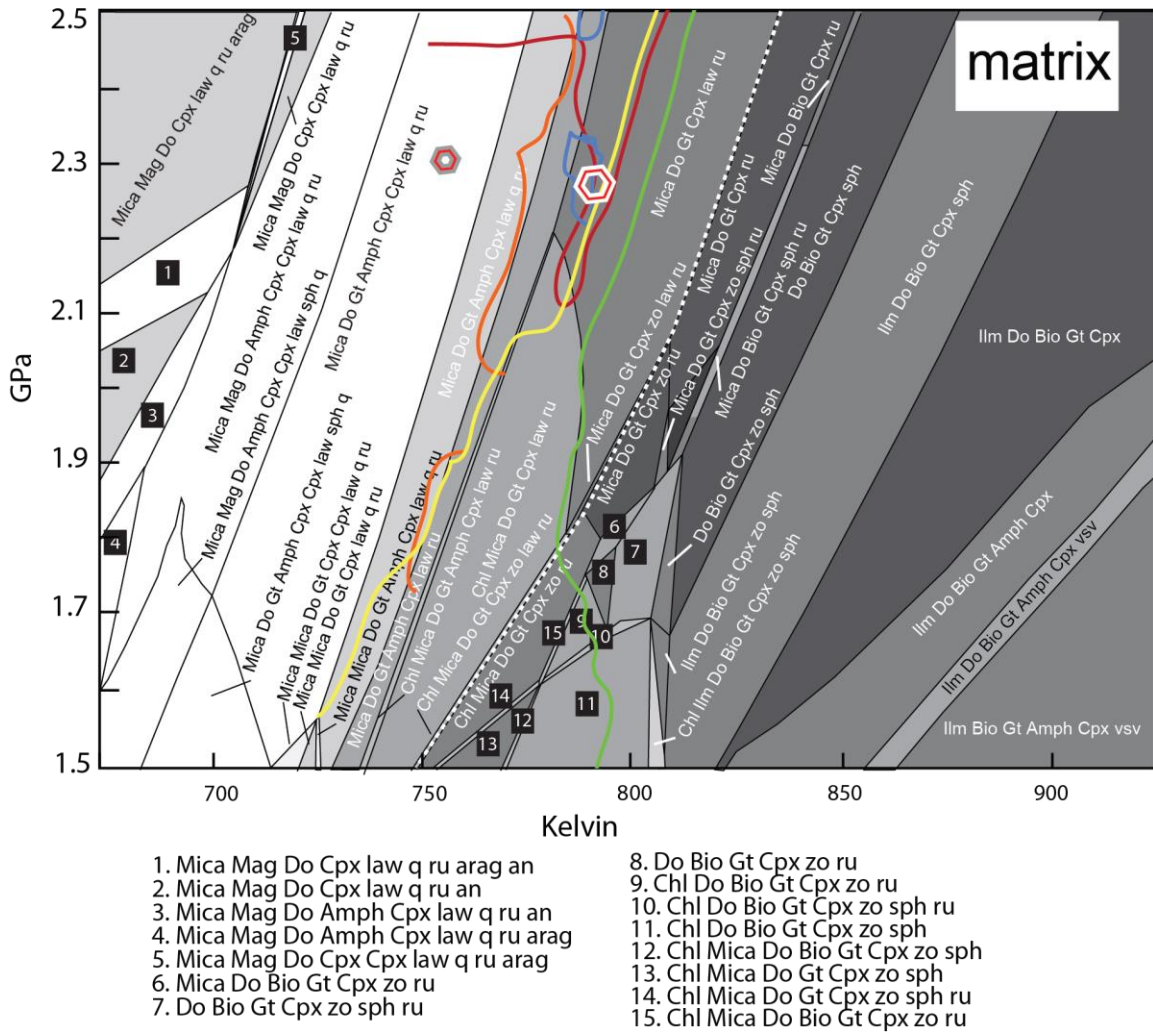
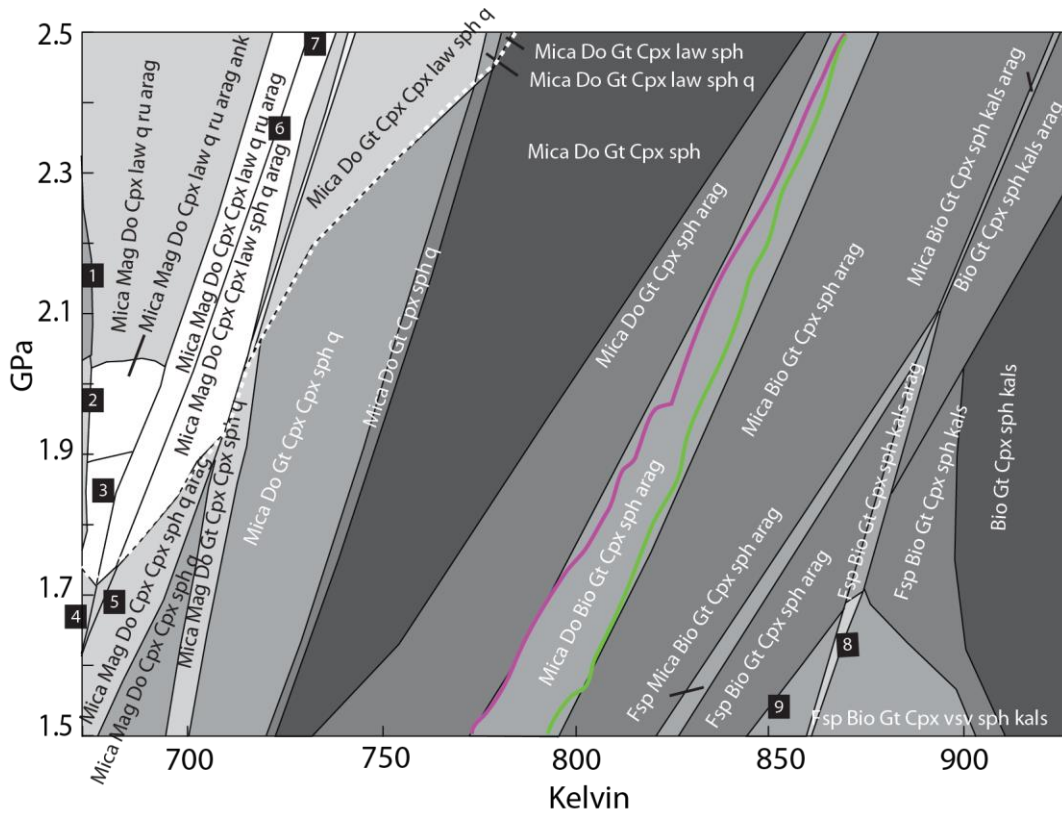


Figure A9: 14BSY-37A pseudosection for matrix with 90% garnet isopleths



- | | |
|---------------------------------------|-------------------------------------|
| 1. Mica Mag Do Cpx q ru arag | 6. Mica Mag Do Cpx Cpx law sph q |
| 2. Mica Mag Do Cpx q ru arag ank | 7. Mica Mag Do Gt Cpx Cpx law sph q |
| 3. Mica Mag Do Amph Cpx law q ru arag | 8. Fsp Bio Gt Cpx vsv sph kals arag |
| 4. Mica Mag Do Amph Cpx q ru arag | 9. Fsp Bio Gt Cpx vsv sph arag |
| 5. Mica Mag Do Cpx Cpx q ru arag | |

Figure A10: 14BSY-38A pseudosection for WR with rim isopleths. Only Si in mica (purple) and Mg in garnet (green) occur in this P-T-X space.

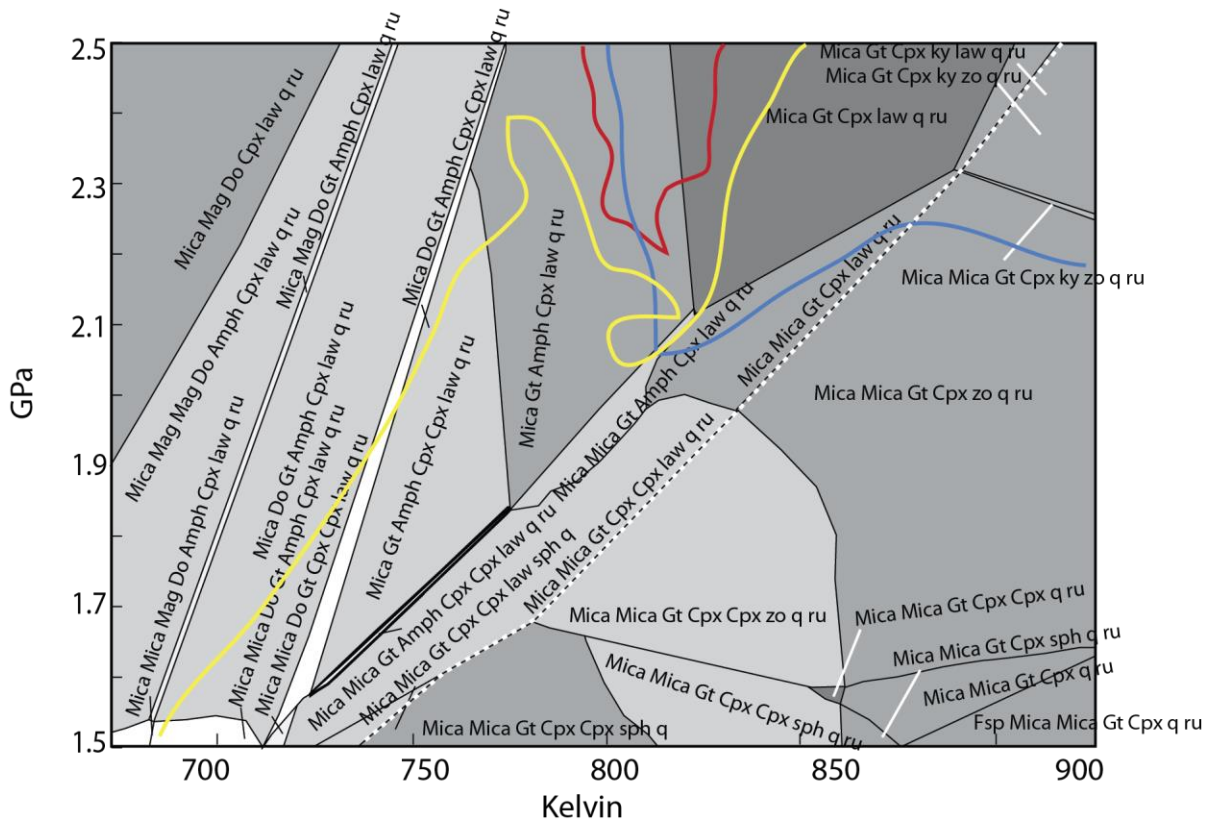


Figure A11: 14BSY-38A and 14BSY-38B combined pseudosection for WR with rim isopleths.

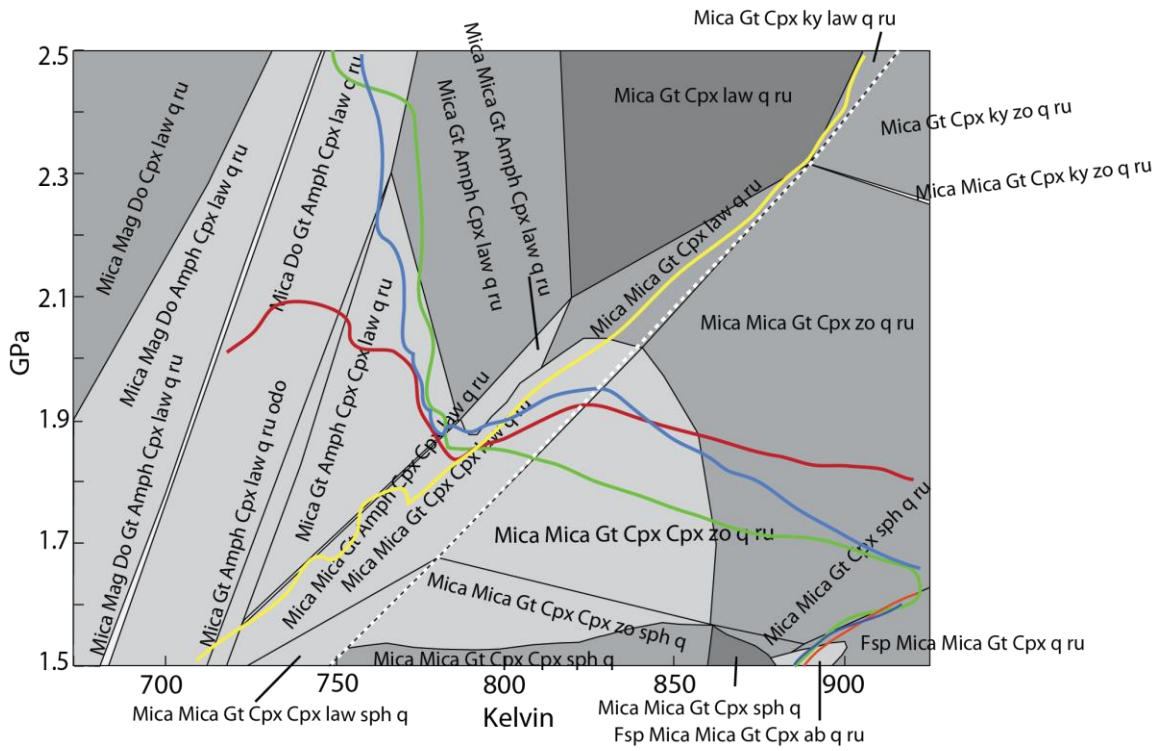


Figure A12: 14BSY-38A matrix and 14BSY-38B WR combined pseudosection with core isopleths

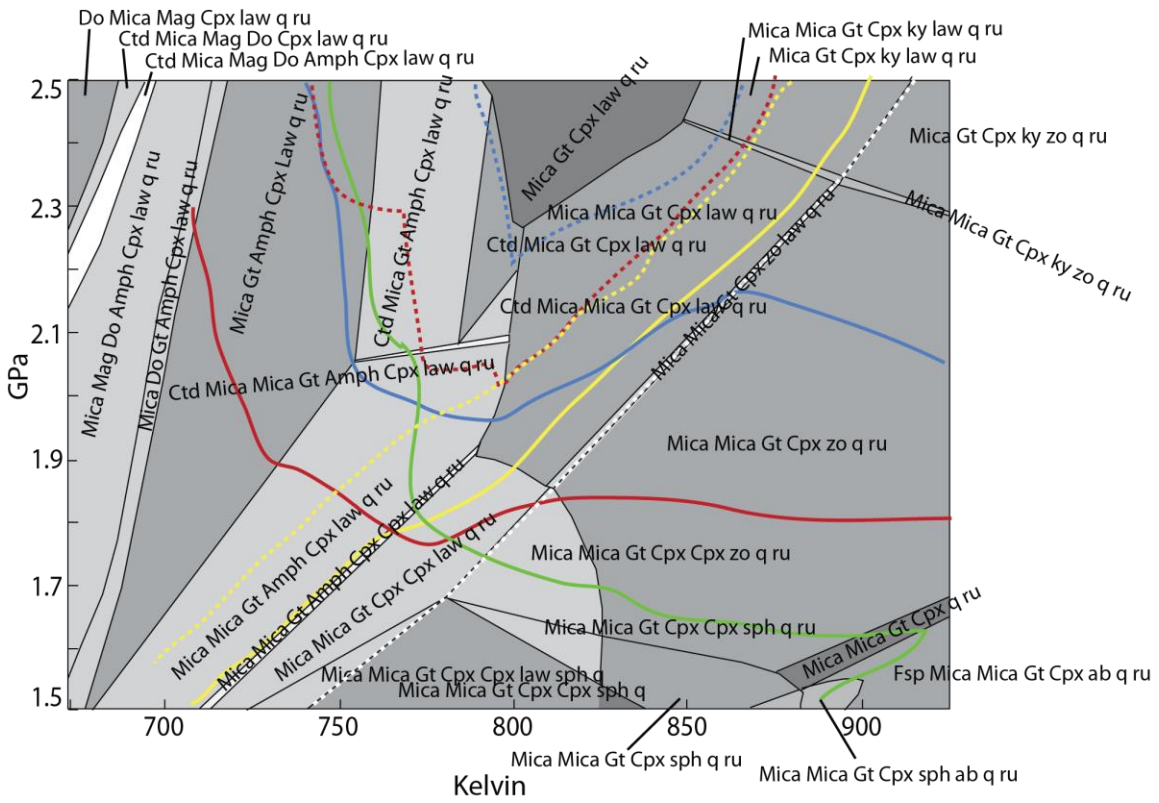


Figure A13 14BSY-38B WR pseudosection with rim isopleths (solid) and core isopleths (dashed).

10.6 APPENDIX F: MICRO-SAMPLING A SINGLE LARGE GARNET

A quartz-mica schist with large (~4 cm) garnet was sampled from the south of the island for zoned geochronology. The sample was taken from a coherent (for a subduction mélangé) layer about 2 m wide which cropped out over the entire Katergaki peninsula. The Katergaki peninsula is mapped by Keiter et al., (2011) as a metabasic unit which is to say, this small layer of quartz mica schist was not noted on the map. 14BSY-10A is a carbonate bearing mica schist with exceptionally large (~4 cm) garnet porphyroblasts. The schist is compositionally banded into quartz-rich and mica-rich layers on the scale of several centimeters. Three varieties of carbonate are present; a finer, partially broken-down calcite, a finer, partially broken-down magnesium carbonate, and a coarser, later calcite which has inclusions of mica and quartz. The rock is approximately 45% quartz, 20% mica, 15% calcite, 5% magnesite, and 15% garnet. Garnet, while strikingly large, is characterized by a “spider web” texture meaning that ~50% of the perceived garnet is, in fact, quartz. The garnet has minor inclusions of mica, carbonate, and rutile which appear to have some slight spiraled appearance. No explanation was determined for why garnets in this layer grew so large and with such a distinctive texture.

Zoned work was carried out on a slice cut from the rock which passed through the center of a large garnet. The slice was cut to 2.32 cm thick so as to ensure that a disk cut from the center of the garnet would be composed of only core material (Fig. A14). The ~2 cm slice was polished, carbon coated, and imaged on the SEM at Boston College. A backscatter electron map was made of the entire garnet. Individual spot analyses (n= 485) were taken with the SEM at points determined by hand by the user to avoid the frequent

quartz inclusions. Raw data from the SEM was treated as an element weight percent and converted to mole percent. Mole percent calcium in the garnet and mole percent Mn in the garnet were plotted on the SEM map using a color scale. Calcium increased towards the rims and Mn decreased towards the rim, indicating that this garnet had preserved its growth zonation. Core and rim regions were identified by using Mn and Ca concentrations as a guide. The core identified by element mapping was not at the geometric center of the garnet, highlighting the utility of this method but also presenting yet another strange aspect of this garnet's growth (Fig A15).

Cores and rims were drilled using the method in Dragovic (2013). Core and rim mass can be found in table A1. So much of the sample was, in fact, quartz, that enormous amounts of raw garnet annulus were needed to create enough crushed pure garnet for dating that the adjacent slice had to be drilled to supplement the core material from the original slice. A core powder and rim powder were reserved during crushing. A matrix was created by taking the material on either side of the drilled garnet.

Preliminary bulk garnet geochronology on the sample was moderately successful, giving an age of 44 ± 13 Ma (maximum $^{147}\text{Sm}/^{144}\text{Nd} = 0.8$, $n=6$, $\text{MSWD}=3.6$) (Table A4). Core and rim garnet geochronology, performed with the same laboratory procedures, was a failure. Both the core and rim garnet separate seemed to be not affected by the partial dissolution process at all. Their Nd concentrations remained high (4.9 and 3.7 ppm for the core and rim, respectively), suggesting that the samples were not cleansed of inclusions, despite losing 93% (core) and 89% (rim) of their starting mass during partial dissolution. The core achieved a $^{147}\text{Sm}/^{144}\text{Nd}$ of 0.18 while the rim reached

a $^{147}\text{Sm}/^{144}\text{Nd}$ of 0.14. Ages calculated from such low isotopic ratios are not valid. The reader may reference table A3 and figure A16 for these numbers.

What went wrong is still very much unresolved. The most obvious difference between the way the bulk garnet separates and the microdrilled separates were treated was the sample preparation, and not the clean lab dissolutions or columns. The drilled garnet slice was first polished with an aluminum suspension and subsequently carbon coated. While both the aluminum and carbon should have been removed by sonicating in isopropyl alcohol and wiping with a lint-free paper towel, it is possible that small amounts of these materials remained on the sample when it was crushed and sieved. Even so, it is not clear that these would be contaminants for $^{147}\text{Sm}/^{144}\text{Nd}$ work. Might small amounts of aluminum or carbon in cracks and crevices not removed by sonicating and wiping have protected the garnet from dissolution in hydrofluoric acid (which acts only on Si-O bonds); maybe hiding inclusions from the reach of the acid? Possibly, but the samples lost a substantial amount of mass in the full dissolution suggesting that dissolution was not inhibited. Another difference is the treatment with crystal bond and exposure to the drill bit. Could these have contaminated the sample? Crystal bond should be entirely removed by an acetone rinse followed by an isopropanol rinse. The glue can be seen by the eye and feels tacky to a gloved hand. No crystal bond remained on the sample after drilling. Could the drill bit have been contaminated? The volume of the drilled sample relative to the area of the sample that the drill bit directly touched makes this unlikely. The drill bit was new and used only for this sample. It is diamond-tipped so any material from the drill itself should have been separated from the garnet during magnetic separation. Might some contamination have occurred in lab? The blank run

with this sample was ~13 picograms of Nd, not enough to account for the 40 nanograms of Nd in the core separate or the 55 nanograms of Nd in the rim.

My best guess at this juncture is that maybe this particular drilled garnet was somehow different from the bulk separate at a sample level. Maybe when the bulk sample was crushed, magnetically-separated, and sieved I was able to take only the garnet that had a high magnetic susceptibility whereas when I performed the same procedure on the drilled sections I magnetically-separated more carefully due to sample size limitations and so went into the partial dissolution with a fundamentally different fraction of the garnet than I did in the bulk work. Maybe the most magnetically susceptible portions of garnets in this sample lack some particularly worrisome inclusions which have high Nd concentrations but low $^{147}\text{Sm}/^{144}\text{Nd}$ ratios and are found in the rest of the garnet.

Monazite fulfills the latter two criteria and monazite was seen in the matrix with microprobe analysis. However, because bulk geochronology had not shown any evidence for serious monazite contamination, and because it was not noted inside the garnet, no special considerations were taken to dissolve phosphate minerals during the partial dissolution of the drilled separates beyond the standard nitric acid dissolution. For monazite to somehow affect the microdrilled garnet to the extent seen here while barely affecting the bulk garnet is asking for fairly special conditions but it is in this author's opinion the most likely scenario of a host of unlikely scenarios.

Because of its large size, the sample has the potential to reveal the earliest stages of garnet growth on Syros. If this sample is deemed to be of interest in future studies, it should be re-run with an added step during the partial to dissolve phosphate phases such as what was done by Gatewood et al. (2015).

Table A3: sample preparation data for 14BSY-10A

		before crush	after crush		after frantz
		all size	140- 230	<230	140-230
10A slice 1	core	0.3143	0.1449	0.1362	0.0671
	rim	0.8664	0.3927		0.147
10A slice 2	core	0.4448	0.2339	0.1758	0.1111
				total core	0.1782

	$^{147}\text{Sm}/^{14}\text{Nd}$	$^{143}\text{Nd}/^{14}\text{Nd}$	$^{147}\text{Sm}/^{144}\text{Nd}$ error	$^{143}\text{Nd}/^{144}\text{Nd}$ error	ng Nd	ng Sm	ppm Nd	ppm Sm	minutes in HF	mg garnet to start	percent loss during partial	mesh size fraction
gt1	0.448287	0.512521	1.34E-04	1.04E-05	4.78365	3.54371	0.27273	0.20212	120	80	78	100-200
gt2	0.233506	0.512454	1.14E-05	4.89E-06	24.8162	9.57673	1.0269	0.39641	15	68	30	100-200
gt3	0.851038	0.512606	3.43E-04	2.88E-05	1.36714	1.92054	0.09507	0.13376	180	148	90	100-200
gt4	0.797635	0.512625	1.40E-04	2.97E-05	1.24797	1.64483	0.1214	0.16000	120	96.7	87	140-230
gt5	0.407446	0.512409	2.92E-04	4.58E-05	1.36246	0.90913	0.26979	0.18002	180	124.5	96	140-230
core	0.175262	0.512428	4.87E-05	4.23E-06	39.7184	11.5079	4.93396	1.42955	154	152	93	140-230
rim	0.141770	0.512423	8.89E-06	7.33E-06	55.453	12.9965	3.6651	0.85899	152	148	89	140-230
core pwd AQ1	0.144485	0.512418	5.58E-06	5.59E-06	25.6258	6.12096	6.42251	1.53407	-	-	-	-
rim pwd AQ1	0.131546	0.512411	1.60E-05	5.91E-06	16.6269	3.61584	8.61499	1.87349	-	-	-	-
matrix AQ1	0.131791	0.512410	1.37E-05	1.04E-05	7.65692	1.66823	16.9312	3.68886	-	-	-	-
WR XRF AQ1		Sm was on top of Nd...no	TIMS data from Sm run									
WR XRF AQ2	0.137946	0.51241	1.237E-05	1.123E-05	23.8932	5.44864	23.5756	5.37638	-	-	-	-

Table A4: Isotope data for 14BSY-10A

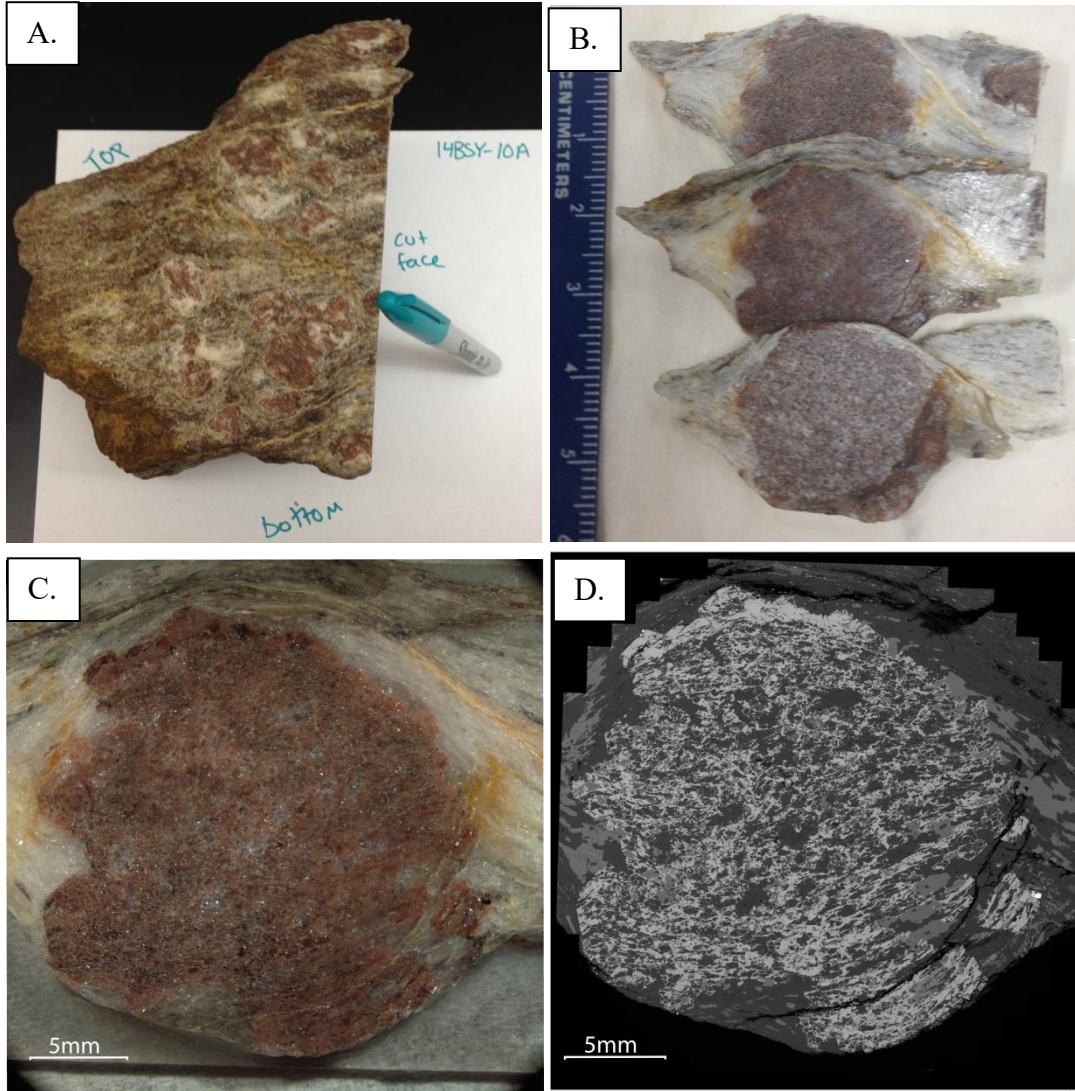


Figure A14: Sample preparation for microdrilling sample 14BSY-10A. A. Piece of sample 14BSY-10A showing large, anhedral garnets and mica and quartz layers. Drilled garnet is actually from a different chunk of the same material. B. Slices cut from the large garnet selected for microdrilling in an attempt to find the middle of the crystal. Center slice was chosen for microdrilling. C. Photograph of polished garnet slice. D. Backscatter electron image of garnet slice. Bright color is garnet, darker inclusions are almost entirely quartz. Note “spider web” texture.

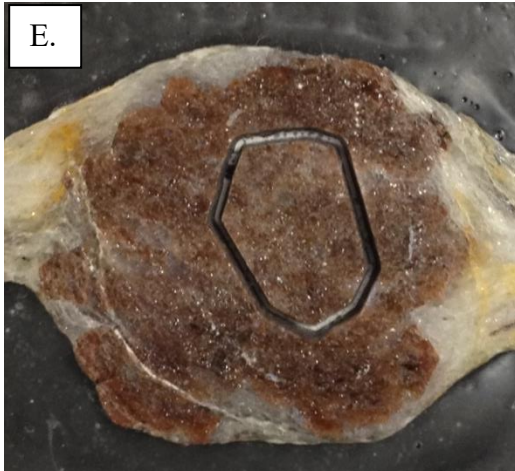
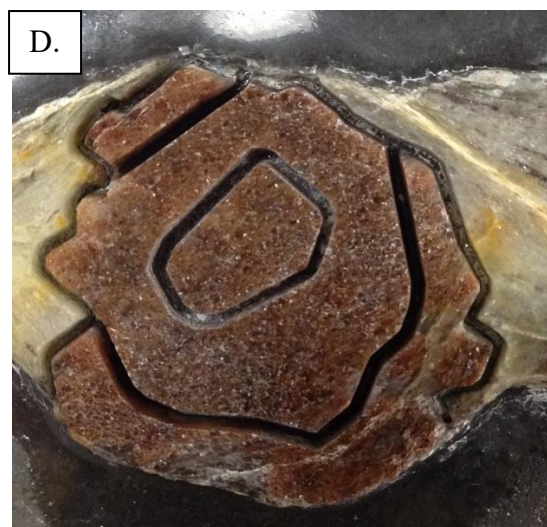
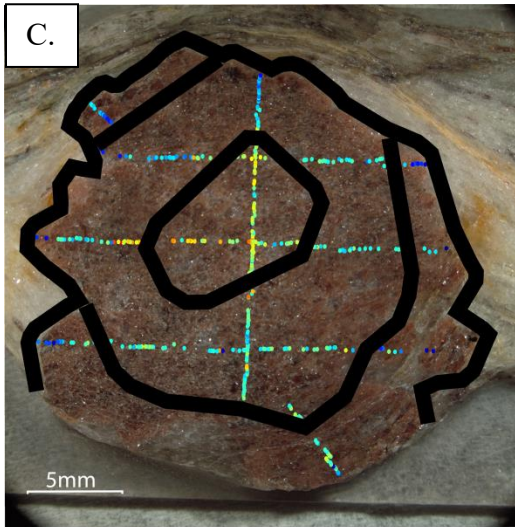
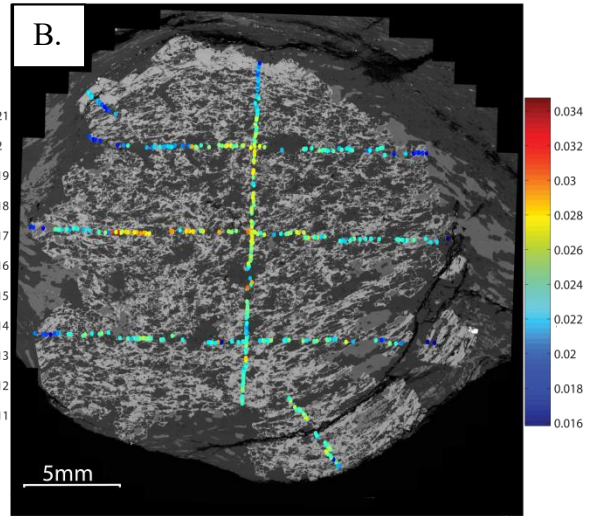
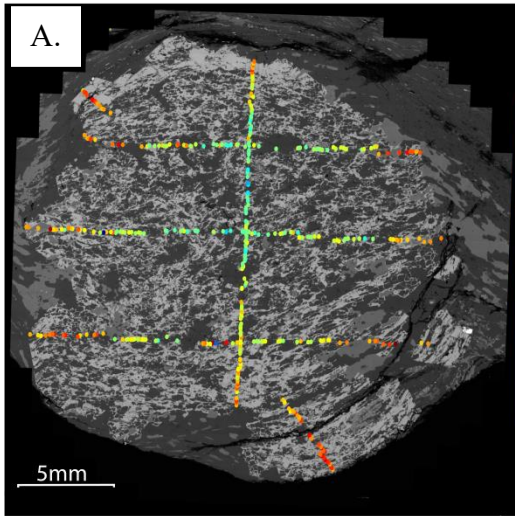


Figure A15: Single large garnet from sample 14BSY-10A as it was microdrilled. A. Moles Ca from spot analyses on the SEM overlaid on backscatter image. B. Moles Mn overlaid on backscatter image. C. Black lines are drill trench locations chosen based on Mn and Ca chemical data. D. Drill trenches separating core from rim and rim from matrix. E. Slice of garnet adjacent to primary slice. This secondary slice was not chemically analyzed but a core location was chosen based on the location of the core on the primary slice. This second core was drilled to supplement the small amount of garnet recovered from the first core after crushing, sieving and magnetic separation.

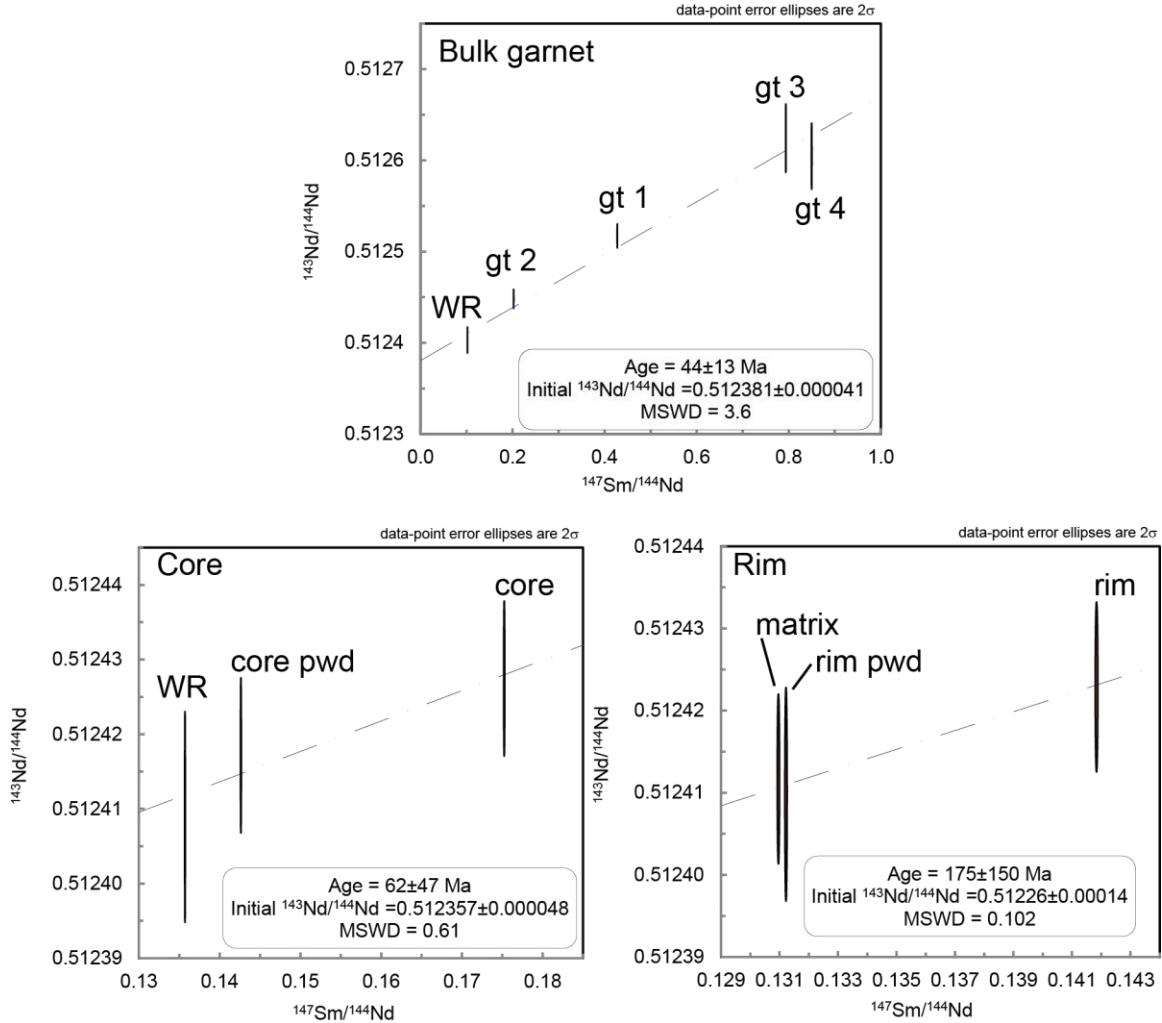


Figure A16: Isochrons for sample 14BSY-10A. Bulk garnet data gives mediocre precision. Core and rim isochrons do not yield interpretable age data. Core and rim garnet fractions were not cleaned during laboratory procedures.

11.0 REFERENCES

- Abers, G. a., van Keken, P. E., Kneller, E. A., Ferris, A., & Stachnik, J. C. (2006). The thermal structure of subduction zones constrained by seismic imaging: Implications for slab dehydration and wedge flow. *Earth and Planetary Science Letters*, 241(3-4), 387–397. <http://doi.org/10.1016/j.epsl.2005.11.055>
- Amato, J. M., Johnson, C. M., Baumgartner, L. P., & Beard, B. L. (1999). Rapid exhumation of the Zermatt-Saas ophiolite deduced from high-precision Sm-Nd and Rb-Sr geochronology. *Earth and Planetary Science Letters*, 171(3), 425–438. [http://doi.org/Doi 10.1016/S0012-821x\(99\)00161-2](http://doi.org/Doi 10.1016/S0012-821x(99)00161-2)
- Anczkiewicz, R. & Thirwall, M. F. (2003) Improving precision of Sm- Nd garnet dating by H₂SO₄ leaching: a simple solution to the phosphate inclusion problem. In Vance, D., Muller, W., & Villa, I. M. (eds) *Geochronology: Linking the isotopic record with petrology and textures*. Geological Society, London, Special Publications, 220, 83-91.
- Auzanneau E, Schmidt, M.W., Vielzeuf, D, Connolly, J.A.D. (2010) Titanium in phengite: a geobarometer for high temperature eclogites. *Contributions to Mineralogy And Petrology* **159**:1-24.
- Baxter, E. F., Ague, J. J., & Depaolo, D. J. (2002). Prograde temperature – time evolution in the Barrovian type – locality constrained by Sm / Nd garnet ages from Glen Clova, Scotland. *Journal of the Geological Society, London*, 159(1985), 71–82. <http://doi.org/10.1144/0016-76901013>
- Baxter, E. F., & Caddick, M. J. (2013). Garnet growth as a proxy for progressive subduction zone dehydration. *Geology*, 41(6), 643–646. <http://doi.org/10.1130/G34004.1>
- Baxter, E. F., & Scherer, E. E. (2013). Garnet Geochronology: Timekeeper of Tectonometamorphic Processes. *Elements*, 9(6), 433–438. <http://doi.org/10.2113/gselements.9.6.433>

- Bebout, G. E., & Barton, M. D. (1989). Fluid flow and metasomatism in a subduction zone hydrothermal system: Catalina Schist terrane, California. *Geology*, 17, 976–980.
- Berman, R.G. (1991) Thermobarometry using multi-equilibrium calculations: a new technique, with petrological applications; in, *Quantitative methods in petrology: an issue in honor of Hugh J. Greenwood*; Eds. Gordon, T M; Martin, R F. *Canadian Mineralogist* v. 29, 833-855.
- Bloch, E., Ganguly, J., Hervig, R. Cheng, W. (2015) 176Lu-176Hf geochronology of garnet I: experimental determination of the diffusion kinetics of Lu³⁺ and Hf⁴⁺ in garnet, closure temperatures and geochronological implications. *Contributions to Mineralogy and Petrology* 169:12 doi: 10.1007/s00410-015-1109-8.
- Breeding, C.M., Ague, J.J., Bröcker, M., & Bolton, E.W.,(2003), Blueschist preservation in a retrograded, high-pressure, low-temperature metamorphic terrane, Tinos, Greece: Implications for fluid flow paths in subduction zones: *Geochemistry Geophysics Geosystems*, v. 4, no. 1, doi: 10.1029/2002GC000380.
- Bröcker, M., Baldwin, S., & Arkudas, R. (2013). The geological significance of ⁴⁰Ar/³⁹Ar and Rb-Sr white mica ages from Syros and Sifnos, Greece: a record of continuous (re)crystallization during exhumation? *Journal of Metamorphic Geology*, 31(6), 629–646. <http://doi.org/10.1111/jmg.12037>
- Bröcker, M., & Enders, M. (1999). U–Pb zircon geochronology of unusual eclogite-facies rocks from Syros and Tinos (Cyclades, Greece). *Geological Magazine*, 136(2), 111–118. <http://doi.org/10.1017/S0016756899002320>
- Bröcker, M., & Enders, M. (2001). Unusual bulk-rock compositions in eclogite-facies rocks from Syros and Tinos (Cyclades , Greece) : implications for U – Pb zircon geochronology. *Chemical Geology*, (175), 581–603.
- Bröcker, M., & Keasling, A. (2006). Ionprobe U-Pb zircon ages from the high-pressure/low-temperature mélange of Syros, Greece: age diversity and the importance of pre-Eocene subduction. *Journal of Metamorphic Geology*, 24(7), 615–631.
- Carlson, W.D., Pattison, D. R. M., & Caddick, M. J. (2015) Beyond the equilibrium paradigm: How consideration of kinetics enhances metamorphic interpretation. *American Mineralogist*, 100, 1659-1667. doi: <http://dx.doi.org/10.2138/am-2015-5097>.
- Cheng, H. & Cao, D. (2015) Protracted garnet growth in high-P eclogite: constraints from multiple geochronology and P-T pseudosection. *Journal of Metamorphic geology*, 33, 613-632. doi:10.1111/jmg.12136

- Connolly, J. A. D. (1990) Multivariable phase diagrams: an algorithm based on generalized thermodynamics. *American Journal of Science*, 290(6), 666–718. <http://doi.org/10.2475/ajs.290.6.666>
- Connolly, J.A.D (2009) The geodynamic equation of state: what and how. *Geochemistry, Geophysics, Geosystems* 10:Q10014
DOI:10.1029/2009GC002540.
- Coggon R, Holland, T.J.B. (2002) Mixing properties of phengitic micas and revised garnet-phengite thermobarometers. *Journal of Metamorphic Geology* 20:683-96.
- Davis, P. B., & Whitney, D. L. (2006). Petrogenesis of lawsonite and epidote eclogite and blueschist, Sivrihisar Massif, Turkey. *Journal of Metamorphic Geology*, 24, 823–849. <http://doi.org/10.1111/j.1525-1314.2006.00671.x>
- Davis, P. B., & Whitney, D. L. (2008). Petrogenesis and structural petrology of high-pressure metabasalt pods, Sivrihisar, Turkey. *Contributions to Mineralogy and Petrology*, 156(2), 217–241. <http://doi.org/10.1007/s00410-008-0282-4>
- Dewolf, C. P., Zeissler, C. J., Halliday, a. N., Mezger, K., & Essene, E. J. (1996). The role of inclusions in U-Pb and Sm-Nd garnet geochronology: Step wise dissolution experiments and trace uranium mapping by fission track analysis. *Geochimica et Cosmochimica Acta*, 60(1), 121–134. [http://doi.org/10.1016/0016-7037\(95\)00367-3](http://doi.org/10.1016/0016-7037(95)00367-3)
- Diener, J. F. A. & Powell, R. (2012) Revised activity-composition models for clinopyroxene and amphibole. *Journal of Metamorphic Geology*, 30, 131-142. doi:10.1111/j.1525-1314.2011.00959.x
- Diener, J. F. A., Powell, R., White, R. W., & Holland, T. J. B. (2007) A new thermodynamic model for clino- and orthoamphiboles in the system Na₂O-CaO-FeO-MgO-Al₂O₃-SiO₂-H₂O-O. *Journal of Metamorphic Geology*, 25, 631-656.
- Dragovic, B. (2013). Constraining the rates and timescales of garnet growth and associated dehydration during metamorphism. Doctoral Dissertation, Boston University.
- Dragovic, B., Baxter, E. F., & Caddick, M. J. (2015). Pulsed dehydration and garnet growth during subduction revealed by zoned garnet geochronology and thermodynamic modeling, Sifnos, Greece. *Earth and Planetary Science Letters*, 413, 111–122. <http://doi.org/10.1016/j.epsl.2014.12.024>
- Dragovic, B., Samanta, L. M., Baxter, E. F., & Selverstone, J. (2012). Using garnet to constrain the duration and rate of water-releasing metamorphic reactions during subduction: An example from Sifnos, Greece. *Chemical Geology*, 314-317, 9–22. <http://doi.org/10.1016/j.chemgeo.2012.04.016>

- Ellis, D.J., & Green, D.H., (1979), An experimental study of the effect of Ca upon garnet-clinopyroxene Fe-Mg exchange equilibria, *Contributions to Mineralogy and Petrology*, v. 71, no. 1, p. 13-22 doi: 10.1007/BF00371878
- Faure, G. & Mensing, T. (2005). *Isotopes: Principles and Applications*. John Wiley and Sons, Hoboken, NJ. 897 pp.
- Fuhrman, M. L. & Lindsley, D. H. (1988) Ternary-feldspar modeling and thermometry, *American Mineralogist* 73, 201-215.
- Früh-Green, G. L., Scambelluri, M., & Vallis, F. (2004). O–H isotope ratios of high pressure ultramafic rocks: implications for fluid sources and mobility in the subducted hydrous mantle. *Contributions to Mineralogy and Petrology*, 141(2), 145–159. <http://doi.org/10.1007/s004100000228>
- Gatewood, M. P., Dragovic, B, Stowell, H. H., Baxter, E. F., Hirsch, D. M., & Bloom, R.(2015) Evaluating chemical equilibrium in metamorphic rocks using major element and Sm-Nd isotopic age zoning in garnet, Townshend Dam, Vermont, USA, *Chemical Geology* 401, 151-168. doi: <http://dx.doi.org/10.1016/j.chemgeo.2015.02017>
- Gitahi, N. (2004), Geochemistry and metamorphic evolution of eclogites on Syros island, Greece, paper presented at Seventeenth Annual Keck Research Symposium in Geology, Keck Geol. Consortium, Lexington, Va.
- Green, T.H., & Hellman, P.L., (1982), Fe-Mg partitioning between coexisting garnet and phengite at high pressure, and comments on a garnet-phengite geothermometer: *LITHOS*. V. 15 p. 253-266
- Green, E.C.R., Holland, T.J. B., and Powell, R. (2007). An order-disorder model for omphacitic pyroxenes in the system jadeite-diopside-hedenbergite-acmite, with applications to eclogitic rocks. *American Mineralogist*, 92. 1181-1189.
- Hacker, B. R. (2008). H₂O subduction beyond arcs. *Geochemistry, Geophysics, Geosystems*, 9(3), n/a–n/a. <http://doi.org/10.1029/2007GC001707>
- Hacker, Bradley R.; Peacock, Simon M.; Abers, Geoffrey A; & Holloway, S. D. (2003). Subduction factory 2. Are intermediate-depth earthquakes in subducting slabs linked to metamorphic dehydration reactions? *Journal of Geophysical Research*, 108(B1), 2030. <http://doi.org/10.1029/2001JB001129>
- Halama, R., John, T., Herms, P., Hauff, F., & Schenk, V. (2011). A stable (Li, O) and radiogenic (Sr, Nd) isotope perspective on metasomatic processes in a subducting slab. *Chemical Geology*, 281(3-4), 151–166. <http://doi.org/10.1016/j.chemgeo.2010.12.001>

- Harvey, J., & Baxter, E. F. (2009). An improved method for TIMS high precision neodymium isotope analysis of very small aliquots (1-10^{??}ng). *Chemical Geology*, 258(3-4), 251–257. <http://doi.org/10.1016/j.chemgeo.2008.10.024>
- Holland, T., Baker, J., & Powell, R. (1998) Mixing properties and activity-composition relationships of chlorites in the system MgO-FeO-Al₂O₃-SiO₂-H₂O. *European Journal of Mineralogy* 10, 395-406 doi: 10.1127/ejm/10/3/0395
- Holland, T., & Powell, R. (1998). An internally consistent thermodynamic dataset for phases of petrologic interest. *J. Metamorph. Geol.* 16, 309–343.
- Holland, T. & Powell, R., (2003) Activity-composition relations for phases in petrological calculations: an asymmetric multicomponent formulation. *Contributions to Mineralogy and Petrology*. 145, 492-501. doi:10.1007/s00410-003-0464-z
- Holley, E. A., T. Ross, & J. T. Cheney (2004), Pressure-temperature conditions of metamorphism in eclogites, Syros, Greece, paper presented at Seventeenth Annual Keck Research Symposium in Geology, Keck Geol. Consortium, Lexington, Va.
- Jedlicka, R. Faryad, S. W., & Hauzenberger, C. (2015) Prograde metamorphic history of UHP granulites from the Moldanubian Zone (Bohemian Massif) revealed by major element and Y + REE zoning in garnets. *Journal of Petrology*. 56 (10), 2069-2088. doi:10.1093/petrology/egv066
- Keiter, M., Ballhaus, C., & Tomascheck, F. (2011). A new geological map of the island of Syros (Aegean Sea, Greece): Implications for lithostratigraphy and structural history of the Cycladic Blueschist Unit. *Geological Society of America Special Paper*, 481, 400.
- Kelemen, P. B., & Manning, C. E. (2015). Reevaluating carbon fluxes in subduction zones, what goes down, mostly comes up. *Proceedings of the National Academy of Sciences*, 112(30), E3997–E4006. <http://doi.org/10.1073/pnas.1507889112>
- Konrad-Schmolke, M., Handy, & M.R., Babist, J. (2005) Thermodynamic modeling of diffusion-controlled garnet growth. *Contrib Mineral Petrol* 149: 181. doi:10.1007/s00410-004-0643-6
- Konrad-Schmolke, M., O'Brien, P. J., & Zack, T. (2011). Fluid Migration above a Subducted Slab--Constraints on Amount, Pathways and Major Element Mobility from Partially Overprinted Eclogite-facies Rocks (Sesia Zone, Western Alps). *Journal of Petrology*, 52(3), 457–486. <http://doi.org/10.1093/petrology/egq087>
- Lagos, M., Scherer, E., Tomaschek, F., Munker, C., Keiter, M., Berndt, J., & Ballhaus, C. (2007). High precision Lu–Hf geochronology of Eocene eclogite-facies rocks

- from Syros, Cyclades, Greece. *Chemical Geology*, 243(1-2), 16–35.
<http://doi.org/10.1016/j.chemgeo.2007.04.008>
- Lister, G. S. and Forster, M. A. (2016), White mica $^{40}\text{Ar}/^{39}\text{Ar}$ age spectra and the timing of multiple episodes of high-*P* metamorphic mineral growth in the Cycladic eclogite–blueschist belt, Syros, Aegean Sea, Greece. *J. Metamorph. Geol.*, 34: 401–421. doi:10.1111/jmg.12178
- Ludwig, K.R. (2008) User's manual for Isoplot 3.70. Berkeley Geochronology Center Special Publication no. 4, Berkeley.
- Maluski, H., Bonneau, M., Kienast, J.R., (1987). Dating the metamorphic events in the Cycladic area: $^{40}\text{Ar}/^{39}\text{Ar}$ data from metamorphic rocks of the island of Syros (Greece). *Bull. Soc. Ge'ol. Fr. III* (8), 833– 841.
- Marmo, B. A., Clarke, G. L. and Powell, R. (2002), Fractionation of bulk rock composition due to porphyroblast growth: effects on eclogite facies mineral equilibria, Pam Peninsula, New Caledonia. *Journal of Metamorphic Geology*, 20: 151–165. doi:10.1046/j.0263-4929.2001.00346.x
- Marschall, H. R., Altherr, R., Gméling, K., & Kasztovszky, Z. (2008). Lithium, boron and chlorine as tracers for metasomatism in high-pressure metamorphic rocks: a case study from Syros (Greece). *Mineralogy and Petrology*, 95(3-4), 291–302.
<http://doi.org/10.1007/s00710-008-0032-3>
- Marschall, H. R., Ludwig, T., Altherr, R., Kalt, A., & Tonarini, S. (2006). Syros Metasomatic Tourmaline: Evidence for Very High- P Fluids in Subduction Zones. *Journal of Petrology*, 47(10), 1915–1942.
<http://doi.org/10.1093/petrology/egl031>
- Massonne, HJ and Schreyer, W., (1989) Stability field of the high-pressure assemblage talc phengite and two new phengite barometers, *European Journal of Mineralogy* v. 1, no. 3, p. 391-410
- Mulcahy, S. R., Vervoort, J.D., Renne, P.R. (2014) Dating subduction zone metamorphism with combined garnet and lawsonite Lu-Hf geochronology. *Journal of Metamorphic Geology*, 32(5), 515-533.
- Moore, S. J., Carlson, W. D. and Hesse, M. A. (2013) Origins of yttrium and rare earth element distributions in metamorphic garnet. *Journal of Metamorphic Geology*, 31, 663-689. doi:10.1111/jmg.12039.
- Okrusch, M., and Bröcker, M., (1990) Eclogites associated with high-grade blueschists in the Cyclades archipelago, Greece: a review: *European Journal of Mineralogy* v. 2 p. 451-478 doi: 10.1127/ejm/2/4/0451
- Philippon, M. Brun, J., Gueydan, F. (2012) Deciphering subduction from exhumation in

the segmented Cycladic Blueschist Unit (Central Aegean, Greece).
Tectonophysics 524-525 116-134. doi:10.1016/j.tecto.2011.12.025

- Philippon, M., Gueydan, F., Pitra, P., and Brun, J-P., 2013, Preservation of subduction-related prograde deformation in lawsonite pseudomorph-bearing rocks: *Journal of Metamorphic Geology*, v. 31, no. 5, p. 571–583, doi: 10.1111/jmg.12035.
- Pollington, A. D., & Baxter, E. F. (2010). High resolution Sm–Nd garnet geochronology reveals the uneven pace of tectonometamorphic processes. *Earth and Planetary Science Letters*, 293(1-2), 63–71. <http://doi.org/10.1016/j.epsl.2010.02.019>
- Pollington, A. D., & Baxter, E. F. (2011). High precision microsampling and preparation of zoned garnet porphyroblasts for Sm-Nd geochronology. *Chemical Geology*, 281(3-4), 270–282. <http://doi.org/10.1016/j.chemgeo.2010.12.014>
- Powell, R. and Holland, T. (1999) Relating formulations of the thermodynamics of mineral solid solutions: Activity modeling of pyroxenes, amphiboles, and micas. *American Mineralogist*. 84 (1-2), 1-14.
- Putlitz, B., Cosca, M. a., & Schumacher, J. C. (2005). Prograde mica ⁴⁰Ar/³⁹Ar growth ages recorded in high pressure rocks (Syros, Cyclades, Greece). *Chemical Geology*, 214(1-2), 79–98. <http://doi.org/10.1016/j.chemgeo.2004.08.056>
- Ramos, E. (2015) Garnet growth as a tracer of subduction zone dehydration: a case study from the Cycladic Blueschist Unit in Syros, Greece. Senior Undergraduate Thesis, Boston University.
- Ravna, E.J., and Terry, M.P., (2004), Geothermobarometry of UHP and HP eclogites and schists - an evaluation of equilibria among garnet-clinopyroxene-kyanite-phengite-coesite/quartz: *Journal of Metamorphic Geology*, v. 22, no. 6, p. 579–592, doi: 10.1111/j.1525-1314.2004.00534.x.
- Rubatto, D. (2002) Zircon trace element geochemistry: partitioning with garnet and the link between U-Pb ages and metamorphism. *Chemical Geology*, 184(1-2), 123-138.
- Scherer, E. E., Cameron, K. L., & Blichert-Toft, J. (2000). Lu-Hf garnet geochronology: Closure temperature relative to the Sm-Nd system and the effects of trace mineral inclusions. *Geochimica et Cosmochimica Acta*, 64(19), 3413–3432. [http://doi.org/10.1016/S0016-7037\(00\)00440-3](http://doi.org/10.1016/S0016-7037(00)00440-3)
- Schmadicke, E., and Will, T.M.,(2003), Pressure-temperature evolution of blueschist facies rocks from Sifnos, Greece, and implications for the exhumation of high-pressure rocks in the Central Aegean: *Journal of Metamorphic Geology*, v. 21, no. 8, p. 799–811, doi: 10.1046/j.1525-1314.2003.00482.x.

- Schmidt, M. W., & Poli, S. (1998). Experimentally based water budgets for dehydrating slabs and consequences for arc magma generation. *Earth and Planetary Science Letters*, 163(1-4), 361–379. [http://doi.org/10.1016/S0012-821X\(98\)00142-3](http://doi.org/10.1016/S0012-821X(98)00142-3)
- Schumacher, J. C., Brady, J. B., Cheney, J. T., & Tonnsen, R. R. (2008). Glaucophane-bearing Marbles on Syros, Greece. *Journal of Petrology*, 49(9), 1667–1686. <http://doi.org/10.1093/petrology/egn042>
- Spandler, C., Pettke, T., and Rubatto, D. (2011) Internal and external fluid sources for eclogite-facies veins in the Monviso Meta-ophiolite Western Alps: Implications for fluid flow in subduction zones. *Journal of Petrology*. 52(6) 1207-1236. doi:10.1093/petrology/egr025.
- Spandler, C., & Hermann, J. (2006). High-pressure veins in eclogite from New Caledonia and their significance for fluid migration in subduction zones. *Lithos*, 89, 135–153. <http://doi.org/10.1016/j.lithos.2005.12.003>
- Spear, F. S., Thomas, J. B., Hallet, B. W. (2014) Overstepping the garnet isograd: a comparison of QuiG barometry and thermodynamic modeling. *Contributions to Mineralogy and Petrology*. 168(3) doi:10.1007/s00410-014-1059-6
- Stewart, E. (2015) Microstructural and tectonic applications of texturally controlled Sm/Nd garnet geochronology, Master's Thesis, Order No. 1603518 Boston University, 2015.
- Sun, C., and Liang, Y., 2015, A REE-in-garnet-clinopyroxene thermobarometer for eclogites, granulites and garnet peridotites: *Chemical Geology*, v. 393-394, no. C, p. 79–92, doi: 10.1016/j.chemgeo.2014.11.014.
- Tatsumi, Y. (1986). Formation of the volcanic front in subduction zones. *Geophysical Research Letters*, 12(8), 717–720.
- Tomaschek, F., Kennedy, A. K., Villa, I. M., Lagos, M., Ballhaus, C. (2003). Zircons from Syros, Cyclades, Greece--Recrystallization and Mobilization of Zircon During High-Pressure Metamorphism. *Journal of Petrology*, 44(11), 1977–2002. <http://doi.org/10.1093/petrology/egg067>
- Trotet, F., Jolivet, L., & Vidal, O. (2001 a). Tectono-metamorphic evolution of Syros and Sifnos islands (Cyclades, Greece). *Tectonophysics*, 338, 179–206.
- Trotet, F., Vidal, O., and Jolivet, L., (2001 b), Exhumation of Syros and Sifnos metamorphic rocks (Cyclades, Greece). New constraints on the PT paths: *European Journal* v. 13 p. 901-920 doi: 10.1127/0935-1221/2001/0013/0901.
- van Breemen, O., & Hawkesworth, C. J. (1980). Sm-Nd isotopic study of garnets and their metamorphic host rocks. *Earth and Environmental Science Transactions of*

the Royal Society of Edinburgh, 71(02), 97–102.
<http://doi.org/10.1017/S0263593300013535>

- van Keken, P. E., Hacker, B. R., Syracuse, E. M., & Abers, G. a. (2011). Subduction factory: 4. Depth-dependent flux of H₂O from subducting slabs worldwide. *Journal of Geophysical Research*, 116(B1), B01401.
<http://doi.org/10.1029/2010JB007922>
- Wendt, I., & Carl, C. (1991). The statistical distribution of the mean squared weighted deviation. *Chemical Geology*, 86, 275–285. [http://doi.org/10.1016/S0009-2541\(10\)80009-9](http://doi.org/10.1016/S0009-2541(10)80009-9)
- White, R. Pomroy, N.E., Powell, R. (2005) An in situ metatextite transition in upper amphibolite facies rocks from Broken Hill, Australia. *Journal of Metamorphic Geology*. 23 (7), 579-602.
- White, R.W., Powell, R., Clarke, G.L. (2002) The interpretation of reaction textures in Fe-rich metapelitic granulites of the Musgrave Block, central Australia: constraints from mineral equilibria calculations in the system K₂O-FeO-MgO-Al₂O₃-SiO₂-H₂O-TiO₂-Fe₂O₃. *Journal of Metamorphic Geology*. 20 (1), 41-55. doi:10.1046/j.0263-4929.2001.00349.x
- White RW, Powell R, Holland TJB, Worley BA (2000) The effect of TiO₂ and Fe₂O₃ on metapelitic assemblages at greenschist and amphibolite facies conditions: mineral equilibria calculations in the system K₂O-FeO-MgO-Al₂O₃-SiO₂-H₂O-TiO₂-Fe₂O₃. *Journal of Metamorphic Geology* 18:497-511
- Zen, E., (1966) Some topological relationships in multisystems of n+ 3 phases; Part 1, General theory; unary and binary systems: *American Journal of Science* v. 264 p. 401-427